AALBORG UNIVERSITY

DEPARTMENT OF ENERGY TECHNOLOGY

$10^{th}$ SEMESTER

# DC Wind Farm Power Collection Network Design and Analysis

*Author:*
Rólant J. Olsen
Marie-Christine Schimmelmann

*Supervisor:*
Philip Carne Kjær

EPSH-1030

June 3, 2015

AALBORG UNIVERSITY

**Department of Energy Technology**
Fredrik Bajers Vej 5
9100 Aalborg
Telephone +45 9940 9940
http://www.et.aau.dk

**Title:**
DC Wind Farm Power Collection Network - Design and Analysis

**Project period:**
February $2^{nd}$ 2015
June $3^{rd}$ 2015

**Project group:**
Group EPSH4-1030

**Authors:**
Rólant J. Olsen
Marie-Christine Schimmelmann

**Supervisor:**
Philip Carne Kjær

**No. printed copies:** 4

**No. of pages:** 116

**No. of appendix pages:** 22

**Total no. of pages:** 132

**Completed:** June $3^{rd}$ 2015

**Synopsis:**

In offshore wind farms, DC power collection networks constitute a promising alternative to the commonly utilized AC networks in terms of system losses and costs. However there is no practical experience with their operation so far. In order to identify characteristics and weaknesses of the DC wind farm concept, case studies which reflect the system behaviour are required.
This project proposes a possible design for such networks, including implementation of a control strategy and discussion of the system's protection scheme. Transient analysis is conducted for selected cases in PSCAD to identify typical wave forms of the system responses, find maximum stresses and to verify the network design.

Rólant J. Olsen

Marie-Christine Schimmelmann

# Preface

This master thesis has been composed at Aalborg Universities Department of Energy Technology, in the spring of 2015 by Rólant J. Olsen and Marie-Christine Schimmelmann, group number EPSH4-1030, by way of their $10^{th}$ semester. The project is based on a proposal from Vestas and a subject has been chosen to form a basis for the project report: *DC wind farm power collection network control and protection*.

Literature references are shown in IEEE style. References are marked with the a single number in square brackets. The bibliography is generated numerically by order of referencing. Books in the bibliography are shown with; author, title, publisher, year of publication and ISBN number. Websites are shown with; author, title of website, website address and date of access. References to literature are placed immediately after a section or subsection, for instance; *"Electric energy is the most popular form of energy..."* [1]. References for figures and illustrations are placed in the captions. References to sections, figures and equations are as follows; section/figure/equation 1.2.3.

The following software is used in this project:

- LaTeX- report, graphs, illustrations and circuit drawings
- PSCAD - transient analysis
- MATLAB/Simulink - data processing and control
- PLECS - circuit and control studies

A CD-ROM is enclosed containing the following:

- PDF of the thesis
- PSCAD models
- MATLAB/Simulink files
- PLECS models
- Literature references

# Nomenclature

| Symbol | Description | Unit |
|---|---|---|
| A | Area | $[mm^2]$ |
| a | Temperature coefficient | $[-]$ |
| b | Electric field coefficient | $[-]$ |
| C | Capacitance | $[F]$ |
| $C$ | Scale factor | $[-]$ |
| c | Specific heat | $[J/kgK]$ |
| E | Energy | $[J]$ |
| f | Frequency | $[Hz]$ |
| g | Conductance | $[S]$ |
| I | Current | $[A]$ |
| k | Shape factor | $[-]$ |
| L | Inductance | $[H]$ |
| l | Length | $[m]$ |
| m | Mass | $[kg]$ |
| p | Probability | $[-]$ |
| P | Real Power | $[W]$ |
| r | Radius | $[m]$ |
| R | Resistance | $[\Omega]$ |
| T | Thermal resistance | $K$ |
| U | Voltage | $[V]$ |
| v | Speed | $[m/s]$ |
| X | Reactance | $[\Omega]$ |
| Y | Admittance | $[S]$ |
| Z | Impedance | $[\Omega]$ |
| $\alpha$ | Temperature coefficient | $[-]$ |
| $\gamma$ | Propagation constant | $[-]$ |
| $\Gamma$ | Gamma function | $[-]$ |
| $\delta$ | Voltage angle | [rad] |
| $\epsilon$ | Permittivity | $[F/m]$ |
| $\Theta$ | Temperature | [K] |
| $\mu$ | Permeability | $[H/m]$ |
| $\rho$ | Thermal resistivity | [K/W] |
| $\sigma$ | Electric field | [V/m] |
| $\tau$ | Time constant | [s] |

# Abbreviations

| Index | Description |
|---|---|
| AC | Alternating Current |
| BIBO | Bounded-Input Bounded-Output |
| CF | Capacity Factor |
| CPP | Conventional Power Plant |
| DAB | Dual Active Bridge |
| DC | Direct Current |
| DS | Dansk Standard |
| EN | European Standards |
| FACTS | Flexible AC Transmission Systems |
| HV | High Voltage |
| HVAC | High Voltage AC |
| HVDC | High Voltage Direct Current |
| IEC | International Electrotechnical Commission |
| LV | Low Voltage |
| MHI | Mitsubishi Heavy Industries |
| MV | Medium Voltage |
| MVAC | Medium Voltage AC |
| MVDC | Medium Voltage Direct Current |
| PCC | Point of Common Coupling |
| PCN | (offshore) Power Collection Network |
| PE | Polyethylene |
| PI | Proportional Integral |
| PLECS | Piece-wise Linear Electrical Circuit Simulation |
| PMSG | Permanent Magnet Synchronous Generator |
| PSCAD | Power Systems Computer Aided Design |
| pu | Per Unit |
| SAB | Single Active Bridge |
| SSCAPN | Substation Capacitor Negative |
| SSCAPP | Substation Capacitor Positive |
| SSN | Substation Negative |
| SSP | Substation Positive |
| TS | Transmission System |
| TSO | Transmission System Operator |
| VSC | Voltage Source Converter |
| WPP | Wind Power Plant |
| WT | Wind Turbine |
| WTG | Wind Turbine Generator |
| XLPE | Cross-Linked Polyethylene |

# List of Figures

# List of Tables

# Contents

# 1 Introduction

This chapter aims to provide an overview of the thematic focus of this project. First the background for utilizing DC grids in offshore wind farms will be described. The problem formulation presents issues that are likely to be encountered in this context. Subsequently, the objectives of this project are derived and its scope and limitations are explained. Finally, the project structure is specified.

## 1.1 Background

During the last decades wind power has become a serious participant in electrical power generation with an installed power capacity of approximately 130 GW at the end of 2014 [7]. The utilisation of large scale offshore wind power plants (WPP) is a way in which countries can reach their goals of renewable energy implementation. Therefore, the capacity of European offshore wind power is supposed to increase by 20 GW from the current 8 GW by the year 2020 [8].

Within today's offshore WPPs the power of the individual wind turbines (WT) is gathered in an AC collection network and transferred from an offshore substation to shore. If situated remotely from shore, offshore WPPs are connected to the national grids via HVDC links. This means that power is converted several times within the WPP before reaching the onshore grid.
Modern WTs use voltage source converters (VSC) to convert from variable frequency AC to DC and then back again to the fixed frequency of the collection network. Furthermore transformers are utilized to step up to the network's medium voltage (MV) within the WT and, after joining the power of all WTs at an offshore platform, to step up to high voltage (HV). At the offshore substation, the power is converted by another VSC to HVDC in order to be sent ashore. Disadvantages of this common practice are conversion losses and the necessity of large, heavy and costly equipment.

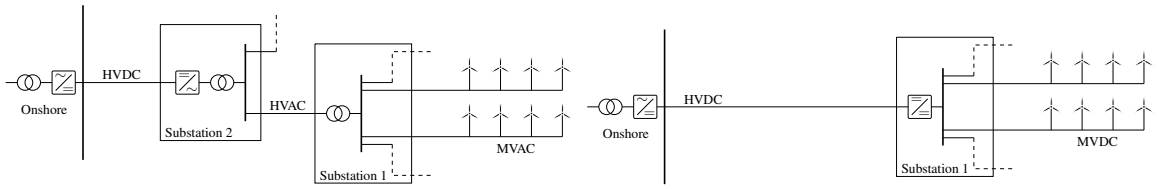


**(a)** AC system configuration **(b)** DC system configuration

**Figure 1.1:** Difference between WPP system configurations

One promising approach to improve costs and losses of future WPPs is the utilisation of a DC power collection network. If WTs had a MVDC output, which then was collected at a single platform and converted to HVDC, the savings would be considerable.
In such a system the power from the individual WTs would be converted by an AC/DC converter with an integrated step-up transformer to MVDC, gathered at the offshore HVDC station and stepped up by a DC/DC converter to HVDC. Thereby the number of conversion steps is reduced compared to an AC grid, which avoids unnecessary losses. The utilized high frequency DC/DC transformers are considerably smaller than AC transformers used today. Comparing AC and DC power transmission by way of conductor cross section, it is clear that DC power cables can operate with a smaller conductor

to transfer the same amount of power. Consequently this topology would benefit by having smaller, lighter and fewer components, thereby reducing the size and amount of offshore stations, the cost of components and of their installation.

## 1.2 Problem Formulation

As described in the previous section, DC offshore wind farm power collection networks (PCN) offer the possibility to improve the technical and economical performance of a WPP. However there is no practical experience with their operation, so that reliable control and protection schemes need to be developed and proved. Case studies need to be performed in order to characterize system behaviour of possible DC system configurations and identify challenges and risks connected to the utilisation of this wind farm concept.

In order to derive a suitable DC PCN from common practice AC PCNs, the grid components, such as cables and switchgear, have to be adjusted to fit DC requirements. Some of the equipment that will find usage in future DC PCNs is still in the development stage and not yet readily found on the market. This applies e.g. to DC/DC converters installed at the wind turbines as well as in the offshore HVDC station. Requirements on converter designs and proposed solutions are currently being developed, they are discussed in the literature.
Furthermore, the utilisation of DC power transmission requires special focus on the protection of the system, as conventional techniques known from AC power systems cannot be applied without further ado. For example, conventional AC breakers use a zero crossing of the current, which DC current inherently does not feature. Fault case simulations need to show, if transients create usable zero crossings that allow their utilization or if special equipment is required. Consequently protection schemes need to be developed specifically for the application in DC grids.

## 1.3 Objectives

Resulting from the problem statement described above, the following objectives for the project are derived:

- Design of a MVDC power collection network concept.
- Development of a control scheme for the MVDC power collection network.
- Development of a protection scheme for the MVDC power collection network.
- Conduction of case studies to characterize the system behaviour.
- Assessment of applicability and weaknesses of the proposed system design.

The success of the project is given by the fulfilment of the listed objectives.

## 1.4 Scope and limitations

The following aspects will be addressed in this project.

**Design of a MVDC power collection network concept**
The project focusses on the MVDC power collection network and the system boundaries are drawn accordingly. Comparing to the configuration depicted in figure 1.1b, only the part right of the DC/DC converter is regarded in detail, comprising MVDC cables, which connect the individual turbines to the substation, switchgear, and the MV side of the turbine and of the HVDC link converters.
In order to exploit the potential savings that are expected of the DC wind farm concept, the

system design will be kept as simple as possible. MVDC cable design, system voltage level, the converter output filters, grounding strategies, switchgear and the utilization of single or multi-converter substation topologies will be addressed.
Since MVDC cables are not available on the market yet and due to the different properties of DC compared to AC current transmission, e.g. the elimination of skin-effects, an MVDC cable design will be developed. The conduction losses resulting from the cable design and rated system voltage will be calculated, utilizing load flow analysis, and compared to expected annual energy production of the WPP.

**Development of a control scheme for the MVDC power collection network**
In general, wind farm control consists of several control layers with different tasks. For this project the focus is placed on the wind turbine control level at the converter output side, which aims at feeding power into the PCN according to a given power reference. However, since voltage drops in the DC PCN depend on active power flows, they have to be able to reduce their power injection in order to maintain the system voltages within allowed limits, if required.
The control scheme will be developed utilizing MATLAB/Simulink. It will be implemented into a PLECS model of the system to validate its functionality.
The voltage at the offshore substation converter is assumed to be given in this project and will only be regarded as a disturbance to the WT control. Its control would require more detailed consideration of the substation DC/DC converter and connection to shore, which is outside the scope of this project. Likewise, the WPP control level and the control of the turbines themselves are neglected.

**Development of a protection scheme for the MVDC power collection network**
Protection is required to provide a reliable power plant with low downtime throughout its lifetime and to avoid damage to system components. Disconnectors are required to allow safe maintenance of all components. However, protection equipment that can break faults is costly and bulky.
Therefore the aim is to design the system in such a way, that it can operate without any additional switchgear. The hypothesis that this is possible is based on the fact that wind turbines with a converter interface do not contribute fault currents, hence only the energy stored in the system will feed into the fault. After the fault transient is depleted, the faulty part of the grid can by separated by disconnectors. Based on this hypothesis the development of a fault detection and protection algorithm is not within the project scope.

**Conduction of case studies to characterize the system behaviour**
For the identification of characteristics and weaknesses of the DC wind farm concept case studies, which reflect the system behaviour under expected operating conditions, are required.
In this project, short circuit transients will be analysed for selected fault types, in order to gain knowledge about transient waveforms, that are to be expected for systems with similar design, and to identify worst case faults. PSCAD is utilized for the simulations.
Validity of the transient analysis results depends on the validity of the cable modelling tool provided by PSCAD.
Static fault cases will not be present in the grid, in accordance with the aim to have a design where no sources feed into faults. Harmonic studies are not regarded, since they depend on converter design, which is outside the project scope. Since lightening and breaker surges are not expected travelling wave analysis is disregarded too.

**Assessment of applicability and weaknesses of the proposed system design**
A specific DC power collection network topology and design are chosen in the early stages of the project. Control and protection development as well as transient analysis and the identification of system characteristics are based on these choices. It is expected that during the project, weaknesses and strengths of the chosen design will show. This will be pointed out and suggestions for changes regarding the affected design aspects will be given.

Obviously, presented results are valid only for the specific WPP configuration. Applicability for other WPP designs is not investigated. Furthermore the project is subject to the following limitations:

- The often discussed possibility of a European super-grid and multiple interconnections of offshore wind farms with each other and several transmission grids is not considered. The regarded WPP is connected with one single VSC HVDC connection to the onshore transmission grid.
- Converter designs for MVDC and HVDC converters are not regarded in this project. In the models, they are considered as current sources in case of the turbine converters, and voltage sources in case of the substation converter.
- All converters in the system are assumed to utilize single active bridge topologies, i.e. they are designed for unidirectional export of power only and will block power inrush from the external grid. This has to be considered for the applicability of cable design recommendations and the design of protection in particular, since both are based on the estimation of possible current flows in the PCN.
- Only type D turbines, as specified in [9], are used.
- The utilization of full scale converters in type D turbines allows complete decoupling of active and reactive power control at the WT output. Out of these, within the project scope only active power control will be examined as the DC PCN inherently does not feature reactive power.
- As a direct consequence from the previous point, the compliance of the WPP with national grid codes regarding reactive power and voltage requirements at the PCC with the onshore transmission grid, has to be ensured onshore. Reactive power/voltage control are therefore not in the scope of this project, as the focus is placed on the DC PCN only.
- All wind farm components which are out of the project scope are assumed to possess sufficient protection to prevent destruction by internal component faults, e.g. converters do not allow current flows above their own current ratings through their semiconductor devices.
- Switchgear which is required for the system will be specified. However, the development of specific DC switchgear, if not yet available commercially, is not part of the project.
- Shadowing effects, fluctuations etc. within the wind farm are neglected, as they are very site dependent and influence the energy output of the plant, but not the dimensioning of components, control and protection. The wind power in the simulations is consequently assumed to be equal at all turbines.
- Ambient temperatures are assumed to be constant throughout the year. Seasonal changes and long term heating effects due to cable operation are not regarded.

## 1.5 Structure

The structure of this report is as follows:

Chapter 2 presents a literature review, including possible topologies of DC collection networks in offshore wind farms, strategies for WPP control, protection principles and switchgear.

In chapter 3 the studied WPP is described regarding its topology and all relevant components. An overview of the DC system configuration and a definition of system boundaries connected to the scope of this project is given. Differences between an AC and DC wind farm concept are outlined. Furthermore the MVDC cables utilized in the power collection network are designed. Finally, energy production and conduction losses in the WPP are analysed.

The next chapter, 4, focuses on control within the PCN. A strategy for control of power injection on the wind turbine level is developed and implemented in a model of the grid, aiming at following a given power reference while keeping the system voltage within permitted limits.

Chapter 5 analyses transients occurring during normal operation and selected fault cases. Transient behaviour of various grounding strategies of cable armour and sheath is compared and a suitable strategy chosen for utilisation in the system. The transient behaviour of the simulated cases is characterized and weaknesses in the system design are discussed. Worst case faults regarding transient voltage and current peaks are identified.

In chapter 6 selected aspects of the system design are revised based on the transient simulation results obtained before. Worst case faults regarding transient temperature rise, fault depletion time and speed of system de-energization are identified. The MVDC cable's capability to withstand transient electric stresses and temperature rises is validated. Furthermore, a discussion of system protection compares consequences of implementing various protection schemes.

Finally, in chapter 7 the addressed issues are discussed and concluded. An outlook on future work in the context of DC PCNs is also given here.

# Literature Review 2

This chapter provides an overview and background knowledge regarding topics discussed in the project, based on literature research. It contains information on possible DC wind farm topologies, wind farm control, protection principles and switchgear.

## 2.1 DC Grid Topologies

DC wind farm collection network layouts discussed in the literature are classified according to different characteristics. Converter topologies, position and number of power transformation steps and layout of the turbine interconnections are specified as distinguishing criteria.

### 2.1.1 DC/DC Converter Placement

[2] discusses different configurations for the position and subsequently necessary amount of DC/DC converter step-ups within the PCN. The proposed options are depicted in Fig. 2.1.

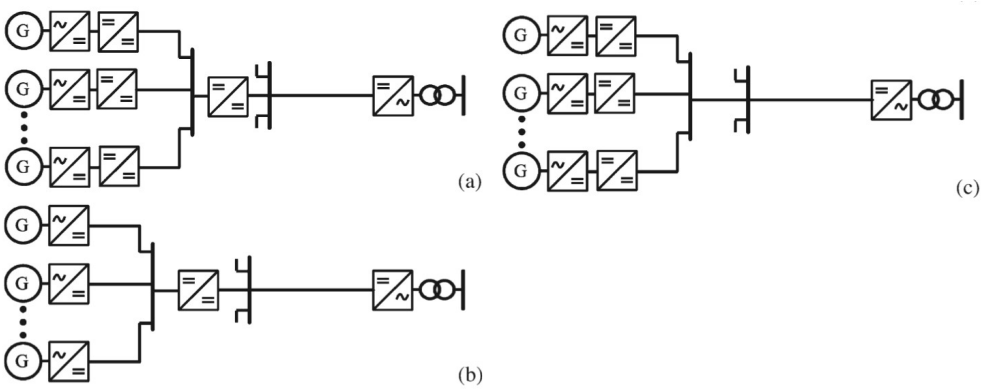


**Figure 2.1:** Possible DC/DC converter placement in the PCN; (a) Two step-ups. (b) One cluster step-up. (c) Turbine step-up [2]

In the two step-up configuration (a), the voltage is converted from the output level of the wind turbine generator (WTG) to MV at each turbine and to HV after the power flows of all turbines have been collected. Advantages of this technology are reduced cable losses within the PCN due to MV voltage level and individual controllability of the turbine voltages. However, the high number of converters increases converter losses.
Alternatively, in the cluster step-up option (c), the power is first collected at turbine output voltage and subsequently converted to HV collectively. This configuration benefits from reduced number of converters, but has the disadvantage of increased transmission losses within the LV PCN.
Finally it is possible to step up to HV at each WTG (c). Due to the HV in the PCN transmission losses are lowest. On the other hand the direct conversion from LV to HV at low power levels leads to high converter losses.
The authors conclude that the cluster step-up is best, when comparing the three configurations regarding their system losses and cost.

Another solution is proposed in [3], which is completely avoiding the offshore HVDC substation. Instead, the wind turbines are connected in series to generate the HV used for the transmission to shore. On the downside, the turbines operate at high potential and have to work with overrated voltage if another turbine is lost [10]. The layout is shown in Fig. 2.2.

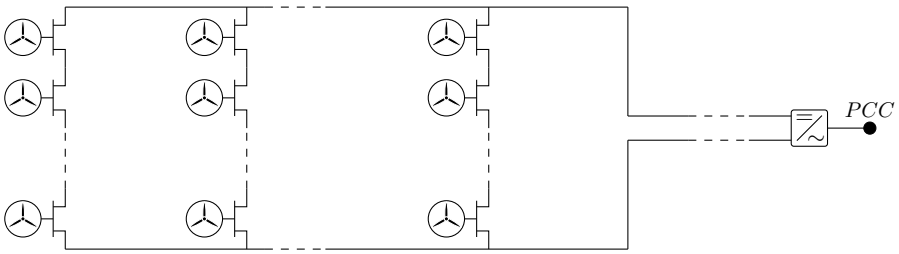


**Figure 2.2:** Series connection layout of a DC PCN [3]

### 2.1.2 Layout of the Turbine Interconnections

Possibilities to interconnect the turbines within the PCN are summarized in [4]. These include radial networks, single return networks, ring and multiple ring networks and star networks with conection to a single junction as well as multi-hub ring configurations, as can be seen in Fig. 2.3.

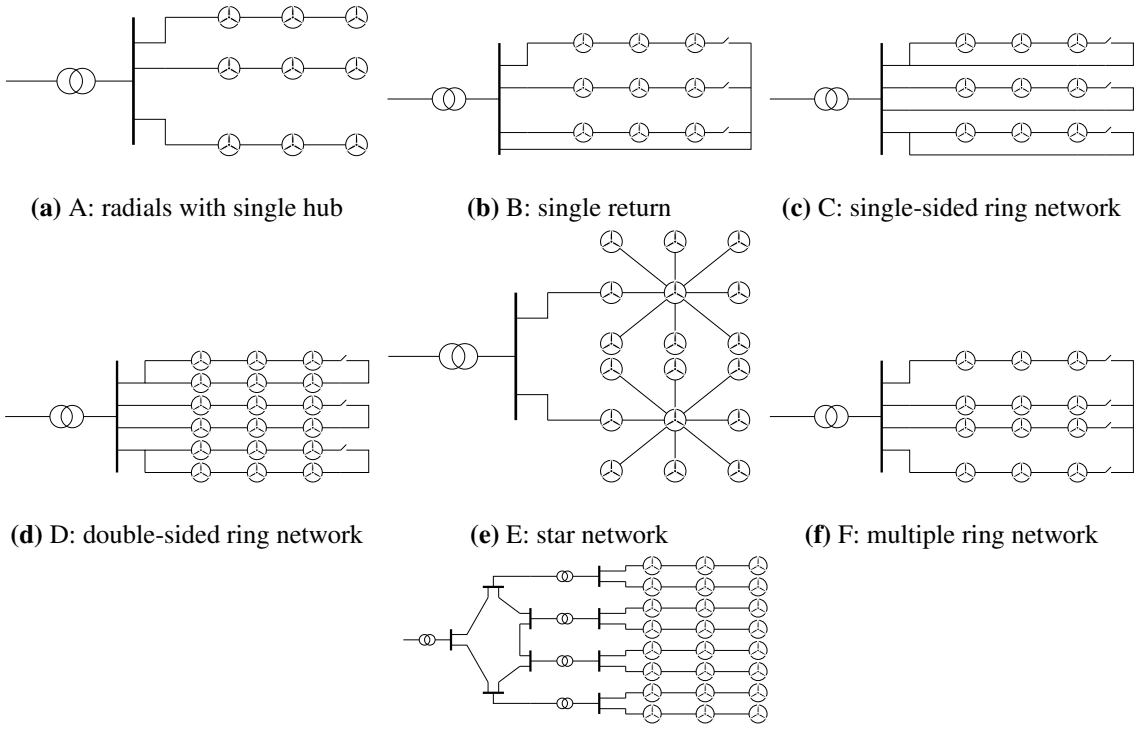

**(a)** A: radials with single hub

**(b)** B: single return

**(c)** C: single-sided ring network

**(d)** D: double-sided ring network

**(e)** E: star network

**(f)** F: multiple ring network

**(g)** G: multi-hub ring

**Figure 2.3:** Possible layouts of the turbine interconnections within the PCN [4]

Depending on the choice of layout, the system reliability and the dimensioning and cost of components vary. While the radial system is cheapest and can be easily controlled and protected, it has poor reliability in case of faults close to the junction point. Single return and ring networks, on the other hand, introduce redundancy by offering alternative paths for power export in case of faults. However, they require additional cables and higher cable ratings, therefore their cost of material and installation is increased.

## 2.2 Wind Farm Control

Control of WPP plants is a necessary aspects of their operation in order to maintain their influence on the transmission system (TS) which they are connected to within requested limits, especially with regard to current grid codes that require WPP's to operate similarly to conventional power plants (CPP). Furthermore control ensures the maintenance of system stability within the WPP collection network.
While CPPs are often composed of identical equipment units that are connected to the same bus of the TS and can therefore be controlled with a common controller, WPPs are more complex. Unlike CPPs they feature a converter based grid interface, which decouples the generators from the grid. Their power output fluctuates with the available wind and their power rating is smaller than that of conventional units (from kW to MW range). In addition to the turbines, the plant is composed of its PCN and additional devices such as FACTS and energy storages, therefore each turbine faces different operating conditions than seen at the PCC.
Resulting from this, modern WPPs feature 2 control levels, a WPP controller and individual WT controller. The former constitutes an interface between the TS(O) and the WPP and is responsible for distributing the respective control task to the individual turbines, while the latter ensures the operation of the individual WTs according to their received reference values [5].

### 2.2.1 Wind Power Plant Control Level

The structure of the WPP control level is shown in figure 2.4 for the example of active power control. The WPP receives an active power reference $P_{ref}^{WPP}$ from the TSO, which is set according to an overall control function based on grid code requirements and the kind of contract the WPP owner has signed. The WPP controller, or main controller, is typically realized as a PI controller with anti wind-up limiter and calculates the overall plant output $P_{out}^{WPP}$ based on measurements at the PCC. This signal is used as input for the dispatch function, which assigns individual reference points $P_{ref}^{WT}$ to the individual turbines based on their available power.

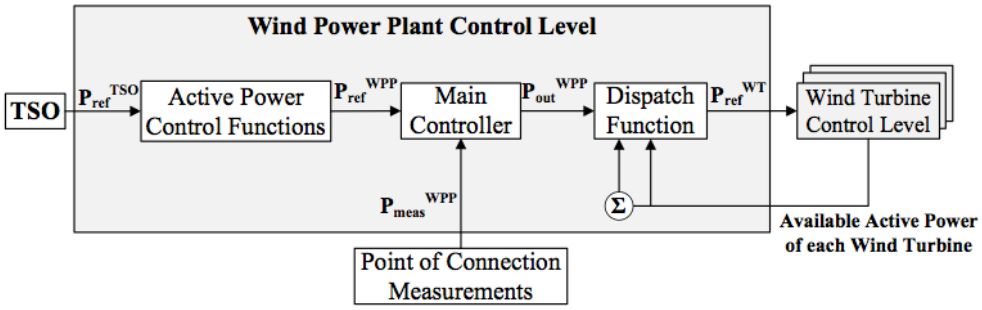


**Figure 2.4:** WPP control level for active power control [5]

There are various strategies for realising the power dispatch, e.g. direct forwarding of the p.u. power reference to the individual WTs, splitting $P_{out}^{WPP}$ in proportion to the available wind power of each WT or dispatching by means of an optimum power flow analysis, taking into consideration the WPP's internal losses and wind power availability [5].

### 2.2.2 Wind Turbine Control Level

The main aim of this level is to control the power injected into the grid, employing both the mechanical and electrical part of the power train. The comparably slow mechanical system is in charge of overall power control, which is handled aerodynamically by pitch and yaw adjustment, and acts either based on given setpoints from the dispatch centre or individually, maximizing the output with respect to available wind power. The electrical system on the other hand features fast dynamics. Its

responsibility covers the interconnection with the grid, active and reactive power control, overload protection. While the generator side converters take care of maximum power extraction, the grid side converters main task is to keep the dc link voltage at a fixed value.
Having different bandwidths (and hence fast and slow control dynamics respectively), the control loops of electrical and mechanical system can be treated independently [11]. Due to the utilization of full scale converters in type D turbines, active and reactive power control are completely decoupled [5].

## 2.3 Protection

In this section the basic principles of distance and differential protection will be explained. Protection schemes are dependent on the specific layout of the wind farm and will only be explained in general terms in this section.

### 2.3.1 Distance protection

The general concept of distance protection is to measure short circuit voltage and current at a specific relay location, in order to determine the fault impedance. The known line impedance is then compared to the fault impedance and if it is smaller, it is recognised as an internal fault and the breaker trips. Figure 2.5 shows a representation of the principle.

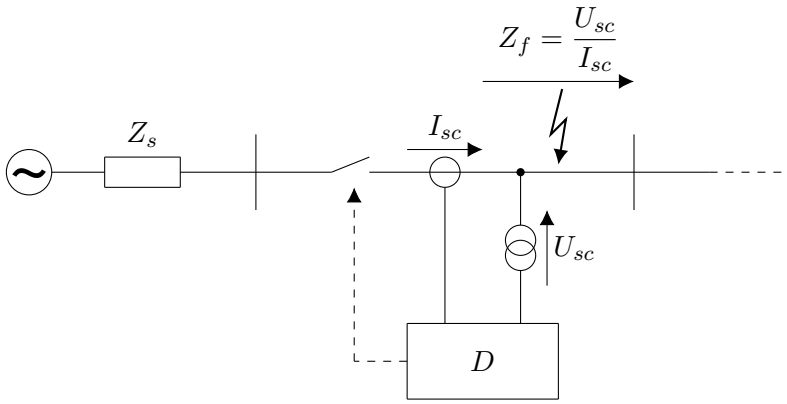


**Figure 2.5:** Principle of distance protection

When implementing distance protection it is important to consider inaccuracies which can be caused by measurement errors, current transformer errors and the impedance value of the line which is usually calculated and not measured. The inaccuracies mean that when setting the relay, a safety margin of 10-15 % should be selected. With long lines or cables, several relays are placed in series with a set distance in between them and a time delay added to the settings in order to maintain selectivity. [12]

### 2.3.2 Differential protection

The most common type of differential protection is the current type. It calculates the sum of all the currents going in and out of a protected device, according to Kirchhoff's current law the sum of these must always be zero if there is no fault. Utilising digital communications equipment with fibre optic cables, lines and cables exceeding 100 km may be protected by differential relays.

The basic working principle of the differential current protection can be seen in figure 2.6, where there is a fault outside of the protected area and the relay compares the currents entering and existing and sees no difference so nothing trips. In figure 2.7 there is an internal fault which means that the

short circuit will draw in current which the relay will then add together and see an increase and the trip order is given. [13]

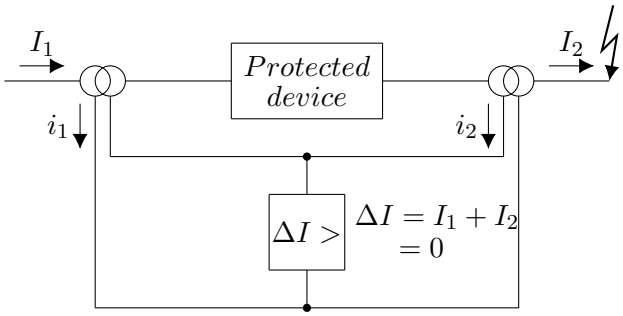


**Figure 2.6:** Differential protection external fault

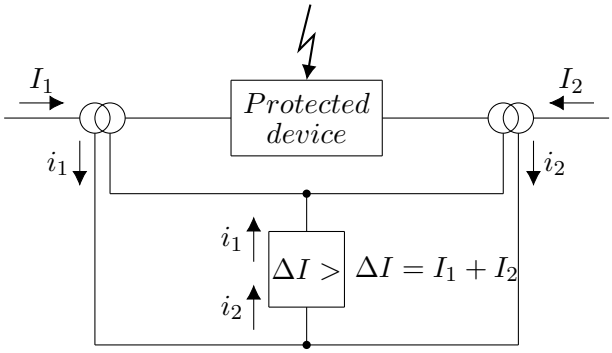


**Figure 2.7:** Differential protection internal fault

### 2.3.3 Protection coordination

Fault detection on an offshore wind farm is divided in to a few different areas. These areas could be cables, turbines, bus bars and converters. Depending on the wind farm layout, there are different approaches on how to coordinate the protection, but the general idea is to have some localised detection for the individual parts, cables and turbines, and then to have the ability to isolate whole branches at the bus bars if required. The red boxes in figure 2.8 represent the primary protection areas which could be secured by differential protection, which relies on communication between relays. If these however malfunction, the secondary protection layer, marked in blue in figure 2.8, will disable the entire radials to minimise damage from a fault. [14]

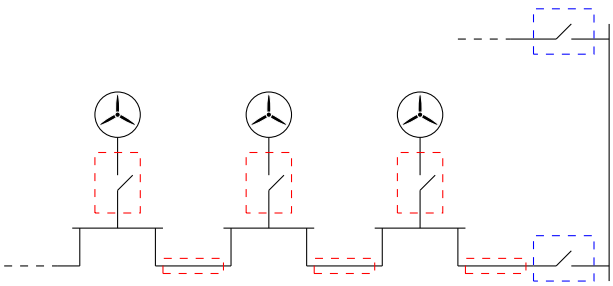

**Figure 2.8:** General protection zones

## 2.4 Switchgear

There are some important considerations to be done when analysing DC grids. For instance the protection equipment used in AC grids can often not be used in DC grids. AC circuit breakers utilise the natural zero crossing of alternating current to eliminate arching and other damaging effects. In DC grids however this is not possible without some modifications, due to the lack of any natural zero crossings.

### 2.4.1 Disconnectors

Disconnectors are used to isolate parts of electrical systems or components, usually for maintenance or repair. These devices are not intended to disconnect currents since they no means of suppressing arcs, which would occur when disconnecting high currents. In offshore wind farms they would be placed on substations to be able to isolate the individual radials and the substation itself. Wind turbines also include disconnectors to ensure separation from the electrical grid when maintenance work needs to be performed.

### 2.4.2 AC circuit breaker

AC circuit breakers take advantage of the fact that alternating current goes to zero once every cycle. This means that the breaker can monitor the current level and break at the exact point when it crosses zero. The benefit is a reduction in breaker size and a minimal influence to the rest of the system compared to disconnecting at nominal current levels which is the case when breaking DC currents as seen in figure 2.9.

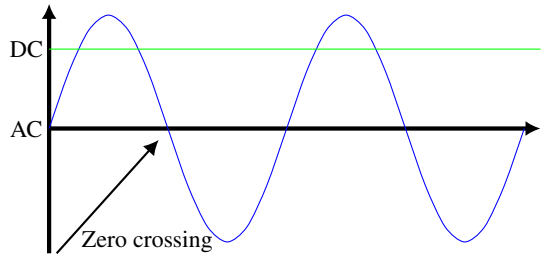


**Figure 2.9:** Zero crossing

#### Fuse

Fuses can be used as protection from over currents and short circuits effectively, but after a fault they need replacement, making them expensive to use in offshore wind farms as this would require personnel to travel to the site and physically replace the fuse.

### 2.4.3 DC circuit breaker

DC circuit breakers can be divided into three categories, mechanical, static and hybrid. These will be examined further to get an overview of their benefits and working principles. [15]

#### Mechanical DC circuit breaker

A mechanical circuit breaker combined with a passive parallel circuit can be utilised in order to create a zero crossing when breaking, which can be seen in 2.10. During normal operation the power flows through the breaker, but when it opens an arc is created and the parallel circuit causes it to oscillate which forces the current to cross zero and then allowing the breaker to open and disconnecting the power flow. The speed of this type of breaker depends on the time it takes to charge the capacitor. In order to speed it up it is possible to create an addition to the breaker to charge the capacitor independently. A surge arrester is also added in parallel to protect the system from breaking transients. [15] [14]

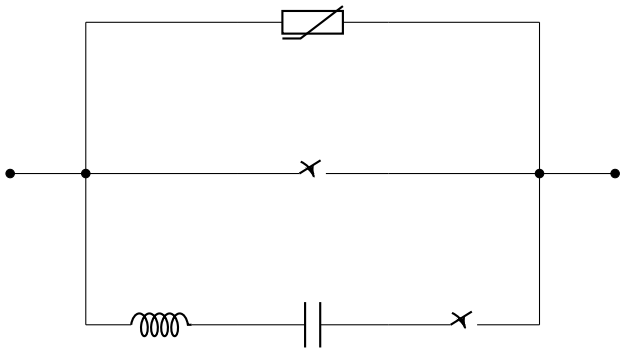

**Figure 2.10:** DC breaker with resonance circuit and surge arrestor

### Static circuit breaker

The static circuit breaker uses power electronics to control the power flow and typically made with IGBTs. The benefit is a very fast disconnection, < 1 ms, and it does not cause any unwanted transients. These types of breakers do however have significantly higher losses than compared to regular breakers since the power always flows through the semiconductors and due to these power losses, cooling is also required, which increases space and cost requirements. The static circuit breaker can be seen in figure 2.11. [15] [14]

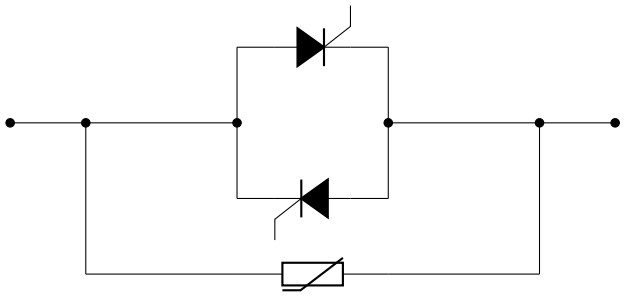

**Figure 2.11:** Static circuit breaker with surge arrestor

### Hybrid circuit breaker

The hybrid circuit breaker effectively combines the previously examined breaker types. This design is very effective since it has the little or no losses when the breaker is closed, but does not arc when breaking since the static switch will actually be the one the opens the circuit. A specific system designed by ABB has been tested and could break currents up to 16 kA [16]. The layout of the switch can be seen in figure 2.12. [15] [14]

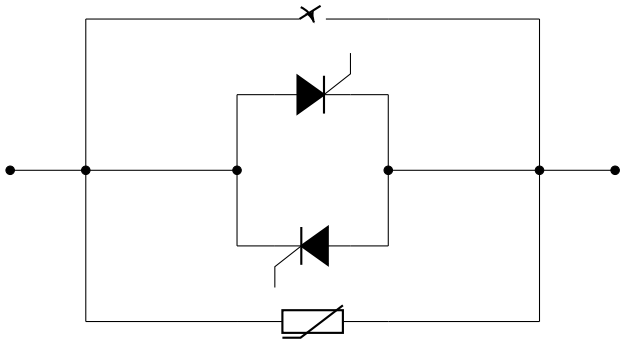

**Figure 2.12:** Hybrid circuit breaker

# System Design 3

In this chapter the wind farm and its components will be analysed, starting with an overview of the DC system configuration and a definition of system boundaries connected to the scope of this project. As a study case the AC wind farm topology, depicted in figure 3.3, is transformed to the investigated DC concept. The differences between AC and DC wind farm concept will be outlined.
A cable sizing section follows, where a mathematical approach is taken to look at the thermal design and the insulation, in order to find a cable sizing algorithm. Finally the energy production and system losses will be analysed and a decision regarding cable design and voltage level for the system analysis in subsequent chapters will be made.

## 3.1 System description

An offshore WPP is composed of several segments, starting with the turbines producing electricity up to the interface with the external grid onshore. A system overview is presented in figures 3.1 and 3.2 for the currently used AC system and the possible future DC system respectively. Comparing the two figures it is seen that the main difference is the lace of substation 2 in the DC system configuration. In standard AC systems there are three conversion steps. MVAC from the turbines is transformed into HVAC at the first substation, after which it is converted at the second substation to HVDC for transport to shore. The immediate benefit of the DC system configuration is that the second substation is completely avoided. MVDC is generated at the turbines which is collected at the substation, and then converted to HVDC for export.

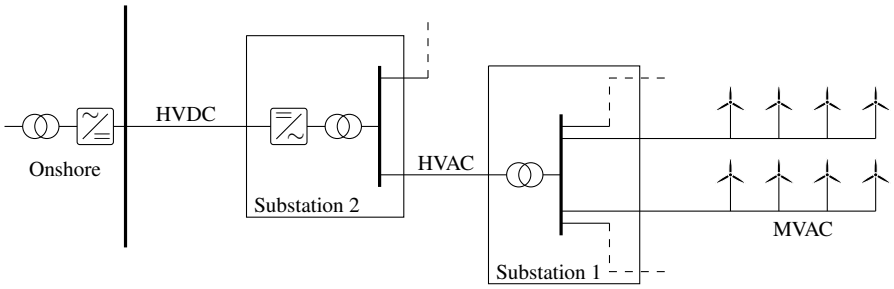


**Figure 3.1:** AC system configuration

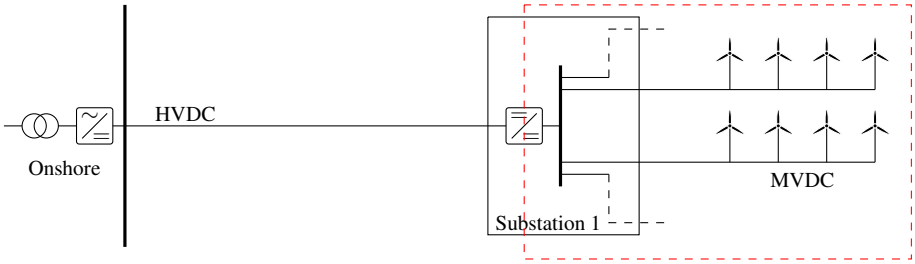


**Figure 3.2:** DC system configuration

The scope of this thesis consists of the components within the red box in figure 3.2, which is marking

the system boundaries. This includes the MVDC side of the DC/DC converter in the substation and all radials with respective turbines and cables.

### 3.1.1 Power Collection Network Topology

The layout of the PCN is depicted in figure 3.3. Eight feeders, with four turbines each, are connected to the offshore substation, which connects the WPP via an HVDC link to shore. The 32 turbines are V164 8.0 MW turbines from the manufacturer MHI Vestas Offshore Wind [6]. The substation depicted is the original AC design and will be altered accordingly later in the thesis.

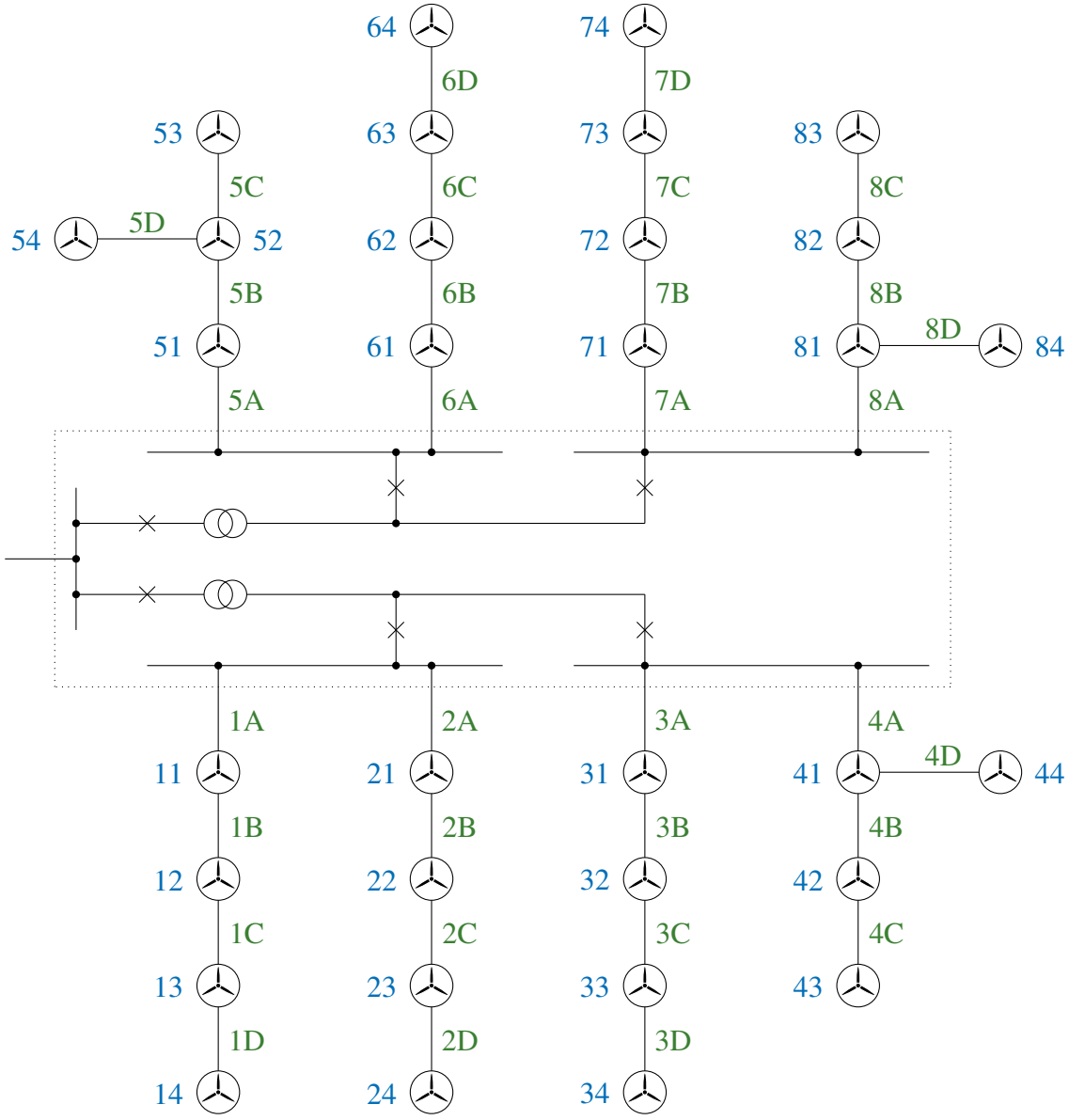


**Figure 3.3:** Wind farm topology

The turbines have been labelled in blue and start from the bottom left radial with the first number representing the radial number and the second number is the number of the turbine, counting from the substation. The cables are labelled in green and follow the same number as the turbines, but with letters for the specific radial cable. Cable lengths are summarised in table A.4, appendix A.5.

Subsequently, the main components of concern for the DC wind farm PCN concept are introduced.

### 3.1.2 Wind Turbine Power Train

The power train connecting each turbine to the PCN is depicted in figures 3.4 and 3.5 for the AC and DC system respectively.
The turbine rotor, which is propelled by wind, powers a permanent magnet synchronous generator (PMSG). They are connected by means of a drive shaft and a gearbox. The mechanical power is transformed into electrical power by the PMSG. Magnitude and phase of the three phase AC output are variable, depending on wind speed, the design of the turbine components and its mode of operation. To enable grid connection of the turbine, its power needs to be brought to grid frequency and voltage. Therefore, the electric power is first rectified and then transformed to satisfy the requirements of the PCN.
At this point, the power train configuration is different depending on the PCN design. In the AC system, the power is altered to the required frequency and voltage level by series connecting an inverter and transformer.
For the new DC system approach, these two components are replaced by a DC-DC converter, indicated by the red dashed box in figure 3.5. Its aim is to step up the voltage to the required magnitude. The converter is explained in more detail in subsection 3.1.3.

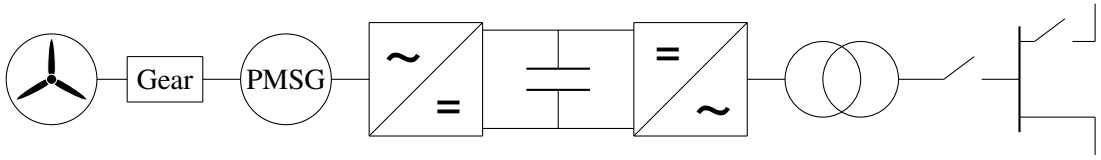


**Figure 3.4:** AC System Power Train Configuration

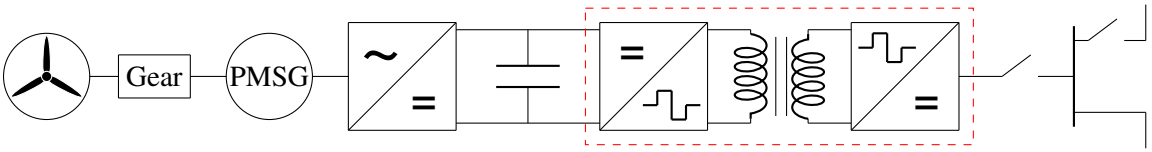


**Figure 3.5:** DC System Power Train Configuration with DC-DC converter (red box)

In this project, the power train of the turbines is not regarded further. The observations concentrate on the MVDC side of the PCN, beginning on the output side of the DC-DC converters.

### 3.1.3 DC-DC converters

The DC-DC converters purpose is to change the voltage of the power produced by the turbines. They are installed in the power train of each turbine, where the voltage is stepped up to the medium voltage level of the PCN, and in the offshore substation, where the it is stepped up to the high voltage level of the HVDC link.
Each DC-DC converter consists of a controllable full bridge inverter producing a medium frequency square wave, a transformer providing galvanic isolation and stepping up the voltage and a rectifier connected in series, as shown in figure 3.5. It may be configured as a single active bridge (SAB) with diode rectifier or dual active bridge (DAB) with transistor based rectifier, allowing unidirectional or bidirectional power flow respectively. This choice depends on the requirements regarding system energization, efficiency, dynamics and costs. If the system is needed to import power from the external grid, a DAB configuration is necessary.
The DC-DC converter works as a VSC. It is able to precicely follow a given current reference down to almost zero voltage. In case of a power flow reversal the current flow in the PCN will change direction, while the voltage polarity is maintained. This is of importance for cables with extruded insulation (compare cable layers in subsection 3.1.4), which are considered in this project, as they feature very limited ability to withstand voltage reversal.

In this project, only unidirectional power flow and hence SAB DC-DC converters are considered. Note that this requires the system to be energised from inside the PCN by e.g. a generator on the substation or by the turbines themselves. Energisation is however outside the scope of this project and considered to be provided.
Specific DC-DC converter designs are discussed in the literature, but as of today not utilized in this context. In this project, they are mainly regarded as a black box. According to their properties they are modelled as ideal current sources with a series inductance, representing the energy stored in the medium frequency transformer. The output is assumed to be ideally filtered, so that voltage ripples are not taken into consideration.

**Filter capacitors**

Filter capacitors are used to reduce voltage ripples of the input and output of the DC-DC converters in the system. They have an energy storage capacity equal to $1/2 \cdot CV^2$. On the turbine side of the PCN, two series connected equally sized capacitors are installed in parallel to the converter output. They are grounded at the midpoint in between both capacitors in order to provide a well defined voltage potential. The same principle is used at the substation for filtering the converter input.

Regarding the sizing, it is estimated that every output filter has a time constant of 50 ms, which means it stores enough energy to constantly provide nominal power for a duration of 50 ms. This corresponds to the rated power of the turbines at the turbine converters and to rated power of the WPP at the substation converter. As two capacitors are installed with each converter, each of them has to provide half of the required capacity. The capacitor size can be calculated according equations 3.1 and 3.2.

$$E = P\tau \tag{3.1}$$

$$C = \frac{E}{V^2} \tag{3.2}$$

Where $E$ is energy in joule, $P$ is power in watt and $\tau$ is the time constant in seconds, $C$ is capacitance in Farad and $V$ is voltage. For the modeling, capacitors will be considered as ideal components, as their internal resistances are small compared to cable and fault resistances.

### 3.1.4 DC cables

MVDC cables are composed of several layers, which are introduced subsequently.

**Conductor:** The current carrying conductor of submarine cables is made of copper or aluminium. The advantages of copper are its higher tensile strength and a lower resistivity. Hence it can carry more current with a smaller cross section, which will reduce the amount of material needed for the outer cable layers. However, aluminium has a lower density than copper and is considerable cheaper regarding material cost. [17], [18] The conductor of a cable can have different shapes: Solid conductors consist of one single massive wires and can be used for cross sections up to 400 $mm^2$. In submarine applications, conductors are mainly stranded from round wires, however for large cross sections as in HVDC applications profiled wire conductors are more economic, as they achieve higher filling factors. In order to achieve longitudinal water tightness of the cable, to prevent water from entering the cable after a fault or during installation, swelling agents are inserted between the conductor layers. [18]

**Insulation System:** The insulation system is composed of an insulation layer, which provides electric isolation between conductor and screen, and two semiconductor layers on both of its sides, ensuring the maintenance of a cylindrical electric field and avoiding the formation of gaps and partial discharges independent of the chosen conductor shape. Furthermore the insulation system provides some degree of mechanical protection. For submarine cable insulation, cross-linked polyethylene (XLPE) is the preferred material [18], offering high chemical resistance to oil and solvents, excellent tensile strength and high abrasion resistance [19], operating temperatures up to 90 °C and short circuit temperatures up to 250 °C. Alternatively, paper-insulated oil-filled cables or mass-impregnated cables can be used.

**Water-Blocking Sheath:** In order to prevent water ingression, HV cables are equipped with a metallic sheath. For MV cables however, they often operate with a simpler design of sheath, as they have to handle lower electric field strength compared to HV applications. Instead, polymeric sheaths with an additional water-absorbing layer under them are utilized to provide radial water tightness. High-density polyethylene is the most common material for that purpose. [18]

**Armour:** Metal wires, which form a wound layer around the cable, serve as mechanical protection against external threats in rough environments and provide tension stability. To provide corrosion protection, the armour comprises an additional layer of zinc and is flushed in bitumen. Alternatively, a polymeric sheath can provide the protection.

**Serving:** This layer, made of extruded polymers or wound yarn, protects the cable against scratches that would degrade the cables corrosion protection.

### 3.1.5 Offshore substations

Substations contain different components which allow them to combine the power received from the radials and transform it to a higher voltage before sending it to shore or another substation for further transforming. As could be seen in the system overview in figures 3.1 and 3.2, the AC system requires one substation more than the DC system, since it does not need to convert MVAC/HVAC and HVAC/HVDC, but only from MVDC/HVDC. In the wind farm layout in figure 3.3, the original AC substation can be seen which contains breakers and transformers. A DC substation will not require transformers, but breakers are important to be able to break fault currents to isolate faulted radials. The downside is that breakers and other protective equipment is costly and require space, so these will be attempted to be kept to a minimum or avoided entirely if possible. Disconnectors will always be present to allow for maintenance.

Depending on the power rating of the DC/DC converters and desired system redundancy, the substation may feature either one or several converters connected in parallel. The benefit of having several converters would be the ability to shut part of the wind farm off in faulted conditions, but continue to supply power to shore from the unfaulted radials. The downside is that several converters require more space and separate cooling, compared to a single large unit. Three substations designs will be presented and discussed here.

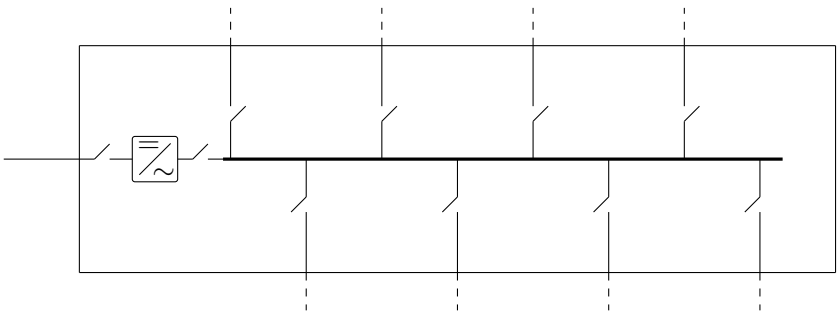

**Figure 3.6:** Layout of single converter substation

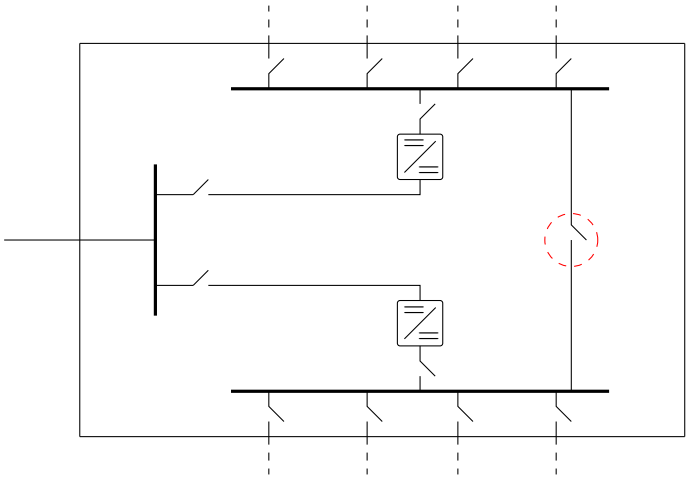

**Figure 3.7:** Layout of double converter substation

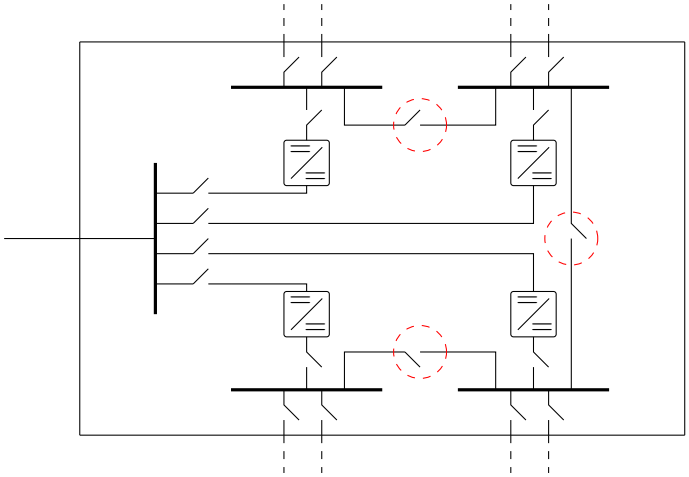

**Figure 3.8:** Layout of substation with four converters

Figure 3.6 shows a single converter substation with disconnectors at each radial and on either side of the converter. This is the simplest and cheapest design, but has the downside that if the converter fails the whole wind farm shuts down and cannot deliver power until it is fixed.

The double converter substation seen in figure 3.7 can maintain a minimum power supply of 50 % even if one converter fails or a fault situation occurs in any of the radials. If a fault happens in a radial, then the converter connected to it will stop exporting power, reducing the total to half until the fault can be isolated and the voltage brought back up. The disconnector marked with a red circle is open during normal operation, but could be used if the converters would be rated higher than their normal operating limit and one of them broke down, then the other one could export some of the power from the radials connected to the faulted converter, and as such be able to export more than 50 % of the total wind farm power until repairs could be made.

Utilising four converter as seen in figure 3.8 would result in a reliable wind farm since it would be unlikely that power production would drop below 75 % of rated. If the converters were rated to 80 MW instead of 64 MW, then even if a converter failed, 100 % of power supply could be maintained. This could be achieved by utilising the disconnectors shown in red circles, which allow any of the four subradials to be reconnected to the rest of the system in case of converter failure.

For this thesis, if not otherwise stated, the substation layout in figure 3.6 will be used.

### 3.1.6 Disconnectors and other Switchgear

Disconnectors have to be placed in such a way in the PCN, that every system component which requires maintenance can be isolated from the rest of the system. This concerns converters at the substation, radials, turbines and even the individual cables connecting the turbines so parts of the radial can be taken out for service. Figure 3.9 shows the various placements of disconnectors.

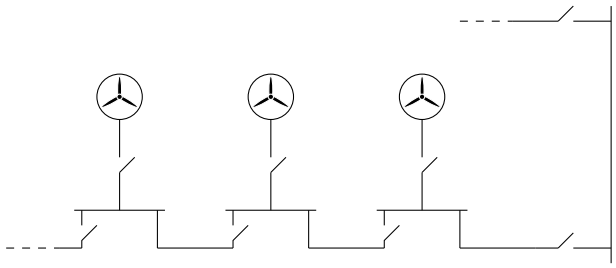

**Figure 3.9:** Possible disconnector placement

Ultimately the placement will be based on what is required by way of reliability and maintenance, disconnecting a whole radial just to work on a single turbine would be to costly. The more disconnectors and breakers are placed, the probability of a higher continuous power supply increases, but so does the cost. For the design of the DC wind farm, the focus will be on having as few components as possible to reduce cost, so no breakers, but only the disconnectors that are essential for maintenance will be considered. These are the turbine, radial and substation disconnectors. This decision is based on the fact that in a fault case, only the energy stored in the system, capacitors, inductors and cables, will contribute to the fault current. The substation cannot import power and all the turbines have DC/DC converters which contribute to faults. When simulation work is concluded it will be seen if this assumption holds true or if changes are required.

## 3.2 Cable sizing

This section aims at dimensioning the MVDC cables for the PCN. First, the theory required to calculate the dimensions of the MVDC cables will be presented. Subsequently the results are shown and discussed.

### 3.2.1 Thermal design - Conductor Sizing

The thermal design follows the procedure in [18]. It refers to finding the proper conductor size which will allow the desired amount of power to flow, but without compromising the cables thermal limits. A cable is heated by its power losses which are calculated as equation 3.3. The resistance of the conductor is temperature dependent and is given by equation 3.4.

$$P_L = I^2 R \tag{3.3}$$

$$R = R_{20°C}(1 + \alpha(\Theta_C - 20°C)) \tag{3.4}$$

Where $R_{20°C}$ is the resistance of the conductor at 20 $°C$, $\alpha$ is the temperature coefficient of the conductor material and $\Theta_C$ is the maximum conductor temperature.

To find the ampacity, the thermal resistances of the different layers must be found. $T_1$ is the thermal resistance of the insulation layer, $T_2$ of the layer between the metal sheath and armour, $T_3$ of the outer

sheath and $T_4$ is the thermal resistance between the ocean floor and the surface of the cable. These are calculated by equations 3.5 through 3.8.

$$T_1 = \frac{\rho_T}{2\pi} ln\left(\frac{D_o}{D_i}\right) \tag{3.5}$$

$$T_2 = \frac{\rho_T}{2\pi} ln\left(1 + \frac{2t_2}{D_s}\right) \tag{3.6}$$

$$T_3 = \frac{\rho_T}{2\pi} ln\left(1 + \frac{2t_3}{D_a}\right) \tag{3.7}$$

$$T_4 = \frac{\rho_T}{2\pi} ln(2\frac{2L}{D_e}) \tag{3.8}$$

$\rho_T$ is the materials specific thermal resistivity, $D_i$ is the conductor radius, $D_o$ is from the centre of the conductor to the outer insulation layer, $D_s$ is outer diameter of the metal sheath $t_2$ is the thickness of the metal sheath, $t_3$ is the thickness of the outer sheath, $D_a$ is the outer diameter of the armour, $L$ is the length from the ocean floor to the outer diameter of the cable, $D_e$ is the cable diameter.

Having found the thermal resistances and the conductor resistance, the ampacity of the cable can be calculated by equation 3.9.

$$I_A = \left(\frac{\Delta\Theta}{R'(T_1 + T_2 + T_3 + T_4)}\right)^{0.5} \tag{3.9}$$

$\Delta\Theta$ is the difference between the ambient temperature and the maximum allowable cable temperature.

Unlike in AC cables, skin and proximity effects are not relevant for the ampacity calculation.

### 3.2.2 Insulation

The electric field created by DC cables is dependent on the specific conductivity of the insulation, which in turn is dependent on both temperature and electric field strength, so $\sigma = \sigma(E, T)$. Following the method used in [20], an analytical approach for calculating the electric field can be done by utilising equation 3.10.

$$E(r) = \frac{\delta U_0 (r/r_o)^{\delta - 1}}{r_o(1 - (r_i/r_o)^{\delta}} \tag{3.10}$$

Where $U_0$ is the design voltage, $r_i$ is the conductor radius, $r_o$ is the radius from the centre of the conductor to the outer insulation layer. $\delta$ is defined by equation 3.11.

$$\delta = \frac{\frac{a\Delta T}{ln(r_i/r_o)} + \frac{bU_0}{r_o - r_i}}{1 + \frac{bU_0}{r_o - r_i}} \tag{3.11}$$

$\Delta T$ is the temperature difference between maximum conductor temperature to ambient, $a$ is the temperature coefficient of the insulations electrical conductivity, $b$ is the electric field coefficient of the electrical conductivity of the insulation.

Since the electric field is temperature dependent, it is important to see what the limits are for ambient temperature (no load condition) and the maximum operating temperature. Plotting the results of equation 3.10 for both temperature limits as a function of the distance to the centre of the cable will show the electric stresses which the insulation must be able to withstand. To illustrate this, figure 3.10 depicts the results for a cable with 175 $mm^2$ cross section and 11.8 $mm$ insulation thickness when applying a voltage of 30 kV. The x-axis is limited by the beginning and end of the insulation.

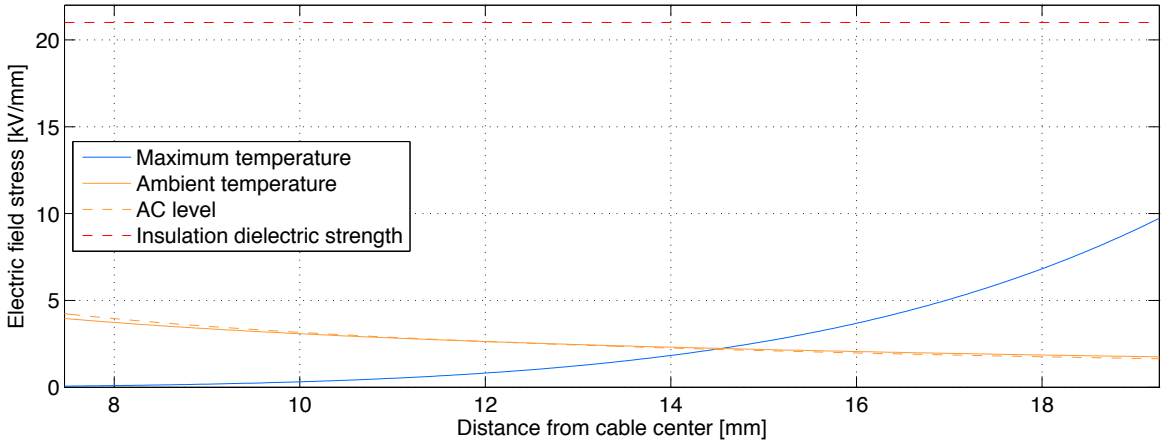


**Figure 3.10:** Electric field stress by radius

From figure 3.10 it is clearly seen that the field stress rises exponentially when the cable is operating at maximum temperature, but is actually lower when closer to the conductor compared to the field generated at ambient temperature. The AC field stress is shown for comparison. It can clearly be seen that under load, a DC cable has to withstand considerably higher stresses, hence the insulation needs to be thicker for similar safety margins. The dielectric strength of XLPE amounts to 21 kV/mm [21] and represents the maximum allowable electric stress that the insulation can handle.

For the design of the insulation it has to be ensured that the stresses in the insulation are lower than the dielectric strength for all operating conditions to avoid electric breakdown. The thicker the insulation, the lower is the maximum stress in the layer.

### 3.2.3 Remaining Layers

Apart from conductor and insulation, the cable consists of two semiconductor layers, sheath, separation sheath between sheath and armour, armour and an oversheath. The thicknesses of these layers are determined according to the recommendation given for medium voltage AC cables in the Danish standard IEC 60502 [22], as summarised in appendix A.3.
It is assumed that these recommendations are applicable for DC cables as well. However, it is necessary to validate that the developed cable is able to withstand stresses that are to be expected during operation in the offshore WPP. This will be done subsequently to the transient simulations conducted in chapter 5.

### 3.2.4 Results

Based on the theory explained above, required cable designs for different possible system voltage levels are determined. The procedure is explained in more detail in appendix A.4.

For the layout of the wind farm, 2 different cable cross sections are selected depending on the voltage level. On each feeder, the cables that connect the outer turbines have to conduct less current, as they have to transmit the power of only one or two turbines towards the substation during normal operation, and can therefore be of a smaller cross section than the cables closer to the substation, which support the power of three and four turbines of each feeder. It is shown in appendix A.5 which cable sections feature which cross section.

Graph 3.11 presents the cross sections for the cables in the PCN depending on the voltage level of the cable, i.e. $10\ kV$ corresponds to $\pm 10\ kV$, $20\ kV$ to $\pm 20\ kV$ and so on.

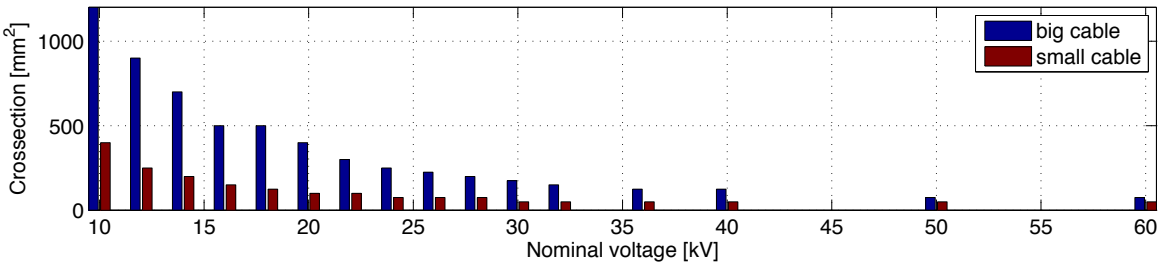


**Figure 3.11:** Required conductor cross sections depending on the cable voltage

The decision for a voltage level and subsequently the required cables depends next to technical aspects on the possibilities to manufacture and install the equipment and on economic considerations. Choosing a larger cross section, for example, will reduce conduction losses and line voltage drops, but on the other hand increase material consumption, cost and weight of the cables. Likewise, the selection of a higher array voltage may decrease conduction losses and required conductor cross sections on the one hand, but increase the thickness of the insulation layer and cost of other equipment connected to the PCN, for which higher voltage ratings are typically connected with higher costs.

For the loss analysis in section 3.3.2 three possible system voltages are regarded. They are 16 kV, 30 kV and 60 kV. Table 3.1 summarizes the calculated layer dimensions for these cases.

| | $A_{cond}$ | $r_{ins} + r_{semic}$ | $r_{pb-sheath}$ | $r_{sep-sheath}$ | $r_{armour}$ | $r_{outer-sheath}$ |
|---|---|---|---|---|---|---|
| 16 kV big cable | 500 | 7.9 + 1.5 | 2.0 | 1.5 | 2.5 | 2.9 |
| 16 kV small cable | 150 | 7.1 + 1.5 | 1.6 | 1.2 | 2.5 | 2.4 |
| 30 kV big cable | 175 | 11.8 + 1.5 | 1.9 | 1.5 | 2.5 | 2.8 |
| 30 kV small cable | 50 | 10.2 + 1.5 | 1.6 | 1.2 | 2.5 | 2.4 |
| 60 kV big cable | 75 | 18.0 + 1.5 | 2.2 | 1.6 | 2.5 | 3.1 |
| 60 kV small cable | 50 | 17.2 + 1.5 | 2.1 | 1.5 | 2.5 | 3 |

**Table 3.1:** Calculated values of cable layer dimensions for system voltages of $\pm 16\ kV$, $\pm 30\ kV$ and $\pm 60\ kV$, A in $mm^2$, all others in mm

From chapters 4 onwards, a system voltage of $\pm 30\ kV$ will be regarded. The resulting cable designs for the 50 $mm^2$ and the 175 $mm^2$ cable are shown in figure 3.12.

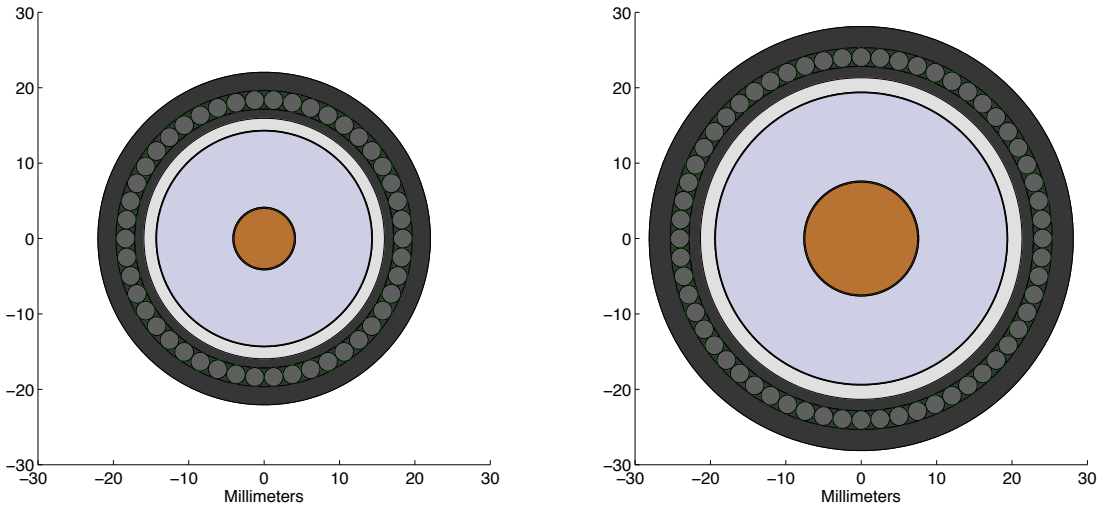


**(a)** Cross section of the 50 $mm^2$ cable

**(b)** Cross section of the 175 $mm^2$ cable

**Figure 3.12:** Comparison of the two MVDC cables designed for the wind farm

In figure 3.10 it was seen that the cables insulation stresses increased with temperature, so minimising the conductor size to save copper increases insulation size since the conductor is designed up to the allowable temperature limits. The cables dimensions could be optimised to meet certain criteria, but for this thesis focus has been on reducing the amount of copper. After the simulations have been made with the cables, their design will be discussed. The final design of any cable will be decided by a mixture of factors such as, copper savings vs. power loss, conductor size vs. insulation size and also general availability of existing cable sizes and what they cost.

## 3.3 Energy Production and System Losses

### 3.3.1 Annual Energy Production

The rated power of every turbine being $8.0\ MW$, the rated capacity of the WPP amounts to $256\ MW$. However, the power output of a wind turbine depends on the wind speed, therefore it is often smaller than the rated power.

Consequently, data of the wind speed distribution for the WPP site is required in order to determine the annual energy produced in the plant. Wind speed distribution can be estimated with the Weibull probability density function [23]:

$$p(v_{wind}) = \left(\frac{k}{C}\right)\left(\frac{v_{wind}}{C}\right)^{k-1} exp\left[-\left(\frac{v_{wind}}{C}\right)^{k}\right] \tag{3.12}$$

In equation 3.12 $p(v_{wind})$ is the probability that the wind speed $v_{wind}$ occurs, $k$ is a shape factor and $C$ is a scale factor. For offshore WPP sites, $k \approx 2$. $C$ can be calculated from equation 3.13, where $\Gamma$ is the gamma function and $\bar{v}_{wind}$ is the average annual wind speed [23].

$$C = \frac{\bar{v}_{wind}}{\Gamma\left(1 + \frac{1}{k}\right)} \tag{3.13}$$

Assuming its availability to be $100\%$, the annual WPP energy distribution is given by equation 3.14, $E(v_{wind})$ being the annual energy output of the plant and $P_T(v_{wind})$ being the turbine's power output

related to $v_{wind}$.

$$E(v_{wind}) = 32 \cdot p(v_{wind}) P_T(v_{wind}) \cdot 8760\ h \tag{3.14}$$

Finally, the annual energy production of the WPP $E_{WPP}$ is found by integrating equation 3.15 and multiplying with the amount of turbines:

$$E_{WPP} = \int E(v_{wind})\ dv_{wind} \tag{3.15}$$

Figure 3.13 (top) shows the turbine output power depending on the wind speed, having a cut-in wind speed of $4\ m/s$ and a cut-off wind speed of $25\ m/s$. Consequently, the results for $E_{WPP}$ depending on the annual average wind speed $\bar{v}_{wind}$ are presented in figure 3.13 (bottom). The values compare to a theoretical maximum of 2243 $\frac{GWh}{year}$ which would be produced when the turbines always operate at rated power.

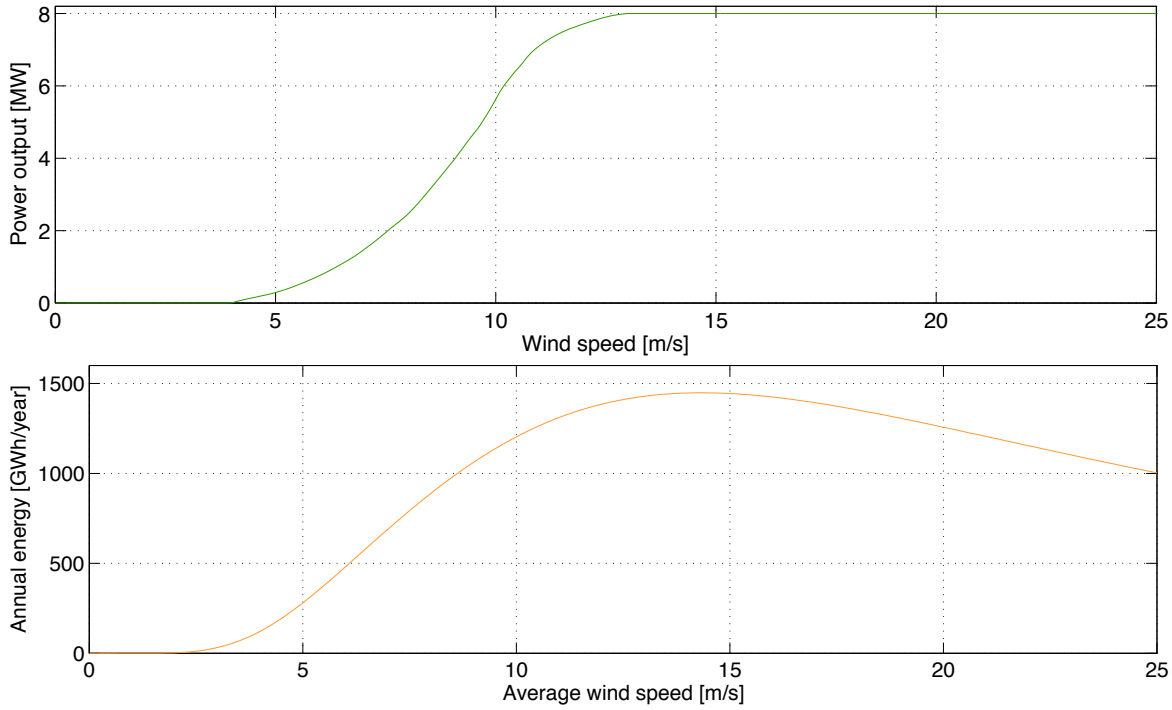


**Figure 3.13:** Wind turbine power curve [6] (top) and annual energy production of the WPP depending on annual average wind speed (bottom)

### 3.3.2 Conduction Losses

Conduction losses in the PCN are calculated following an adapted version of the Gauss-Siedel method, taking into consideration that losses in a DC system are purely resistive. Furthermore, cable heating and the resulting change of conductor resistivity are taken into account. The algorithm is described in appendix A.5.
Three possible system voltages are considered: $\pm 16\ kV$, $\pm 30\ kV$ and $\pm 60\ kV$. It can be expected, that losses decrease with increasing voltage level, since less current is required to transmit the power from the turbine to the substation. Likewise, it is to be expected that the relative voltage drop along the feeder cables is lower for higher rated system voltage.

Before the losses are regarded, nodal voltages in the system in steady are reviewed, with the substation as slack bus. The maximum voltages at any node in the PCN are depicted in figure 3.14 as a function

of delivered turbine power. It can be seen that the maximum voltage drop in the system amounts to 2.1% in a 16 kV system, 1.7% in a 30 kV system and 0.7% in a 60 kV system. This is well within typical voltage limitations of $\pm$ 10%.

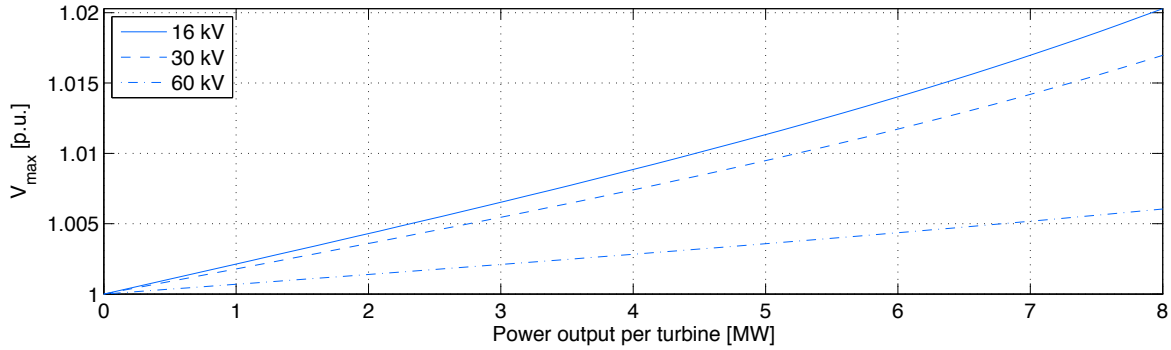


**Figure 3.14:** Maximum nodal voltage in the system for a substation voltage of 1.0 p.u.

Figure 3.15 depicts losses and temperatures of every cable section (compare figure 3.3 in section 3.1), given that the turbines deliver rated power.

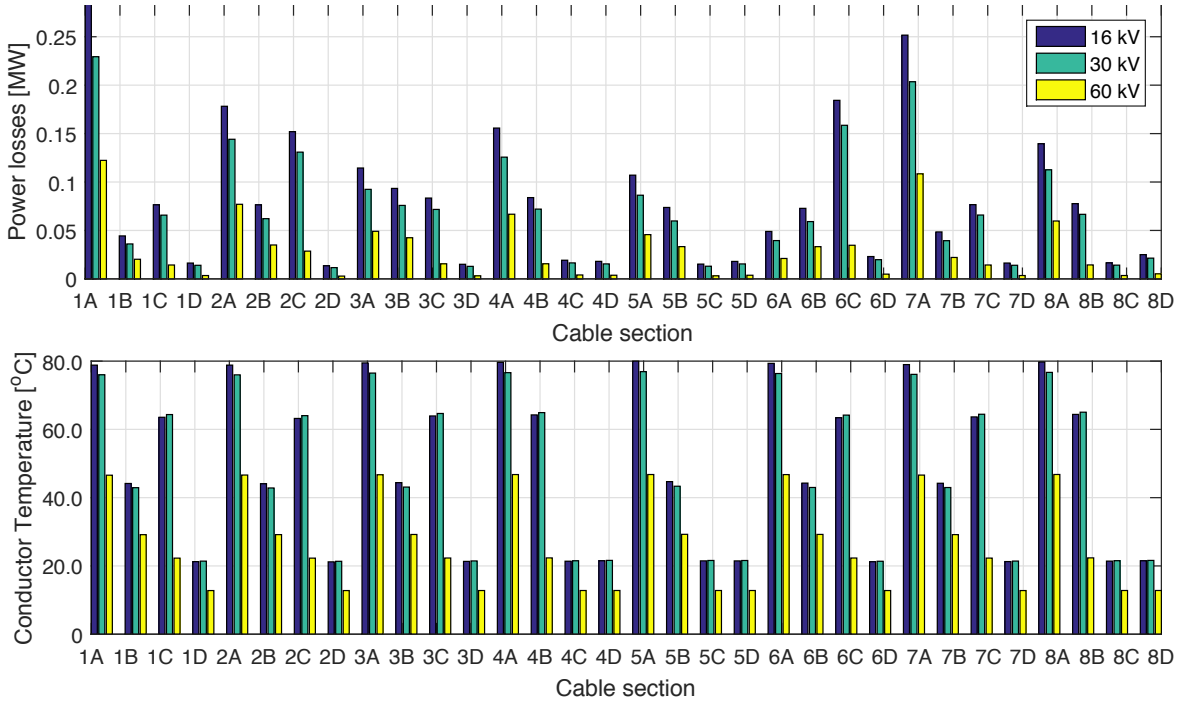


**Figure 3.15:** Absolute power losses (top) and conductor temperature (bottom) for every cable section for turbines delivering $P_{rated}$

It can be seen that the losses are highest for section 1A, which owes to the length of the cable. They amount to 283.6 kW in case of the 16 KV system, 229.4 kW in case of the 30 kV system and 122.4 kW in case of the 60 kV system.
Regarding the temperature, the sections that connect the feeders to the substations reach the highest values for all voltage levels. Between the feeders, the temperatures are similar. Section 5A reaches the highest temperatures for system voltages of 16 kV and 30 kV with 81.832°C and 78.6792°C respectively. For the 60 kV system, section 8A is warmest, reaching 47.8597°C for full turbine power output.

Subsequently, figure 3.16 depicts the rise in temperature that the warmest cable section 5A and the coldest cable section 2D experience depending on $P_{turb}$.

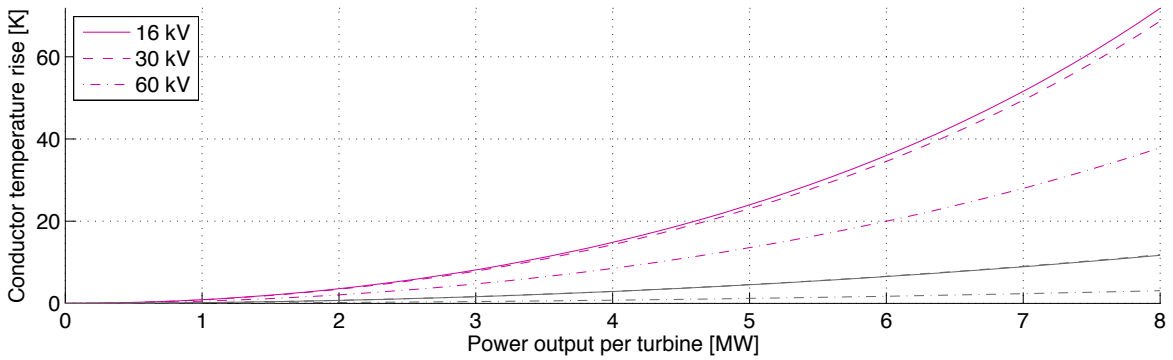


**Figure 3.16:** Temperature rise compared to ambient temperature (10°C) in cable section 5A

The total system losses, which are the sum of all cable section losses, are presented in 3.17 in dependence of $P_{turb}$. For nominal voltage at the substation the losses are depicted in purple, however the highest losses can be expected for the minimum substation voltage of 0.9 p.u. (depicted in grey) and nominal turbine power output, as this case leads to the highest current flows in the system.

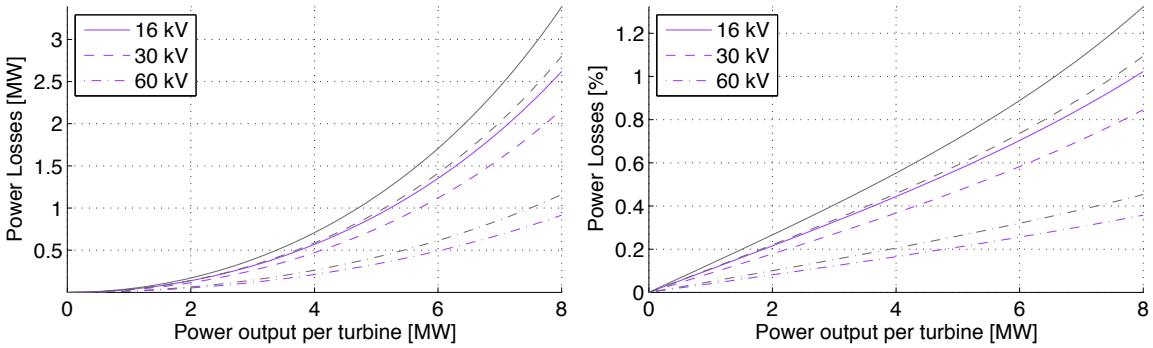


**Figure 3.17:** Cable losses in absolute values (left) and as a fraction of output power of the WPP (right) for $U_{sub} = 1\ p.u.$ (purple) and $U_{sub} = 0.9\ p.u.$ (grey)

The maximum values for the system losses are summarized in table 3.2

| | 16 kV [MW] | 16 kV [%] | 30 kV [MW] | 30 kV [%] | 60 kV [MW] | 60 kV [%] |
|---|---|---|---|---|---|---|
| 1.0 p.u. | 2.619 | 1.023 | 2.166 | 0.846 | 0.915 | 0.358 |
| 0.9 p.u. | 3.387 | 1.323 | 2.801 | 1.094 | 1.159 | 0.453 |

**Table 3.2:** System losses for turbine power of $P_{rated}$ and substation voltage of 1.0 and 0.9 p.u. respectively

For better evaluation of the losses with respect to the power and annual energy production of the WPP (compare figure 3.13 in subsection 3.3.1), power and annual energy losses are depicted as a function of wind speed in figure 3.18. It can be seen that the share of system losses increases with higher average wind speed. For the compared voltage levels losses are lower than 1% of the annually produced energy.

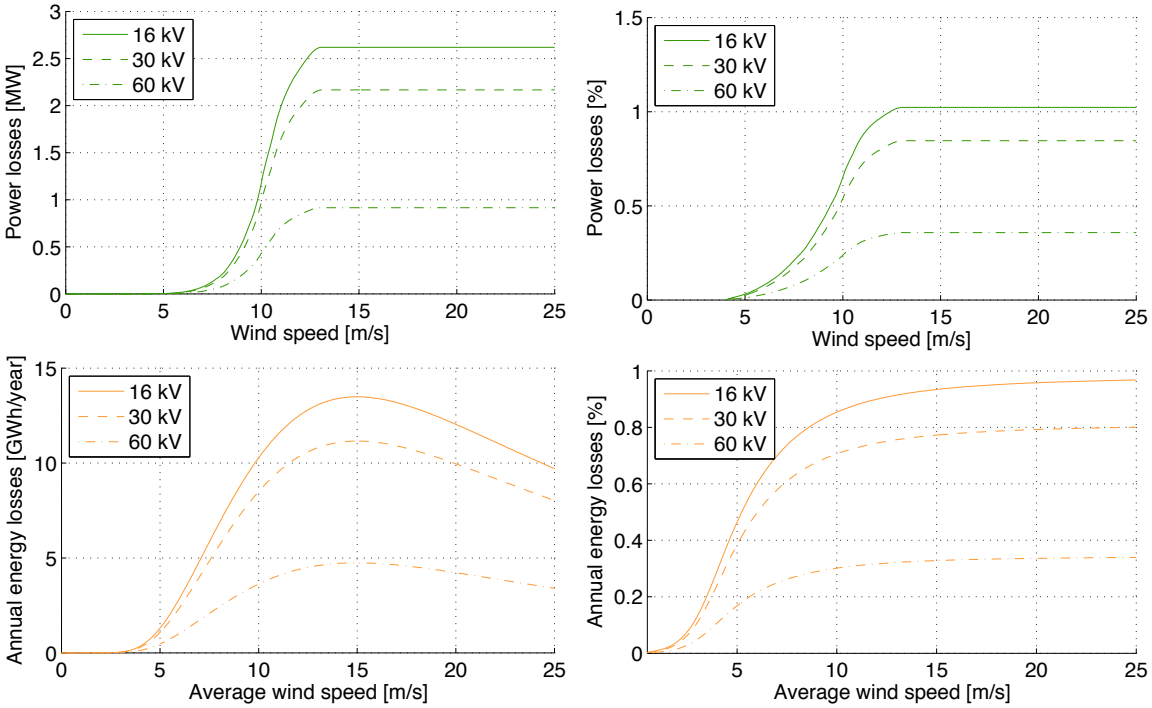


**Figure 3.18:** Power losses (top) and annual energy losses (bottom) of WPP in absolute values (left) and percentage of total production (right)

## 3.4 Conclusion & Outlook

Concluding this chapter, a design for a possible future DC power collection network in offshore WPPs has been proposed. The focus was placed on following aspects:

- Identification of major changes between AC and DC wind farm concept
- DC cable design
- Conduction loss estimation depending on PCN voltage level

Main changes between the AC and the DC system design are:

- **Substation platforms** - It was seen that for the AC network two substations were needed, but only one in the DC network.
- **Cables** - AC networks utilise three cable phases, where the DC networks operate with two phases. As different physical principles play a role in AC and DC power transmission, especially regarding ampacity and electric field stresses in the insulation, cables rated for AC currents cannot be utilized without further ado. Instead MVDC cables will be used.
- **Power train** - The power train used in AC systems contains an AC/AC converter and a transformer, where the DC power train contains a rectifier and a DC/DC converter.
- **Protection equipment** - The AC wind farm contained breakers and disconnectors, where the DC equivalent may only need the disconnectors required for maintenance.

For cable design, required layer dimensions for given conductor cross sections and voltage levels have been calculated based on field strength withstand requirements of the insulation material and the Danish standard IEC 60502-2. Subsequently, cables ampacities have been determined based on thermal restrictions given by the cable heating in steady state operation.
As skin and proximity effects do not have to be considered in the DC case, the total cross section of

the conductors can be kept smaller compared to AC cables. On the other hand, electric stresses in the insulation is less uniform than in AC cables, requiring a thicker insulation layer.
The generated cable data has been compared with requirements of the system to transport power through the cables resulting in minimum allowable cable sizes for every possible system voltage.

Finally, power and expected annual energy production of the WPP has been analysed with respect to the available wind resources and compared to cable losses, which can be expected for the different system voltages and respective cable sizes. As expected, higher system voltages lead to lower conduction losses in the PCN and therefore a higher efficiency of the WPP. Furthermore, the temperatures which every cable section reaches during steady state operation when the turbines operate at rated power have been calculated.

Obviously, the aspects discussed in this chapter constitute only a fraction of all consideration that need to be taken when designing the offshore collection grid, as was already discussed in the project limitations in chapter 1.4. Future work regarding the system design aspects dealt with in this project should in the first place focus on two aspects.
First of all, cable sizing is an iterative process. Section 3.2 shows the first step, focussing on conductor and insulation sizing based on steady state system parameters and preselected safety margins. Next, it is necessary to test if all cable layers can withstand stresses caused by transient operation. This will be done subsequently to the transient simulations conducted in chapter 5, closing the first iteration of the design process. Furthermore, the cable design was based on predefined choices regarding possible voltage levels, conductor cross sections and materials, leaving potential for optimisation in further design iterations.
Secondly the design of protection, switchgear and the arrangement of electrical equipment and connections on the substations has only been briefly discussed and requires further considerations. Again, this will be picked up later in the project in chapter 5.

For the following chapters of this work, a system voltage of $\pm 30\ kV$ will be regarded. The system parameters resulting for this voltage level are summarized in table 3.3. Capacitor sizes are calculated according to equations 3.1 and 3.2.

| | |
|---|---|
| Power rating of turbines | 8 MW |
| Power rating of wind farm | 256 MW |
| MVDC voltage level | $\pm$30 kV |
| Capacity of turbine capacitors | 444.444 $\mu$F |
| Capacity of substation capacitors | 14222.2 $\mu$F |

**Table 3.3:** System Parameters of the

# Control 4

This chapter presents an approach to control the power collection network. First, a generic description of the control is presented. Afterwards, the utilized models the cable and systems are described. Next, the approach of realising the control strategy and is derived. Finally, the concept is implemented in a reduced model of the PCN to validate its functionality.

## 4.1 Generic Description

The PCN's main task is to collect the power generated by the wind turbines and to transmit it from the individual turbine converters to the offshore substation converter, from where it is sent to shore via the HVDC link. In order to accomplish this objective, the control scheme of the system must fulfil the following tasks:

- The WT is supposed to deliver the amount of power $P_{ref}$ that is requested, if the total available power is sufficient.
- The system stability of the proposed offshore grid has to be ensured. This means that the grid voltage has to stay within allowed limits during all operation conditions. Over currents in the PCN are not expected, as it is connected solely to power electronic converters, which are controlled to limit their current flows to 1 p.u. to avoid damaging their semiconductor components.

### 4.1.1 Limitations

The development of the control scheme is subject to the following limitations:

- The power reference $P_{ref}$ is assumed to be set with regard to the wind speed, therefore power contained in the wind is sufficient to provide $P_{ref}$.
- The voltage at the input of the substation converter is regarded as stiff.
- Linear control theory is applied, so non-linearities are linearised for the system analysis and controller design.

### 4.1.2 Working Principle

In order to provide $P_{ref}$ to the PCN, the current output $I_{turb}$ of the turbine converter has to be adjusted depending on the output voltage $U_{turb}$, which in turn is a function of current flow through the PCN and the voltage at the substation $U_{sub}$. Consequently, the current has to follow the relation $I_{turb} = \frac{P_{ref}}{U_{turb}}$, provided that this allows both $I_{turb}$ and $U_{turb}$ to stay within the allowed range of operation.

For the converter current this range of operation is given by a minimum of 0 and a maximum of $I_{rated}$, defined by $I_{rated} \approx \frac{P_{rated}}{0.9\, U_{rated}}$. A temporary over current of up to 120% to 150% might be permissible for up to 50 ms during transient operation. For the converter voltage, the range of operation is given by $U_{rated} \pm 10\%$ during 95% of the time in accordance with EN50160.

However, two conditions may occur which would cause these limits to be exceeded when providing $P_{ref}$. Firstly, an under voltage from the substation can cause $I_{turb}$ to exceed its upper limit in order to provide $P_{ref}$ and secondly an overvoltage from the substation converter can cause an overvoltage in $U_{turb}$, as the current flow from the turbines towards the substation will lead to a voltage increase in the PCN towards the turbines. In both cases, $I_{turb}$ has to be limited and thereby the power output $P_{turb}$ of the turbine will be smaller than $P_{ref}$.

The concept of the control is depicted in figure 4.1. It consists of a power control loop, which takes a voltage measurement and transforms it into a current reference for the turbine with regard to $P_{ref}$, and a voltage limiter, which determines a current reduction signal $I_{red}$ to avoid violation of the upper voltage limit.

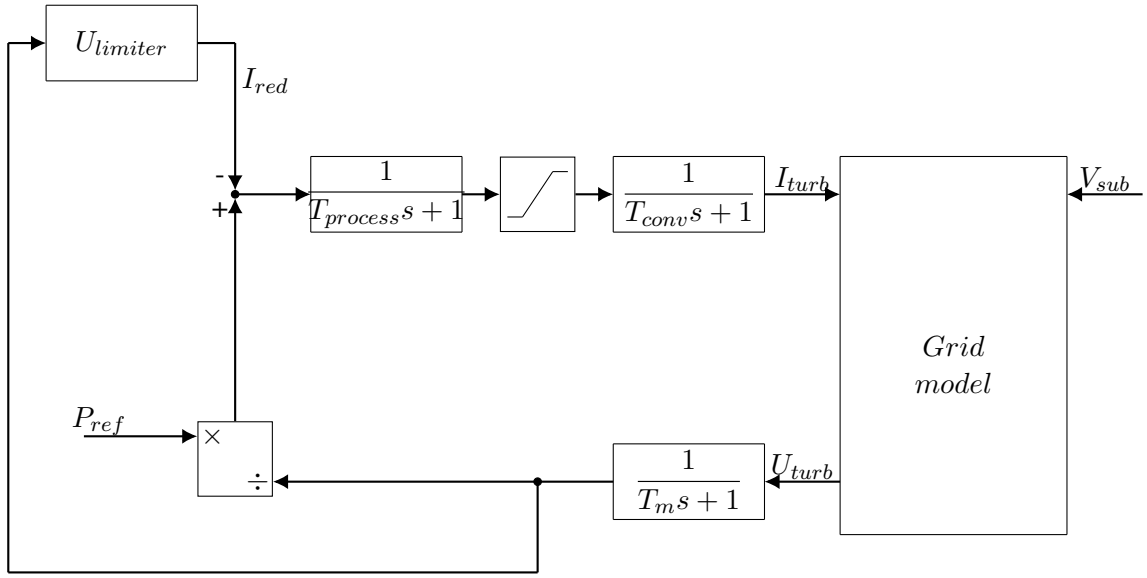


**Figure 4.1:** Concept of turbine control

The power control follows a decentralized approach, which means it is implemented for each turbine individually without regard to the other turbines. The voltage limiter however, will be implemented at the most upstream turbine of every feeder only. Its $I_{red}$ signal will be transmitted to the turbines downstream the same radial. Consequently, all turbines will adjust their current output by the same amount.

### 4.1.3 Communication and Measurements

Currents and voltages at the turbine are measured. For the voltage measurements a time delay $T_m$ is present. Furthermore, a processing time $T_{process}$ for the calculation of required $I_{turb}$ values is taken into account. Communication is required from the last turbine of each feeder to the turbines situated downstream in order to send a current reduction signal in case of overvoltage in the feeder.

## 4.2 Model

The implementation of the control requires a model of the designed cable. Two types of models are utilized in this chapter:

- A linearised transfer function model is used to derive and analyse the control concept.
- A PLECS model is used to investigate influences of system nonlinearities and for validation of the concept in an entire feeder.

As mentioned above, control is implemented at each turbine individually. Consequently, the analysis of the system and derivation of its control is conducted with a simplified system model, consisting of one turbine, the offshore substation and the cable connection in between. The single line representation is shown in figure 4.2.

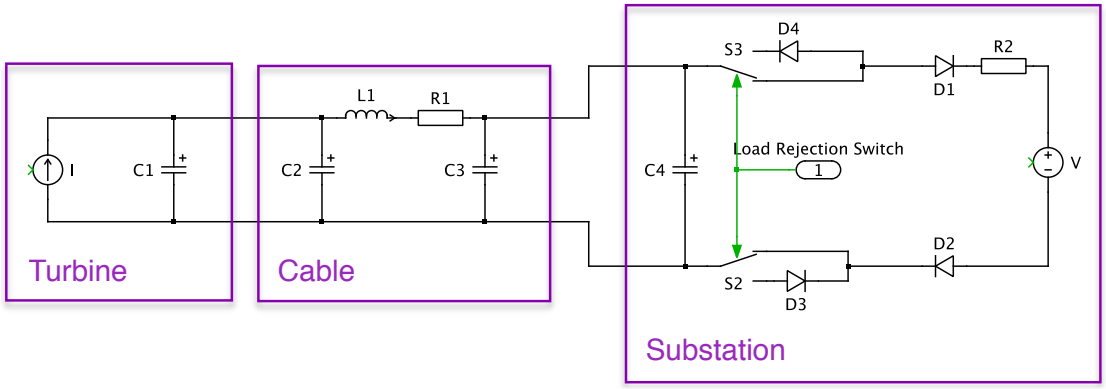


**Figure 4.2:** PLECS Model of the System

In the model, the wind turbine is modelled as a controllable current source, which is connected in parallel to its converter output capacitance. In addition, the control of the current source will feature a time delay $T_{conv}$, representing the inductance of the transformer coils in the DC/DC converter (compare figure 3.5 in chapter 3.1). A single pi-link is used to model the cable. The offshore substation is represented by a stiff voltage source, ideal diodes are implemented to ensure that power flow is unidirectional. The resistance is necessary only for modelling purposes in PLECS and has a value close to zero. The next subsection presents the derivation of the cable model parameters from the cable's layout.

### 4.2.1 Pi-Model Parameters

For controller design, each cable segment, i.e. the connection between two turbines or from one turbine to the substation, is represented as a single pi-link, as shown in figure 4.2.

Subsequently, the calculation of the single line diagram parameters $R$, $L$ and $C$ is presented. The conductor resistance $R$ is given by equation 4.1, with $\rho$ being the specific resistivity of copper, $A$ the cross section and $l$ the length of the cable.

$$R_{conductor} = \frac{\rho_{20°C}}{A} l \tag{4.1}$$

The cable capacitance $C$ is calculated according to equation 4.2 [17]. In the equation, $R_o$ represents the outer insulation radius over the semiconductor layer, $R_i$ the radius over the conductor and $\varepsilon_0 = 8.85 \times 10^{-12}\ \frac{F}{m}$ is the permittivity of the vacuum and $\varepsilon$ is derived from equation 4.3. Since the pi-model features two parallel capacitances to ground, each of them will amount to $\frac{C}{2}$.

$$C_{cable} = \frac{2\pi\varepsilon\varepsilon_0}{ln\left(\frac{R_o}{R_i}\right)} l \tag{4.2}$$

In order to take into account the semiconductive layers inside and outside of the insulator, its permittivity is adjusted as shown in equation 4.3 [17]. In the equation $b$ is the outer insulation radius

without the semiconductor layer, $a$ the inner insulation radius over the inner semiconductor layer and $\varepsilon_{xlpe} = 2.3$ [20, p. 91].

$$\varepsilon = \varepsilon_{xlpe} \frac{ln\left(\frac{R_o}{R_i}\right)}{ln\left(\frac{b}{a}\right)} \tag{4.3}$$

The inductance of the two cable phases is calculated in equation 4.4.It is composed of the inner and outer inductance of the conductor, with the vacuum permeability $\mu_0 = 4\pi \times 10^{-7}\ \frac{H}{m}$, the material specific relative permeability $\mu$, conductor radius $R_i$ and distance $d$ between the axes of positive and negative phase conductor. The proposed PCN is installed with positive and negative phase cables touching each other. As the calculated inductance is with respect to both phases, the single line diagram inductance amounts to $\frac{L}{2}$.

$$L_{cable} = \frac{\mu_0 \mu}{\pi} \left(\frac{1}{4} + ln\frac{d}{R_i}\right) l \tag{4.4}$$

Resulting from equations 4.1, 4.2, 4.3 and 4.4, the pi-model values of the small and big cable can be calculated and are presented in table 4.1.

| | $R\ [\Omega/m]$ | $\varepsilon$ | $\frac{C}{2}\ [F/m]$ | $\frac{L}{2}\ [H/m]$ |
|---|---|---|---|---|
| big cable | $9.6 \times 10^{-5}$ | 2.6420 | $7.2011 \times 10^{-11}$ | $4.6253 \times 10^{-7}$ |
| small cable | $3.36 \times 10^{-4}$ | 2.7429 | $5.5773 \times 10^{-11}$ | $5.4192 \times 10^{-7}$ |

**Table 4.1:** Calculated values of pi-model components

### 4.2.2 Transfer Function of DC link

For the development of the current control, transfer functions of the system described above are derived, with system inputs $I_{turb}$, $U_{sub}$ and system output $U_{turb}$. This leads to equations 4.5 and 4.6, with $C_{12} = C_{turb} + C_C$ and $C_{34} = C_{sub} + C_C$

$$\frac{\Delta U_{turb}}{\Delta U_{sub}} = \frac{1}{1 + s(R_{sub}C_{34} + C_{12}R_C + C_{12}R_{sub}) + s^2(C_{12}(L + R_{sub}R_C C_{34})) + s^3 C_{12}R_{sub}LC_{34}} \tag{4.5}$$

$$\frac{\Delta U_{turb}}{\Delta I_{turb}} = \frac{R_C + R_{sub} + s(L + R_{sub}R_C C_{34}) + s^2(R_{sub}LC_{34})}{1 + s(R_{sub}C_{34} + C_{12}R_C + C_{12}R_{sub}) + s^2(C_{12}(L + R_{sub}R_C C_{34})) + s^3 C_{12}R_{sub}LC_{34}} \tag{4.6}$$

Figure 4.3 depicts the step responses of the turbine voltage to a step in $I_{turb}$ and $V_{sub}$ respectively.

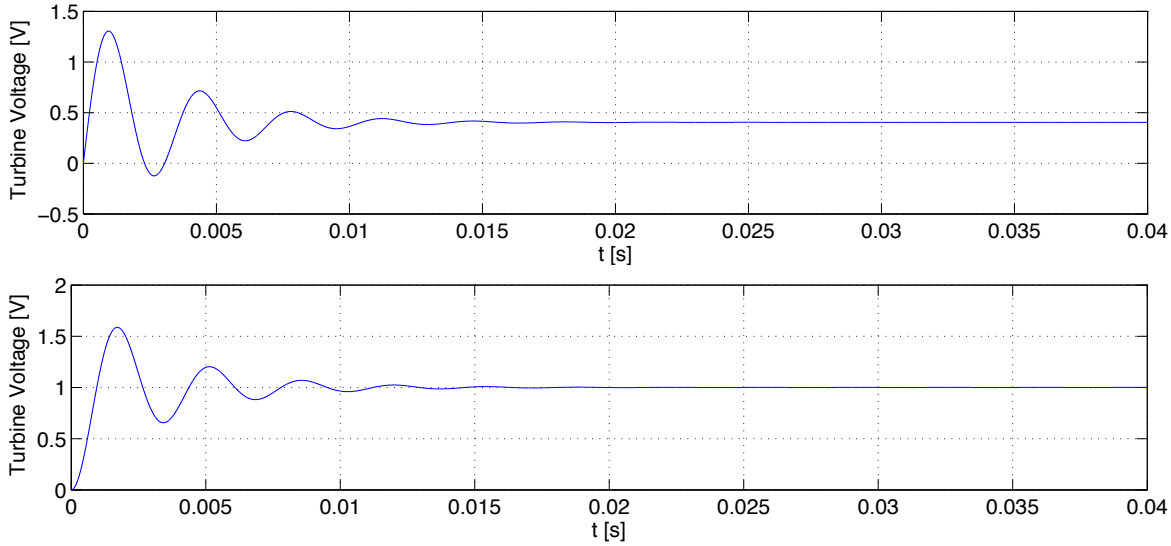


**Figure 4.3:** Step response of $U_{turb}$ to a 1 A step in $I_{turb}$ (top) and to a 1 V step in $U_{sub}$ (bottom)

It is shown that a step in $I_{turb}$ of 1 $A$ results in a steady state change of 0.4 $V$ in $U_{turb}$. The overshoot of the step response amounts to 221.5% and the settling time to 13.3 ms. A step in $U_{sub}$ of 1 $V$ results in a steady state change of 1 $V$ in $U_{turb}$, with an overshoot of 58.3% and settling time of 12.3 ms.

Determination of the system poles, which are all within the left half of the s-plane, shows that the system is BIBO stable.

## 4.3 Control Analysis

In order to derive and analyse the control, linear control theory is applied. First, the power control loop will be regarded in subsection 4.3.1, without consideration of nonlinearities such as unidirectional power flow and current or voltage limitation. Subsequently, the voltage limiter is designed and described in subsection 4.3.2. In both cases, the transfer function model of the system is utilized.

### 4.3.1 Power Control Loop

For the implementation of the control scheme, the terms $I_{turb} = \frac{P_{ref}}{U_{turb}}$ and $P_{turb} = U_{turb} \cdot I_{turb}$ need to be linearised, as shown in equations 4.7 and 4.8, where the index 0 indicates the point around which the relation is linearised.

$$I^0 + \Delta I = \frac{P^0_{ref} + \Delta P_{ref}}{U^0 + \Delta U} \quad \Rightarrow \quad I^0 = \frac{P^0_{ref}}{U^0} \quad \& \quad \Delta I = \frac{1}{U^0}\Delta P_{ref} - \frac{P^0_{ref}}{U^{0^2}}\Delta U \tag{4.7}$$

$$P^0 + \Delta P = (U^0 + \Delta U)\cdot(I^0 + \Delta I) \quad \Rightarrow \quad P^0 = U^0 I^0 \quad \& \quad \Delta P = U^0 \cdot \Delta I + I^0 \cdot \Delta U \tag{4.8}$$

This leads to the linearised transfer function model depicted in figure 4.4, which calculates the change in system outputs $\Delta I_{turb}$, $\Delta U_{turb}$ and $\Delta P_{turb}$ with regard to a change in system input $\Delta P_{ref}$ or a change in the disturbance $\Delta U_{sub}$.

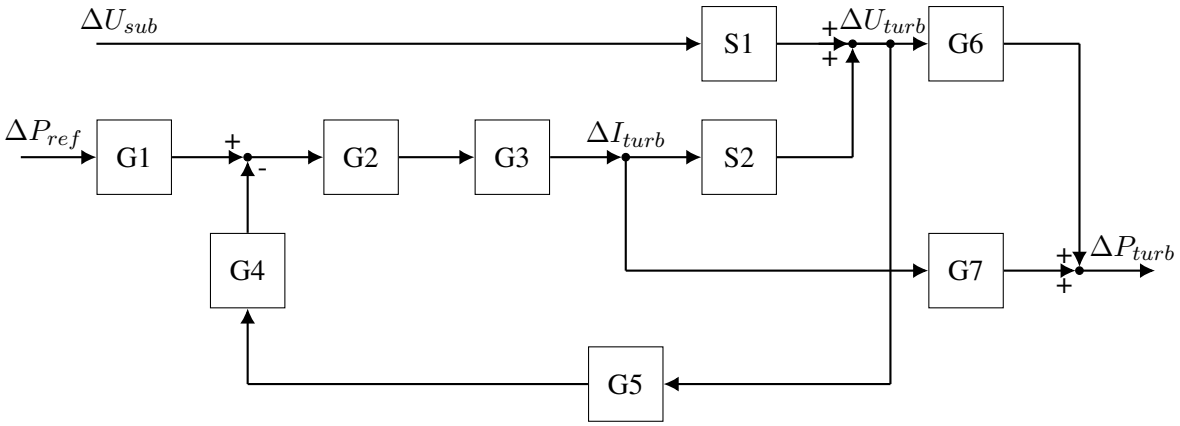


**Figure 4.4:** Transfer function

The transfer functions of the system are defined in table 4.2.

| S1 | S2 | G1 | G2 | G3 | G4 | G5 | G6 | G7 |
|---|---|---|---|---|---|---|---|---|
| $\frac{\Delta U_{turb}}{\Delta U_{sub}}$ | $\frac{\Delta U_{turb}}{\Delta I_{turb}}$ | $\frac{1}{U^0}$ | $\frac{1}{T_{process}s+1}$ | $\frac{1}{T_{conv}s+1}$ | $\frac{P^0}{U^{0^2}}$ | $\frac{1}{T_m s+1}$ | $I^0$ | $U^0$ |

**Table 4.2:** System transfer functions of figure 4.4

Resulting from this, the transfer functions from $P_{ref}$ and $U_{sub}$ to the system outputs are given in table 4.3.

| | $\Delta I_{turb}$ | $\Delta U_{turb}$ | $\Delta P_{turb}$ |
|---|---|---|---|
| $\Delta P_{ref}$ | $\frac{G_1G_2G_3}{1+G_2G_3G_4G_5S_2}$ | $\frac{G_1G_2G_3S_2}{1+G_2G_3G_4G_5S_2}$ | $\frac{G_1G_2G_3\cdot(G_7+G_6S_2)}{1+G_2G_3G_4G_5S_2}$ |
| $\Delta U_{sub}$ | $\frac{-G_2G_3G_4G_5S_1}{1+G_2G_3G_4G_5S_2}$ | $\frac{S_1}{1+G_2G_3G_4G_5S_2}$ | $\frac{S_1(G_6-G_2G_3G_4G_5G_7)}{1+G_2G_3G_4G_5S_2}$ |

**Table 4.3:** Reduced system transfer functions

For the time constants the values presented in table 4.4 are assumed from this point on.

| $T_{conv}$ | $T_{process}$ | $T_m$ |
|---|---|---|
| 0.2 ms | 0.5 ms | 1 ms |

**Table 4.4:** Time constants of the controller

Determination of the system poles, which are all within the left half of the s-plane, shows that the system is BIBO stable.

Subsequently, the systems step response in the worst case is depicted, which is defined by a 4 MW input step of the turbine power reference (figure 4.5) or a 6 kV disturbance step of the substation voltage (from 0.9 to 1.1 p.u or vice versa) (figure 4.6) respectively. The graphs show changes in the output values with respect to the initial value, therefore all curves start at zero.

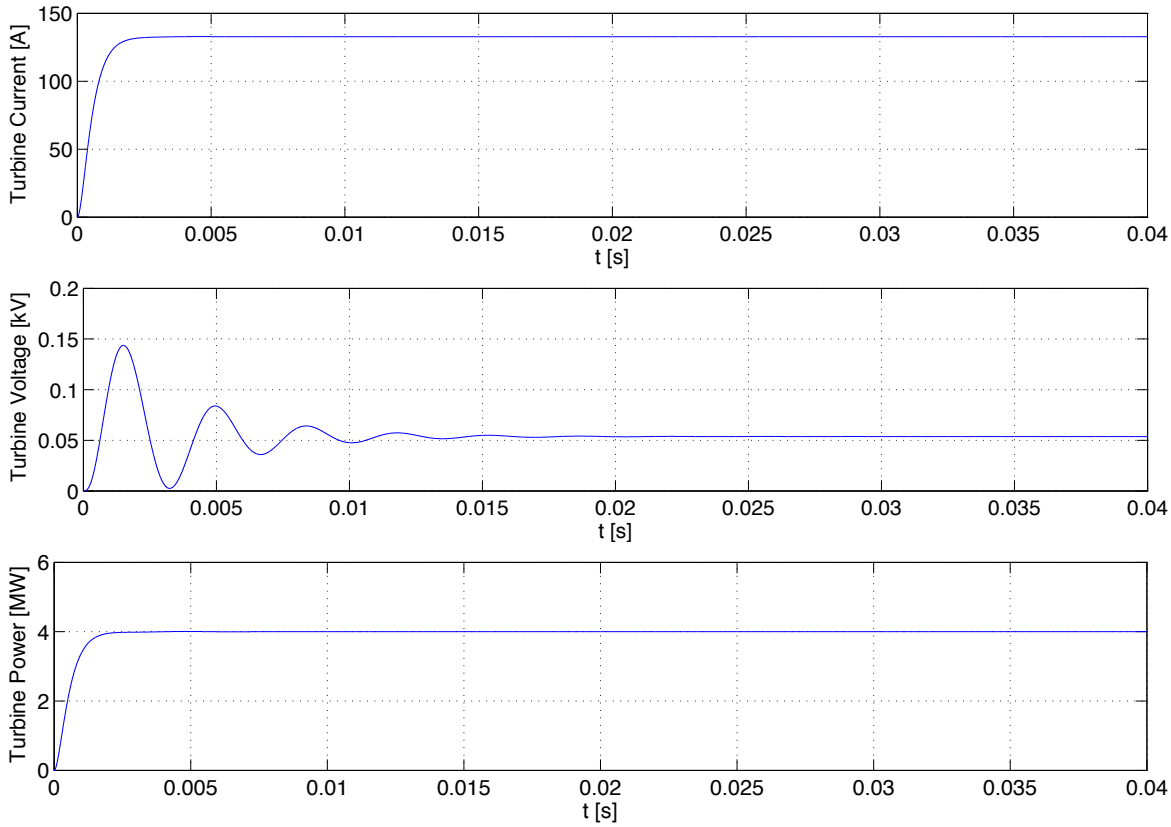


**Figure 4.5:** Step responses of $I_{turb}$ (top), $U_{turb}$ (center) and $P_{turb}$ (bottom) to a 4 MW step in $P_{ref}$

Figure 4.5 shows that the turbine current has an overdamped response to the change in power reference and settles within 2 ms at a steady state value of +132.86 A.
The turbine voltage, depicted in the middle, settles at +53.7 V and features an overshoot of 167.6% and a settling time of 13.8 ms. Even though this overshoot seems high, it is not problematic considering its short duration and the high rated voltage of the system, which is 30 kV and therefore the peak value corresponds to only 0.3% of $U_{rated}$.
However, the overshoot of $U_{turb}$ can be avoided by changing the power reference as a ramp input instead of a step. This is also a more realistic scenario during operation, as the power of a wind turbine can not be changed infinitely fast. A ramp up time of 200 ms is enough to reduce the overshoot to 1.3%.
Similar to $I_{turb}$, the turbine power, which is shown in figure the bottom graph, settles within 2 ms without an overshoot. The steady state value of $P_{turb}$ is +4 MW, which means that there is no steady state error between $P_{ref}$ and $P_{turb}$.
Summarising the observed properties, the step response to a change in $P_{ref}$ is precise, fast, stable and well enough damped, therefore it requires no further compensation or adjustment.

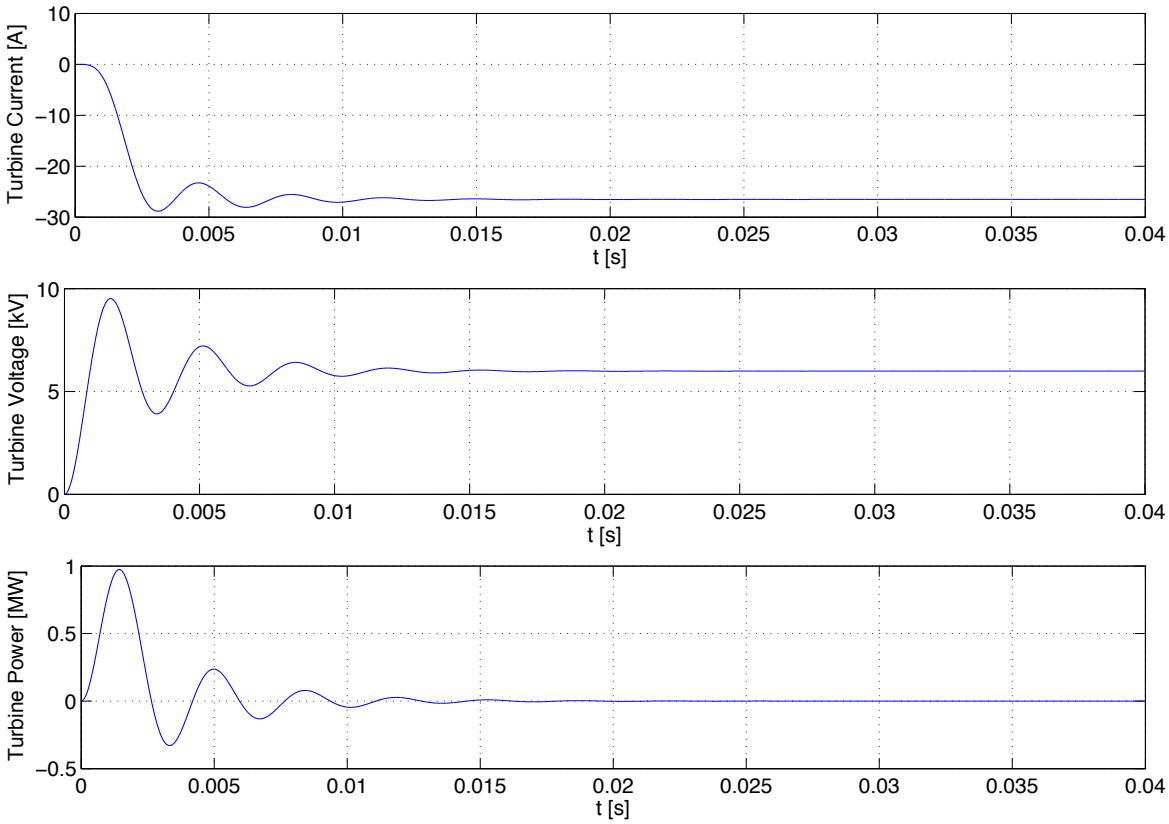


**Figure 4.6:** Step responses of $I_{turb}$ (top), $U_{turb}$ (center) and $P_{turb}$ (bottom) to a 6000 V step in $U_{sub}$

Figure 4.6 presents the response of $I_{turb}$ to a change in $U_{sub}$. Due to the increase in grid voltage, the turbine current drops. It settles within 10 ms at a steady state value of -26.5 A and features an overshoot of 8.7%.
The turbine voltage has an overshoot of 58.3% and settles within 12.3 ms at +5989 V. Finally, the $P_{turb}$ is depicted in the bottom of the figure. Even though the steady state change of the power is zero, it shows a transient response due to the changes and oscillations of $I_{turb}$ and $U_{turb}$. The settling time is defined by the settling time of $U_{turb}$, hence 12.3 ms. The peaks of the oscillations amount to +974 kW and -329 kW.

The observed overshoots of $U_{turb}$ and $P_{turb}$ may be of concern. For the regarded change in $U_{sub}$ the voltage is exceeding its upper limitation during the overshoot. However, it is of short duration and may be acceptable, if it cannot be reduced.
For $P_{turb}$, the peak value is almost a quarter of $P_{rated}$ It is questionable, if the power output from the turbine side of the converter can support that oscillation. Subsequently, it is analysed if the response to the disturbance can be improved by adjusting the controller.

Therefore, the system response to a voltage step of 6000 V at the substation converter is analysed with all time constants set to zero. This is to analyse the natural response of the system. Figure 4.7 depicts the step responses of $I_{turb}$, $U_{turb}$ and $P_{turb}$.

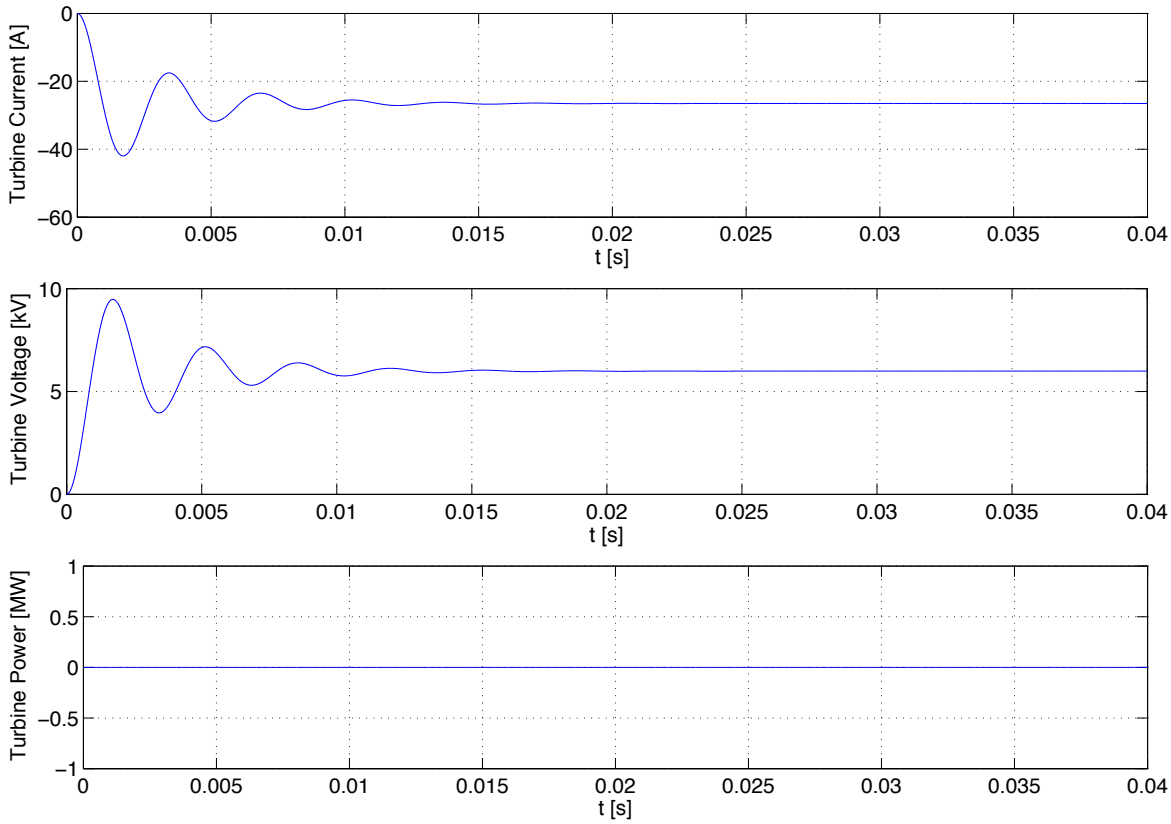


**Figure 4.7:** Step responses of $I_{turb}$ (top), $U_{turb}$ (center) and $P_{turb}$ (bottom) to a 6000 V step in $U_{sub}$, assuming no time delays from converter, processing and measurements

The figures show that without the additional time delays in the system, turbine current and voltage have the same natural frequency, which amounts to $f_{I_{turb}} = f_{U_{turb}} = 291.971\ Hz$. This means the current has now a faster response to the disturbance. Consequently, the turbine power shows no step response at all. It can be concluded that the cause for oscillation in the turbine power as a consequence of a disturbance in the substation voltage are no inherent feature of the ideal grid, but only introduced by the time constants. However, delays from converters, measurement and processing cannot be completely avoided. Choosing equipment with smaller time delays is recommended to improve the step response of $P_{turb}$.
The step response of $U_{turb}$ is almost the same as seen before in figure 4.6, which means that the time constant have no remarkable influence on it. Comparing to the response of the system transfer function model only, analysed earlier in subsection 4.2.2, which shows the same characteristics, it can be concluded that the disturbance cannot be suppressed by controlling the turbine converters. Instead, it is necessary to control the voltage at the substation, which is not in the scope of this project.

### 4.3.2 Voltage Limiter

The aim of the voltage limiter is to prevent the voltage from exceeding its upper limit of 1.1 p.u. by limiting the turbine power, and thereby the current flow from turbines to substation, which determines the voltage drop along the lines. Its structure is depicted in figure 4.8.

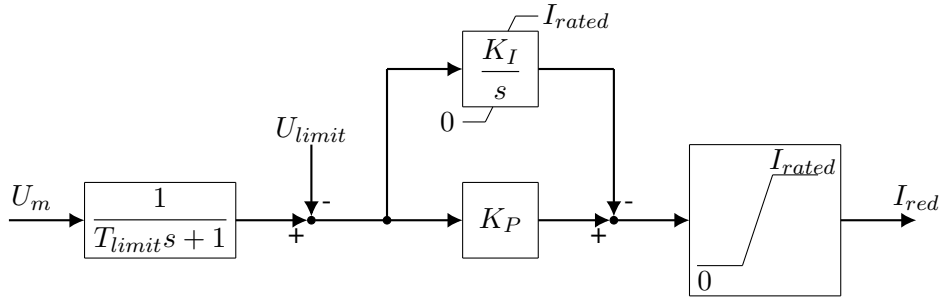


**Figure 4.8:** Concept of voltage limiter

The measured turbine voltage $U_m$ is passed through a lowpass filter in order to prevent oscillations in $I_{red}$. These might otherwise occur as a consequence of the voltage step response to a change in $V_{sub}$ or $P_{ref}$, both featuring an overshoot. The time constant $T_{limit}$ of the filter is therefore chosen with respect to the settling time of these step responses by $T_{limit} = \frac{1}{5}T_s$. The difference between $U_m$ and $U_{limit}$ is then passed through a PI controller with anti-windup in order to bring the voltage down to $U_{limit}$. The resulting current reduction signal $I_{red}$ is limited by $I_{rated}$. Furthermore, it has a lower limit of zero, as the limiter should only reduce current when necessary, but not increase current in order to try to lift the voltage towards the upper limit.

## 4.4 Implementation/Validation

This section presents simulation results when applying step changes to the system with implemented control. In subsection 4.4.1 the response is analysed when the control is applied to the linearised transfer function model of the system and compared to the results when using the PLECS model, which includes non linearities, such as the unidirectional power flow capability of the substation converter. Thereby, the change in dynamics due to this non linearities can be observed. Subsequently, in subsection 4.4.2, the control is implemented in an entire feeder of the WPP to detect possible control interactions of the turbines with each other.

### 4.4.1 Implementation in single Turbine to Substation Model

This subsection aims at analysing differences in the PCN behaviour when using the linearised transfer function model which was used to develop the control compared to the PLECS model, which represents the real system behaviour more accurately as it includes non linearities of its components. Possible problems arising due to these properties will be detected and resolved.

Three simulation cases are investigated:

- Step changes in $P_{ref}$
- Step changes in $U_{sub}$
- Sudden load rejection at the substation converter

First, changes in $P_{ref}$ are regarded. Regarding turbine current $I_{turb}$ and power $P_{turb}$ the step responses resemble those in section 4.3 for both transfer function and PLECS model as long as the voltage limit is not exceeded when the turbine provides $P_{ref}$.
However, $P_{turb}$ features an error with regard to $P_{ref}$ for the PLECS model. This error is due to the linearised control development approach. Error values are presented in table 4.5. They are calculated according to $error = \frac{P_{turb}-P_{ref}}{P_{ref}}$ and for the case of $P_{ref} = 0$ according to $error = \frac{P_{turb}}{P_{rated}}$. For regarding the errors, the voltage limiter is excluded from the control. The more the inputs $P_{ref}$ and $U_{sub}$ deviate from the linearisation point, which in this section is chosen as $P_{rated}$ and $U_{rated}$, the higher the error.

| | | $P_{ref}$ | | | | |
|---|---|---|---|---|---|---|
| | | 0 | 1 MW | 2 MW | 3 MW | 4 MW |
| $U_{sub}$ | 27 kV | 9.1% ($P_{rated}$) | +26.2% | +8% | +2% | -1% |
| | 28.5 kV | 4.8% ($P_{rated}$) | +14.3% | +4.6% | +1.3% | -0.25% |
| | 30 kV | 0.2% ($P_{rated}$) | +0.4% | +0.08% | +0.02% | 0 |
| | 31.5 kV | 0 | -15.5% | -5.4% | -2% | -0.25% |
| | 33 kV | 0 | -33.5% | -11.8% | -4.6% | -1% |

**Table 4.5:** Error in $P_{turb}$ depending on system input

Regarding the turbine voltage the PLECS system shows different behaviour than the transfer function model, as can be seen in figure 4.9 on the example of a step in $P_{ref}$ from 0 MW up to 4 MW and back to zero MW. When stepping down the power, the turbine output capacitor experiences a voltage drop below the settling value due to system dynamics. Because of the unidirectional power flow of the substation converter, no power can be imported to recharge the turbine capacitor. Therefore its voltage takes approximately 100 ms to reach steady state again, while it is recharged from the error turbine current. If there was no steady state error in $I_{turb}$, the voltage would stay at 29.9 kV until $P_{ref}$ is set higher again.

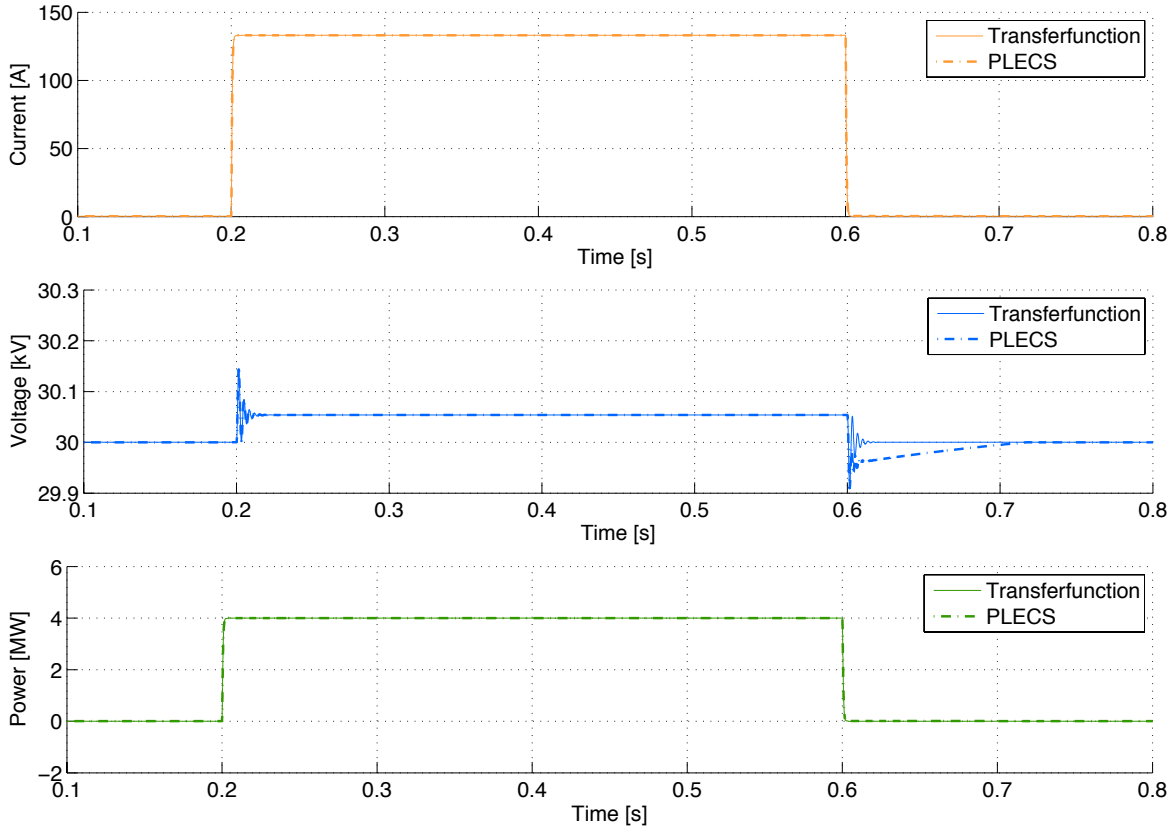


**Figure 4.9:** Current (top), voltage (center) and power (bottom) response to a step in $P_{ref}$ from 0 to 4 MW

Secondly, changes in $U_{sub}$ are regarded. Figure 4.10 depicts the example of a step change from 32.5 kV to 32.99 kV at the substation converter and back, showing the response of $I_{turb}$, $U_{turb}$ and $P_{turb}$ respectively. $P_{ref}$ is kept constant at 4 MW. For comparison the response is depicted for the control including and excluding the voltage limiter is presented.

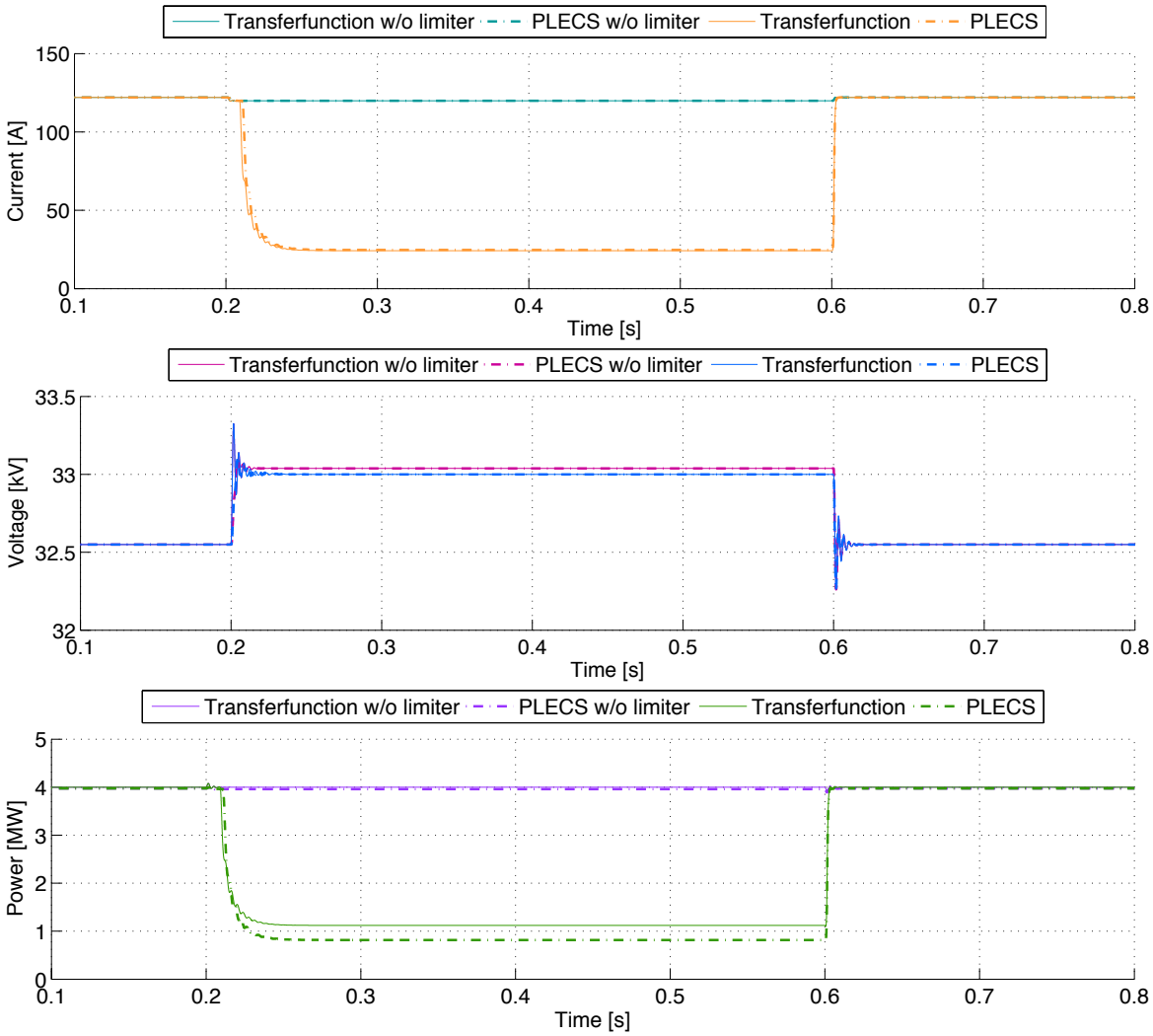


**Figure 4.10:** Current (top), voltage (center) and power (bottom) response to a step in $U_{sub}$ from 32.5 to 32.99 kV

The graphs show that without the voltage limiter, the power follows its reference, and therefore $U_{turb}$ exceeds its upper limit of 33 kV. As expected, $I_{turb}$ is only slightly reduced to maintain constant power. With the limiter, $I_{turb}$ goes down after the voltage exceeds its limit, settling when $U_{turb}$ reaches 33 kV. When the disturbance is over and $U_{sub}$ is set back to its rated value, current and power output resettle at their initial values. It can be concluded that the voltage limiter works properly.

Lastly, it is investigated on what happens in the case of a sudden load rejection at the offshore substation, when no power can be exported from the system any more but the turbine is operating with $P_{ref} > 0$ at the moment that the disturbance occurs. As in the previous case, responses of $I_{turb}$, $U_{turb}$ and $P_{turb}$ are depicted in figure 4.11.

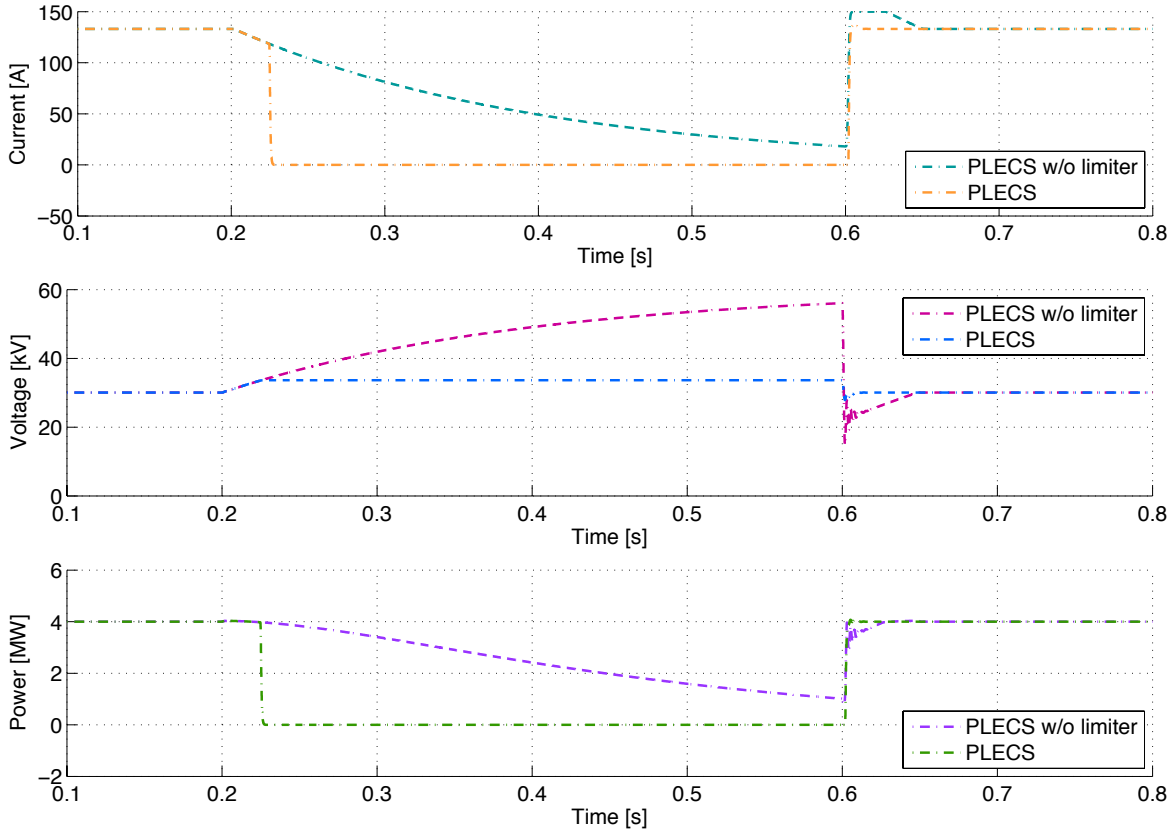


**Figure 4.11:** Current (top), voltage (center) and power (bottom) response to a load rejection at the substation

Without the limiter power it can be seen that the capacitors start charging at the moment of load rejection, since power cannot be exported. $I_{turb}$ goes down as $U_{turb}$ goes increased, in order to keep $P_{turb}$ constant. However, due to the linearised control derivation and the error connected to that $P_{turb}$ decays to zero as the voltage is rising. For the worst case, defined by an initial substation voltage of 27 kV, which results in the highest pre load rejection value of $I_{turb}$, $U_{turb}$ will reach 60.8 kV as $I_{turb}$ decays to less than 1 A within one second.
With limitation, the voltage rise is limited and stops at 33.6 kV which corresponds to 12.1% overvoltage. As soon as the voltage reaches 33 kV, the limitation kicks in. Due to the time delay correlated to $T_{limit}$, $I_{turb}$ continues to charge the capacitors in the system up to that value.
It can be concluded that power control and voltage limiter work properly.

### 4.4.2 Implementation in entire Feeder

Finally, an entire feeder is modelled, where the control is implemented for every turbine, in order to test the developed control scheme with regard to turbine interaction and to ensure that no hunting effects compromise its behaviour. Figure 4.12 depicts the PLECS model of the system.

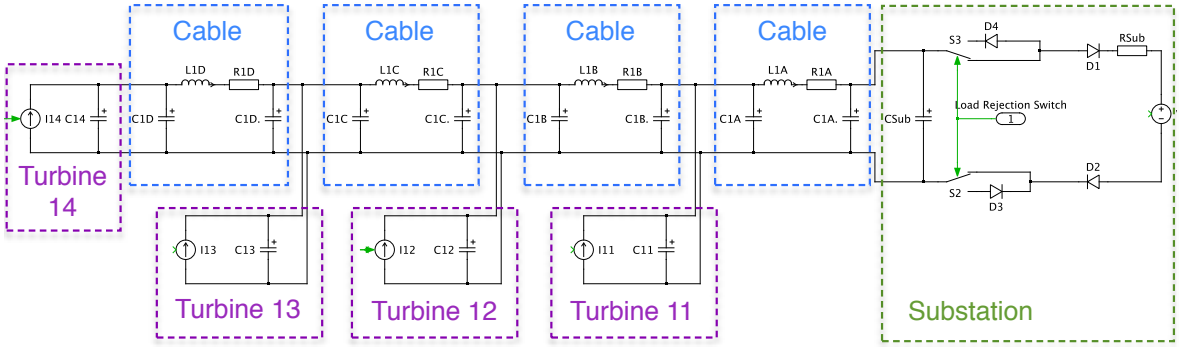


**Figure 4.12:** PLECS model of feeder one for control implementation

Within the feeder, the control loop for the power output is implemented for every turbine individually. The control loop that reduces current to prevent over voltage is reacting to a voltage measurement at turbine 14, since this turbine is the furthest from the substation and hence most likely to experience over voltages. The current reduction signal $I_{red}$ from turbine 14 is sent to the other turbines, which all reduce their output accordingly, until the voltage settles within limits.
The regarded cases are the same as in subsection 4.4.1. Subsequently, simulation results are presented and explained. The graphs show turbine current, voltage and power for all turbines of the feeder.

First, changes in $P_{ref}$ are regarded. As to be expected, the voltage is higher towards the end of the feeder. No hunting effects are observed and turbine response dynamics vary only in magnitude but not in frequency. In general, the same properties as in the single turbine case in subsection 4.4.1 can be observed.

Secondly, changes in $U_{sub}$ are regarded. Figure 4.13 depicts the example of a step change from 32 to 32.9 to 32.8 kV at the substation converter, showing the response of $I_{turb}$, $U_{turb}$ and $P_{turb}$. $P_{ref}$ is kept constant at 4 MW. Again, the response is depicted for the control including and excluding the voltage limiter is presented.

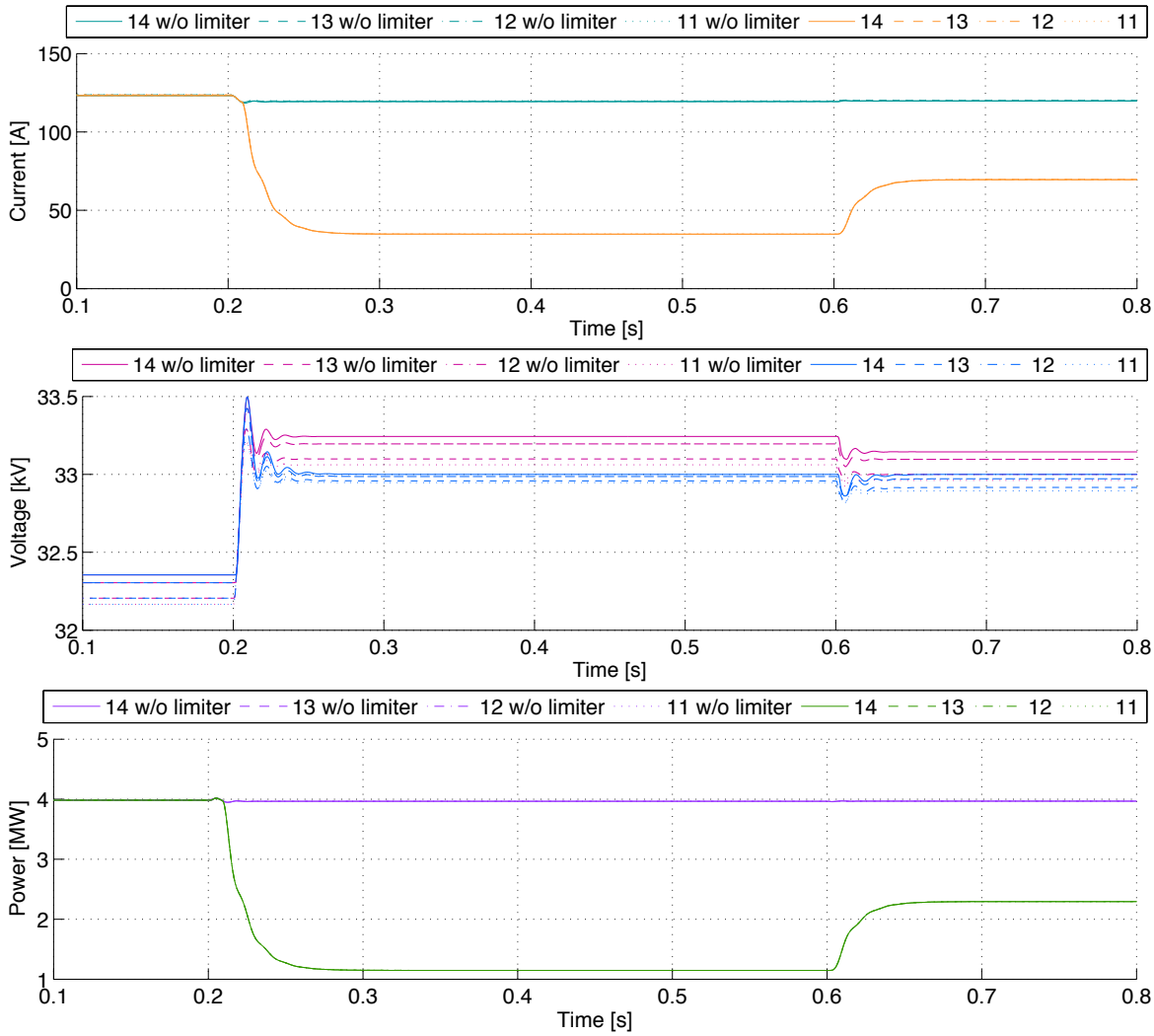


**Figure 4.13:** Current (top), voltage (center) and power (bottom) response to a step in $U_{sub}$ from 32 to 32.9 to 32.8 kV

It can be seen that the current and hence turbine power are limited, when $I_{turb}$ would otherwise exceed its upper limit. At 0.6 seconds $U_{sub}$ is reduced by 100 V. As a result, $I_{turb}$ increases as much as $U_{turb}$ allows it. It can be concluded that the voltage limiter works as desired, and reduces the power not more than it is required by the voltage boundaries.
For the observations of the voltage limiter, communication delay of the $I_{red}$ signal is not considered. If this delay would be included, it should be faster than the time delay given by $T_{limit}$ and should be also included for the turbine at the end of the feeder, where the limiter is implemented, in order to avoid hunting effects.

The load rejection case shows the same characteristics as described for the single turbine case in subsection 4.4.1. As in the other cases, no hunting effects can be observed.

## 4.5 Conclusion & Outlook

Concluding this chapter, a control scheme for the grid has been developed, which features following properties:

- The control operates with a power reference as an input and takes into consideration disturbances of the substation voltage. It has the wind turbine converter current as an output, which in turn determines the voltage at the converter output capacitors and consequently also the power output.
- The control follows a given power reference, as long as no current or voltage limitations are violated. However, due to the application of linear control theory in its development, steady state errors occur, the more the values of $U_{sub}$ and $P_{ref}$ deviate from the point of linearisation. While these errors stay below 1% when $U_{sub}$ is at 1 p.u., they can reach values up to a third of $P_{ref}$, when $P_{ref}$ is small and the substation voltage is at its maximum. For future work, this could be improved by applying nonlinear control theory and considering a feedback of the turbine power in the control design.
- A voltage limiter loop is implemented, which dictates to reduce the current if this is necessary to maintain the voltage within its allowed limits. The limiter works as desired for normal grid operation. In case of a sudden load rejection at the offshore substation it reduces the power output of the turbine converters to zero. Due to time delays in the control, the voltage in the system rises above the upper limit before it settles. In worst case the settling voltage is 2% above the upper voltage limit.

Future work regarding the control of the PCN should include the development of the substation converter control, in order to control the substation voltage and thereby avoid the large overshoots in the turbine voltages that were observed in section 4.2 and 4.3 in the step responses to a change in $U_{sub}$. Furthermore, the steady state error in $P_{turb}$ will be minimized by avoiding deviations from the rated voltage at the substation. Subsequently, investigation of its interactions with the turbine converter control developed here will be necessary.

# Transient Analysis 5

In this chapter the transient properties of the wind farm will be explored, and in order to accomplish this a model of the wind farm will be designed in PSCAD.

## 5.1 Aim of the chapter - Questions to Solve

The main questions which need to be answered by way of this chapter are listed here.

#### Grounding strategy

In any electrical system the grounding strategy is an important factor to consider. In this specific application the voltages and currents induced in both sheath and armour of the cables in the system will depend heavily on how, if at all, they are grounded. Different grounding strategies will be simulated and to find the most suitable grounding for the cables.

#### Highest stresses for cable dimensioning

In order to find the maximum possible stresses on the cables, several simulations will be done. These will included normal operation with step-up and step-down, balanced and unbalanced faults at various locations to find the worst cases. This information will then be compared to the cable design to see if they will tolerate the voltage stresses and heating. To ensure that the worst cases will be found, simulations will be made at maximum and minimum allowable substation voltage.

#### Protection scheme

Having simulated the various fault scenarios it will become clear if a protection scheme will be required for the system. The amplitude and duration of both current and voltage will be analysed to see if a protection scheme can be designed based on control features only, or if physical components, such as breakers and surge arrestors, will need to be installed in the system.

## 5.2 Simulation Model

The overall simulation model designed in PSCAD has the same layout as figure 5.1. The two radials on the bottom left are fully represented and the other six are lumped together. This was done in order to keep the model within the license limits, and also to reduce simulation time considerably. The turbines are represented by current sources and the sub-station as a voltage source.

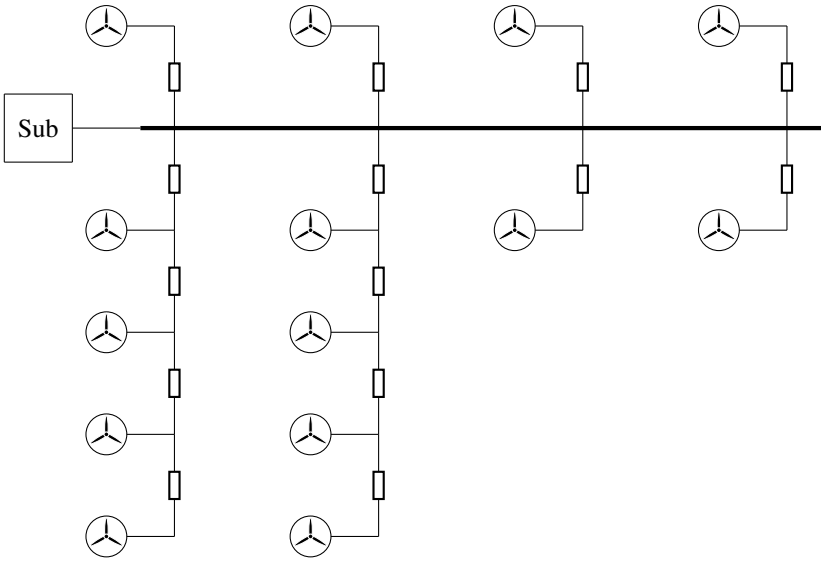


**Figure 5.1:** Simulation mode layout in PSCAD

### 5.2.1 Component Representation in PSCAD

In order to easily show how the different components of the wind-farm are represented in PSCAD, a simple one turbine, one cable system has been made which can be seen in figure 5.2. The component ratings seen on the figure do not represent the actual values which will be used in the complete model.

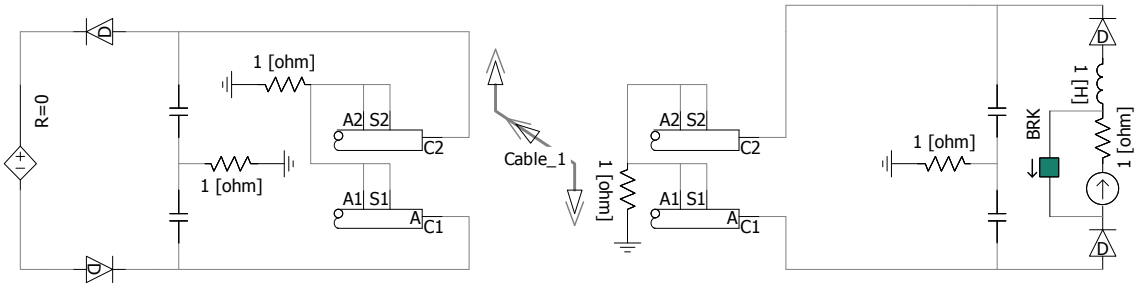


**Figure 5.2:** PSCAD model representation

There are three main components which need to be considered:

- **Substation** - The substation has been modelled as a voltage source and two capacitors act as an input filter. The diodes are added to ensure that the substation does not supply power to the system.
- **Submarine cable** - Cable_1 as seen in the middle of the figure, contains the actual cable model and settings. On its left and right side are the cable interfaces which enable the conductors to be connected to system and are marked as C1 and C2. There are also A and S, which is the armour and sheath. These are grounded together in this figure, but can be grounded in any number of ways, or not at all.
- **Wind turbine** - The wind turbine is represented by a current source, an inductor and capacitors to simulate the output filter and transformer. The breaker is added to be able to shut the turbine on or off and the resistor, which will have a very low value, is added for program stability.

### 5.2.2 Cable model implementation

The cable model used in PSCAD is the frequency dependent in phase model, which is described in section A.1 in the appendix. The graphical interface of the cable model can be seen in figure

5.3, where the settings for the radii of the various layers, depth below surface and translation from centre are entered. Translation from centre is used when having multiple cables in the same model. Material constants such as permittivity, permeability and resistivity are entered for the insulating and conducting layers.

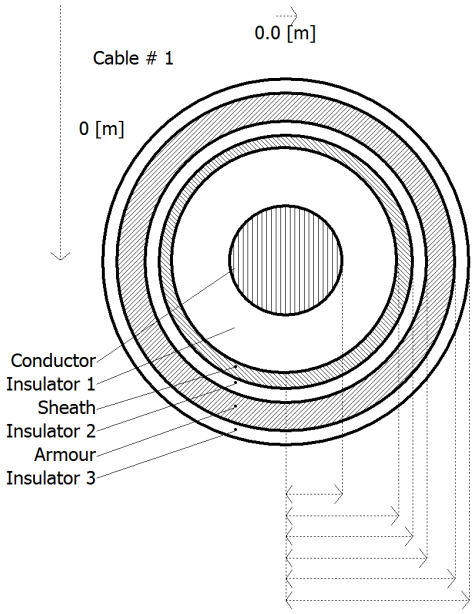


**Figure 5.3:** PSCAD cable model

### 5.2.3 DC fault types

DC faults which occur on wind farms can be sorted into three different levels, turbine generator, connection grid and transmission level. For the specific devices the faults can be further defined as; DC cable faults, junction faults and inner converter faults. The turbine generator and the inner converter faults are product specific and usually have some built in protection, which will not be explored further. Figure 5.4 illustrates the different locations for the faults on the lines and bus. The faults can be from pole to pole or pole to ground.

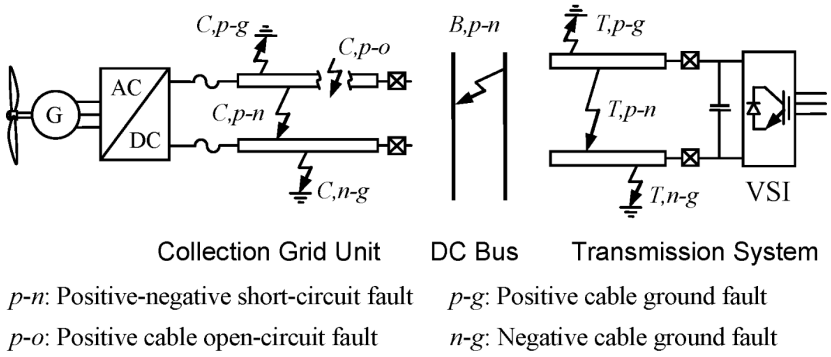


**Figure 5.4:** DC fault types

Cable faults are common and are usually caused by insulation breakdown or deterioration, the causes for these kinds of faults include physical damage, which can cause some of the most serious short circuit faults, and environmental damage such as dampness at the cable terminals. Having the cables operating at too high loads, too high temperatures or if the cable is reaching the end of its lifetime, can also cause cable faults. [24]

## 5.3 Analysis of cable stresses

A small three turbine system has been designed in PSCAD with one 12 km long cable which has been divided in to six equal cable segments with voltage and current measurements at conductor, sheath and armour.

### 5.3.1 Aim

- This has been done in order to see the induced currents and voltages in the sheath and armour during normal and faulted operation, so the magnitudes and distribution along the cable can be examined. This will reveal the critical points to monitor in the complete model of the offshore wind farm.
- Different grounding strategies will be explored and compared to make a suitable recommendation for the wind farm.
- Finding the points with the highest measured currents and voltages in the sheath and armour are important for the dimensioning of the cable, as it has to withstand the highest possible stresses caused during normal operation, or faults, in another cable section.

### 5.3.2 Limitations

The observations in this section are subject to the following limitations:

- The substation converter is a single active bridge converter, which means it has a unidirectional power flow. Consequently the feeder can export but not import power.
- Three grounding strategies have been chosen, both cable ends grounded, one end grounded and no grounding. Sheath and armour are grounded through a common resistor at the cable ends.
- When conducting the faulted cases, four were chosen. Positive conductor to ground and balanced faults at turbine A and B. Other fault locations were seen to have similar or lower stresses on the cables.

### 5.3.3 Model

As described in section 5.3, a small system is modelled with a long cable split in to six separate sections as seen in figure 5.5. Each segment is 2 km long, also the ones at either end. The turbines are 8 MW and the substation voltage is $\pm$ 30 kV.

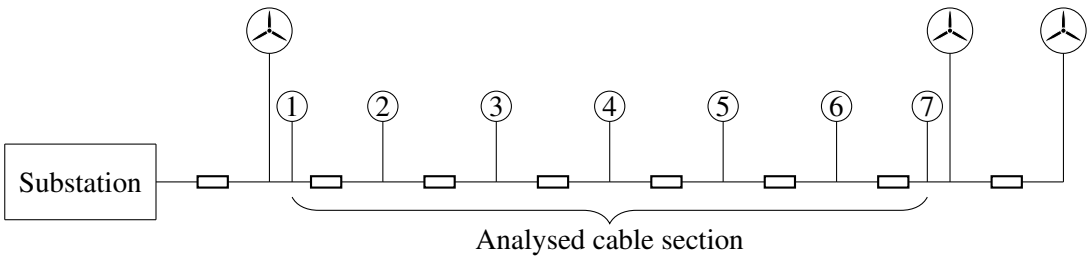


**Figure 5.5:** Feeder model for analysis of induced voltages and currents in sheath and armour

In order to measure current and voltage magnitudes at different positions along the cable, meters are placed between the cable segments as well as on each cable end. Measurements are conducted for both the positive and the negative phase. The full layout of the small PSCAD model can be seen in figure A.15 in the appendix.

### 5.3.4 Transient simulation results - Off/on

In this case the feeder operates under unfaulted condition. The system is energized from the turbines which are operating at full power. The energization is completed at 0.2 seconds, when the system reaches nominal voltage. At 0.3 seconds the turbines are turned off with a step input from nominal to zero power output and at 0.6 seconds an opposite step back to nominal power is set. Subsequently the resulting currents and voltages in the cable section of interest are presented.

#### Both ends grounded - each cable has sheath and armour grounded together

Figure 5.6 shows the conductor current in the positive and negative phase. Figure 5.7 shows the current flow in sheath and armour of both phases.

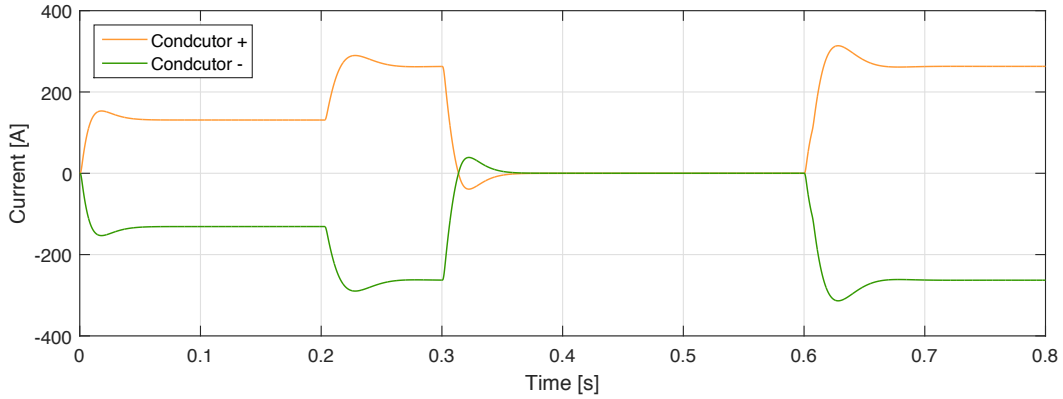


**Figure 5.6:** Conductor currents with grounding on both ends

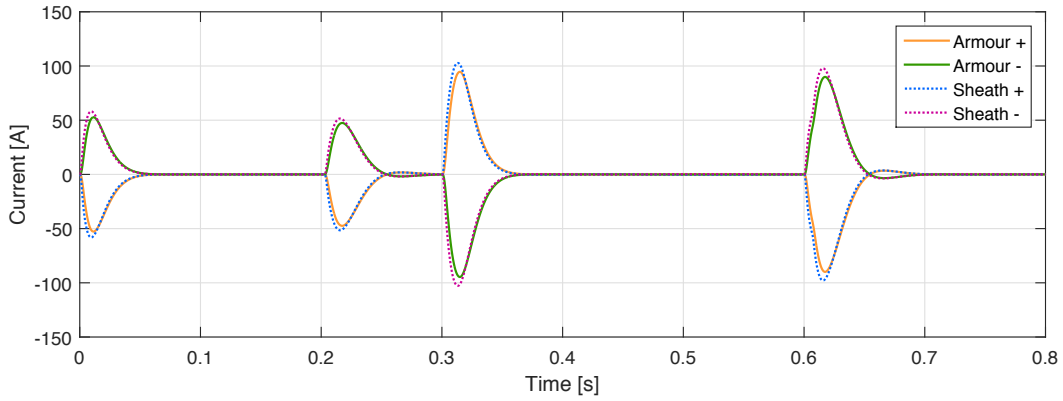


**Figure 5.7:** Induced currents in sheath and armour with grounding on both ends

It can be seen that a change in the conductor current flow induces a current in the sheath and armour. Its magnitude is highest when a step change in turbine output is applied, due to the steep slope of the conductor current. However, the shut down of the turbine leads to a slightly higher peak than the start up. This can be explained by the unidirectional power flow of the substation converter, if the turbines are shut down, their current flow declines to zero and the output capacitors discharge to nominal voltage and this excess energy is then exported to the substation. On the other hand, when the turbines resume normal operation, their output capacitors have to recharge to their previous voltage level above nominal voltage. The energy needed to do so has to be provided from the turbine, as the substation converter prohibits power import from the HVDC link, and consequently the current in the cable conductor changes with a smaller slope compared to the shut down, hence inducing a smaller current.

The voltages of the conductor, sheath and armour are depicted in figures 5.8, 5.9 and 5.10 respectively. In the sheath and armour figures, the voltages are shown for all seven measurement points along the

cable section.

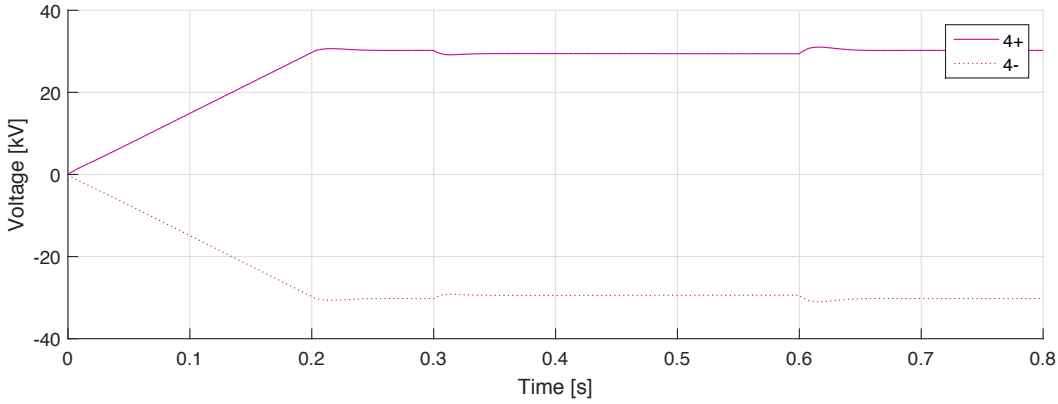


**Figure 5.8:** Conductor Voltage with grounding on both ends

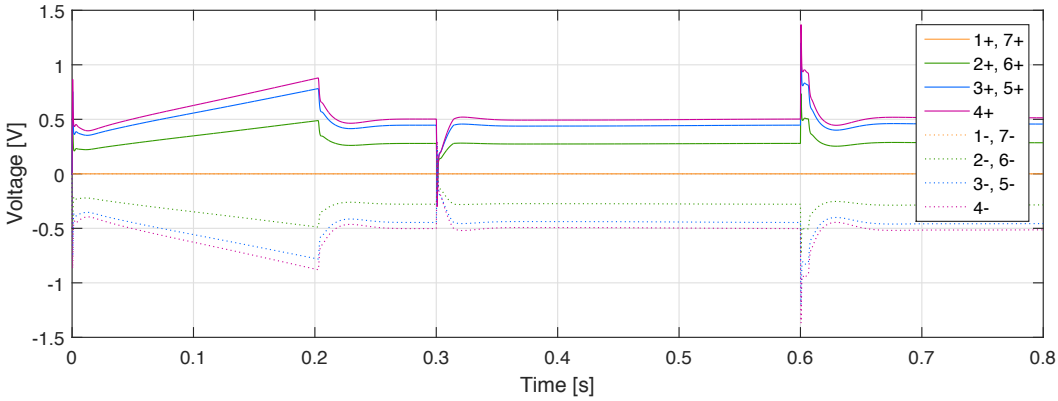


**Figure 5.9:** Sheath Voltage with grounding on both ends

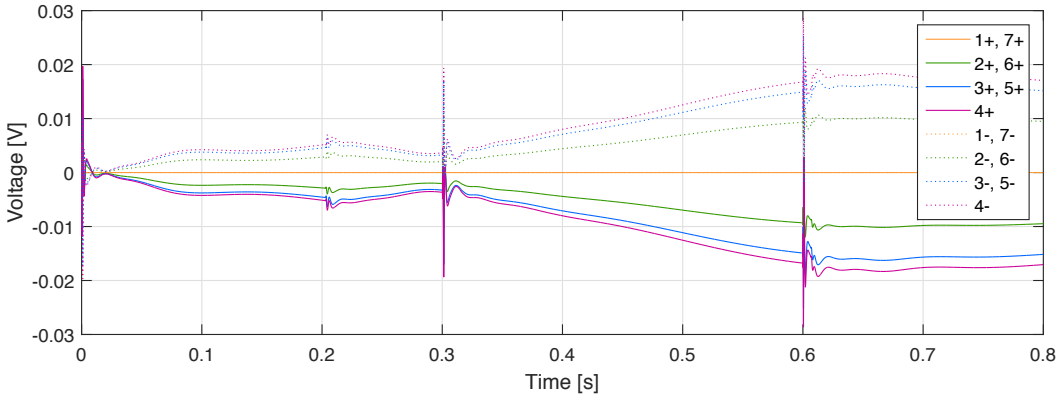


**Figure 5.10:** Armour Voltage with grounding on both ends

The conductor voltage drops about 1 kV and increases 2 kV as a result of the current decrease at 0.3 s and increases again at 0.6 s when the turbines are turned on. The sheath voltage at points one and seven are zero since the ends are grounded. The highest voltage measured is in the middle of the cable and it is seen that the nominal voltage level is 0.5 V and reaches a peak of 1.5 V when the turbines turn on at 0.6 s. The voltage induced in the armour reached a maximum of 0.03 V. It is also seen that the it has the opposite potential of the sheath since the induced current will have an opposite flow.

### Conclusion - Start stop, both ends grounded

It was clearly seen that the highest voltage magnitudes were at the middle of the cable when both ends are grounded, but with a negligible magnitude. The sheath current is just over 100 A and the armour

10 A lower. It can be concluded that by way of reducing the sheath and armour voltages, grounding both ends is recommendable.

### Armour and sheath grounded at one end

In this section the simulations will be done with the sheath and armour grounded at point 7 only.

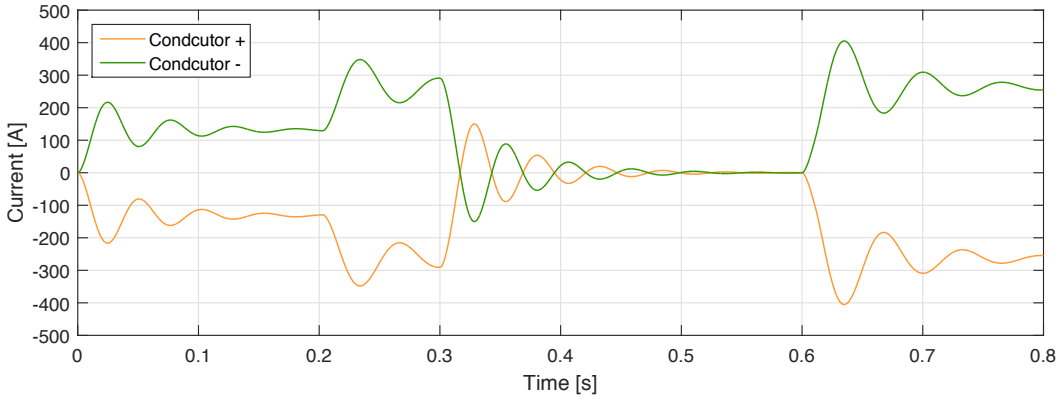


**Figure 5.11:** Conductor currents with grounding on one end (point 7)

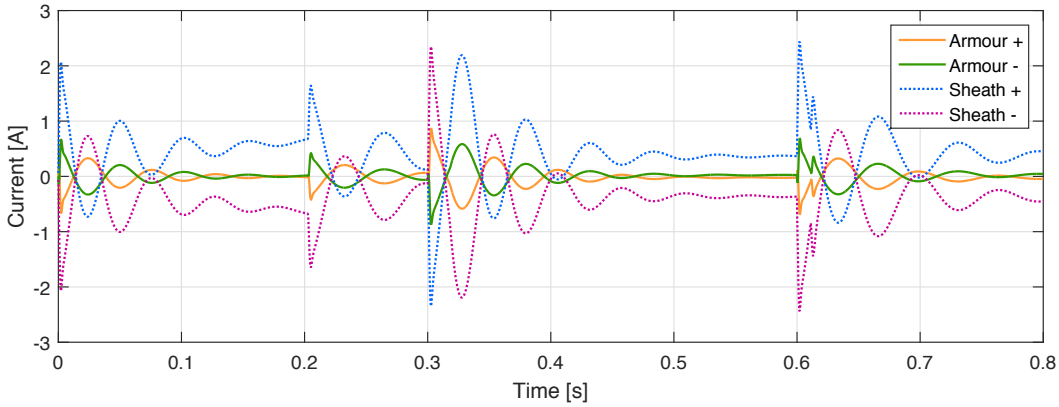


**Figure 5.12:** Induced currents in sheath and armour with grounding on one end (point 7)

Figure 5.11 shows that the current oscillates considerably which could indicate that there is some induction from the sheath to the conductor. Analysing the sheath voltage should reveal if this is indeed the case. The current exceeds 400 A during re-energisation. The currents in the sheath and armour seen in figure 5.12 follow the same oscillatory pattern as the conductor current and reach maximum magnitudes of 2.5 A and 0.9 A for the sheath and armour respectively.

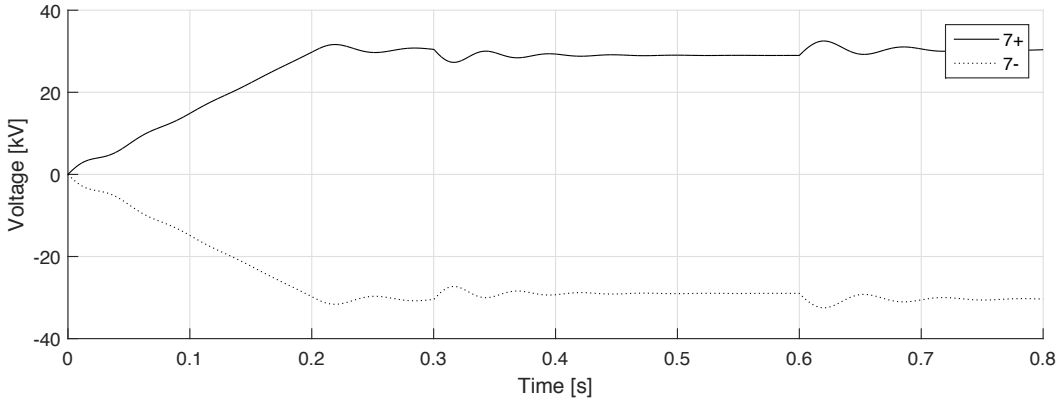


**Figure 5.13:** Conductor Voltage with grounding on one end (point 7)

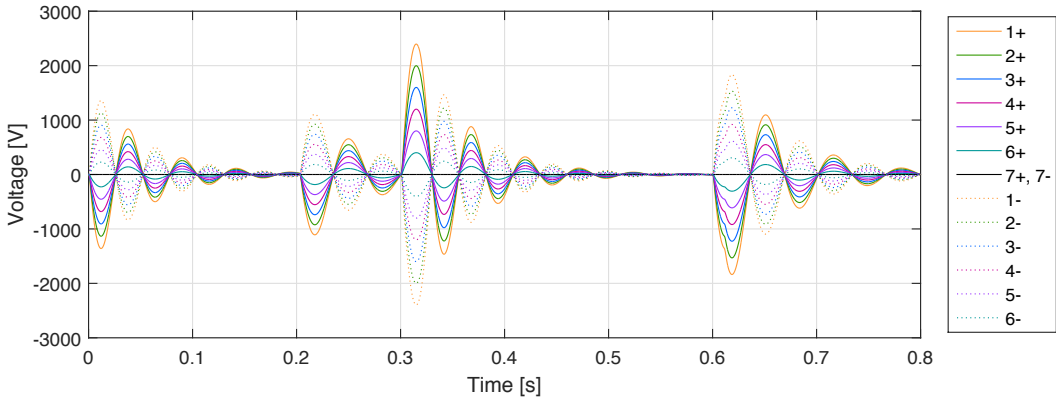


**Figure 5.14:** Sheath Voltage with grounding on one end (point 7)

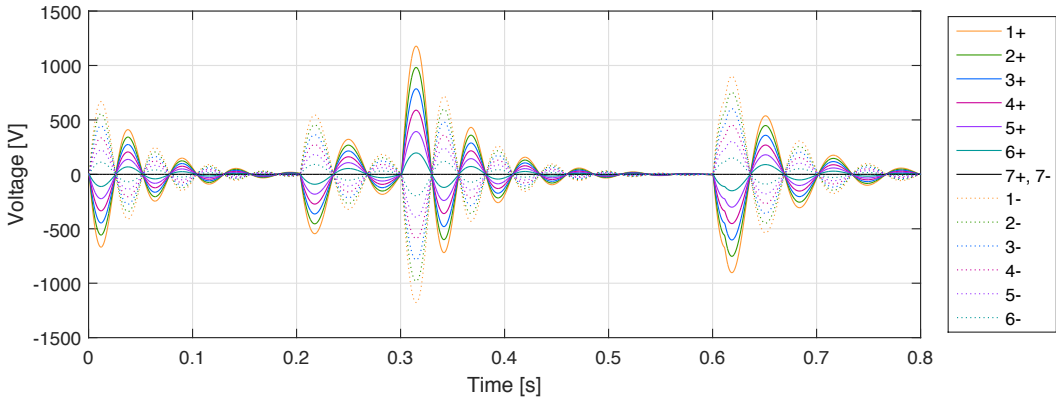


**Figure 5.15:** Armour Voltage with grounding on one end (point 7)

The conductor voltage in figure 5.13 is also seen to oscillate more than compared to the both ends grounded case. Figure 5.14 shows that the voltage reaches almost 2500 V at point 1 with a steep slope, which when considering equation 3.10 in section 3.2, it will induce voltages both in the conductor and armour. The voltage in the armour seen in figure 5.15 follows the trend of the sheath with an amplitude reaching half that of the sheath current.

### Conclusion - Start stop, one ends grounded

Since the voltage induced in the sheath and armour reached 2500 V and 1250 V, it must be considered if the insulation between them will withstand the voltages generated in the full model. This will have to be carefully considered when finalising the cable design.

### No Grounding

In this case the sheath and the armour of the long cable are not grounded. It has a simulation time of 10 s, to ensure that steady state was reached before shutting the turbines off and on, as it was seen to have a prolonged oscillatory behaviour.

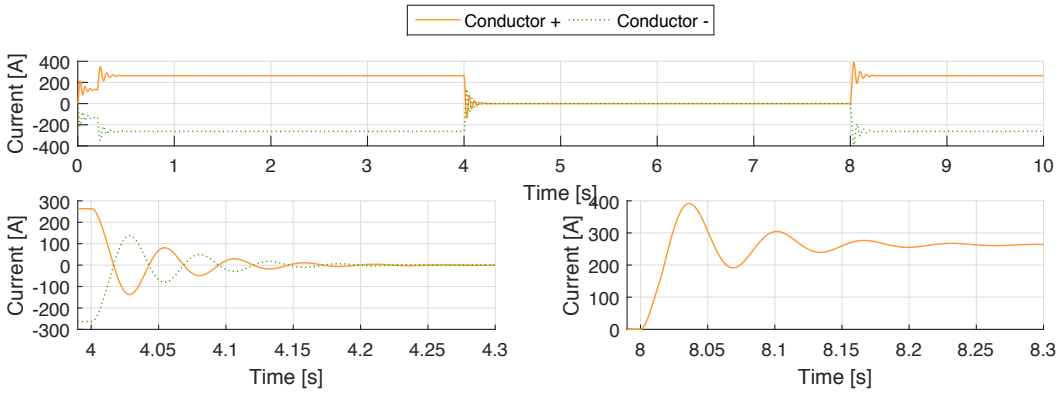


**Figure 5.16:** Conductor currents without grounding

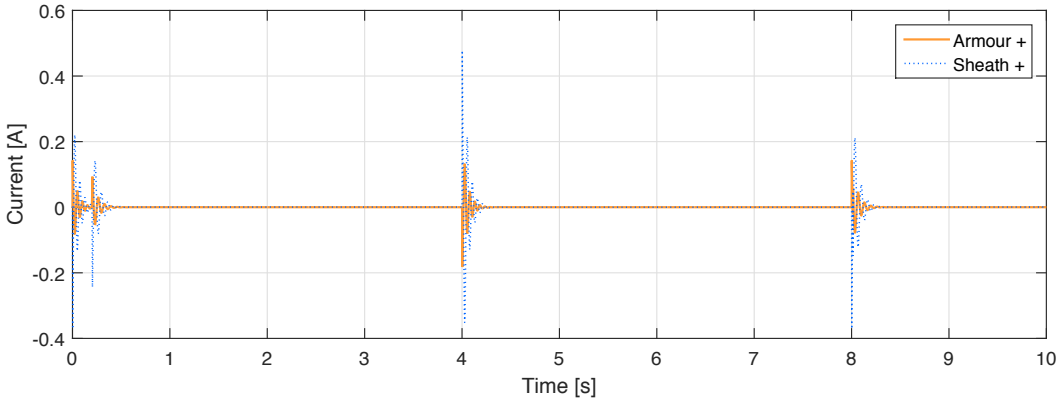


**Figure 5.17:** Induced currents in sheath and armour without grounding

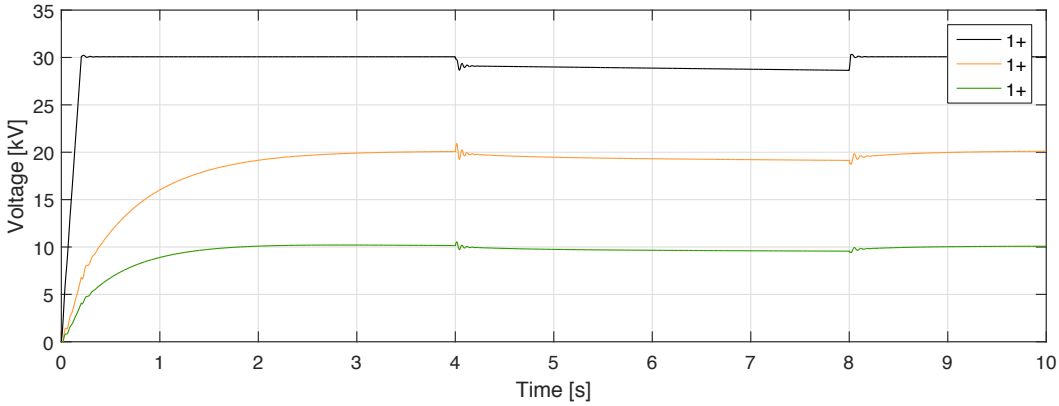


**Figure 5.18:** Conductor, sheath and armour voltage without grounding

In figure 5.16, there are two sub-plots which show a close-up of the switching events at 4 and 8 s respectively. It can be seen that the current takes 0.3 s to settle and reaches almost 400 A when the turbines turn on. This increase in current will be due to the effects of the sheath to conductor as in the one end grounded case. The induced currents in the sheath and armour reach a maximum of 0.5 A and 0.15 A as seen in figure 5.17. Since the current loop is not closed, there will be only be current in the sheath and armour relative to the parallel capacitances. Figure 5.18 shows the voltages of the positive phase of the conductor, sheath and armour. The conductor voltage shown in black, has some

oscillations and continues to decrease after the turbines are turned off. The sheath voltage shown in orange exceeds 20 kV at the time the turbines are shut off, and then continues to decrease for four seconds until the turbines are turned on again. The armour voltage in green, has the same trend as the sheath voltage but with a peak of 11 kV.

#### Conclusion - Start stop, without grounding

It was seen that sheath voltages reached over 20 kV which is very high when considering the comparatively small size sheath and armour insulation. Based on this case it can be concluded that grounding of the sheath and armour is required to some extent.

### 5.3.5 Maximum cable stresses - Off/on

Having analysed the transient behaviour of the cable model, the next step is the find the maximum stresses along the cable, to see which points will require measurements in the complete model. This is done by finding the maximum absolute value of each measurement point along the cable and plotting them in order to see how the voltages and currents propagate through the cable.

#### Turbine start and stop - Both ends grounded

The first results to analyse are from the start and stop case, as explained in section 5.3.4.

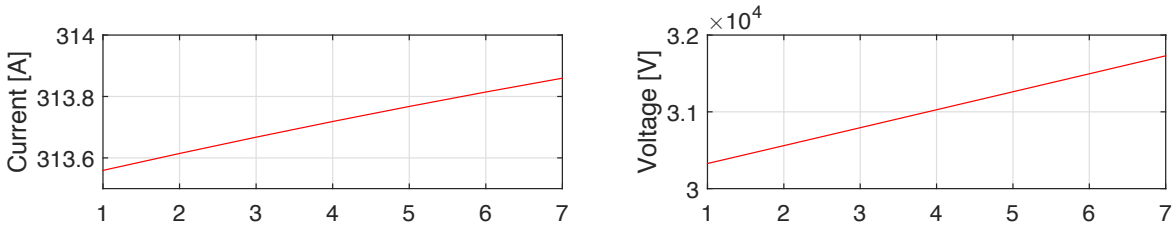


**Figure 5.19:** Maximum conductor stresses measured along the cable

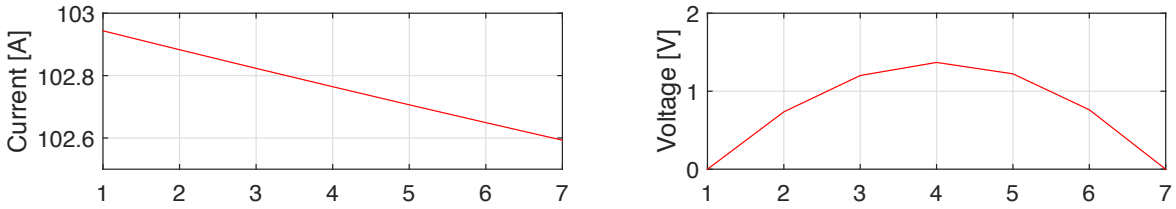


**Figure 5.20:** Maximum sheath stresses measured along the cable

From figure 5.19 it is seen that both the current and voltage are higher at point 7, the point farthest away from the substation, which is to be expected since the power is exported and current flows towards the lowest voltage potential. The current drop along the cable is due to the parallel capacitances between the conductor and sheath. The sheath seen in figure 5.20 has current reaching 103 A at point 1, and decreases 0.4 A at point 7. This reduction will be due to the parallel capacitances between the sheath and the armour and because it is induced by the conductor, which has an opposite current flow direction compared to the conductor. Since the sheath is grounded at both ends, the voltage does not reach more than 1.5 V in the middle of the cable.

### Turbine start and stop - One end grounded

In this case the sheath and armour are grounded at point seven only.

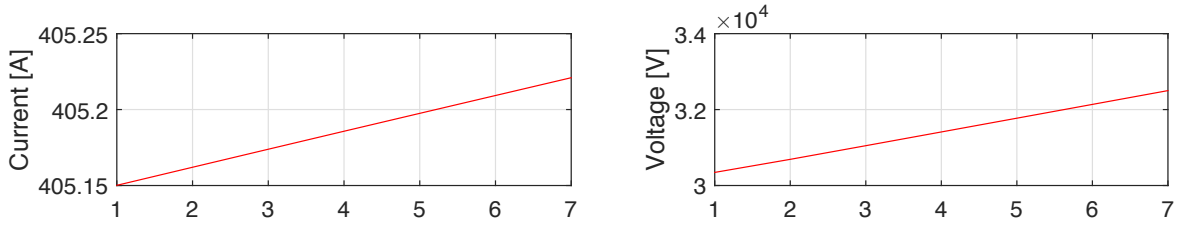


**Figure 5.21:** Maximum conductor stresses measured along the cable

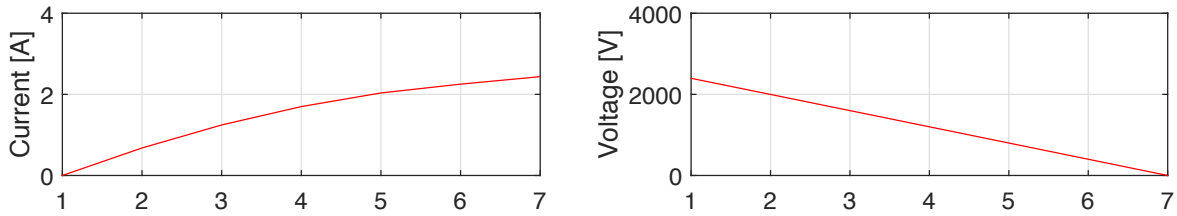


**Figure 5.22:** Maximum sheath stresses measured along the cable

As with the both ends grounded case, it is seen in figure 5.21 that both the highest current and voltage potential are at point 7, due to the power being exported. The sheath reaches just over 2 A at point 7 and 2500 V at point 1 as seen in figure 5.22. Since point 7 is grounded the voltage potential will be zero and the current will flow towards it.

### Turbine start and stop - No grounding

In the final start/stop case the armour and sheath will be ungrounded.

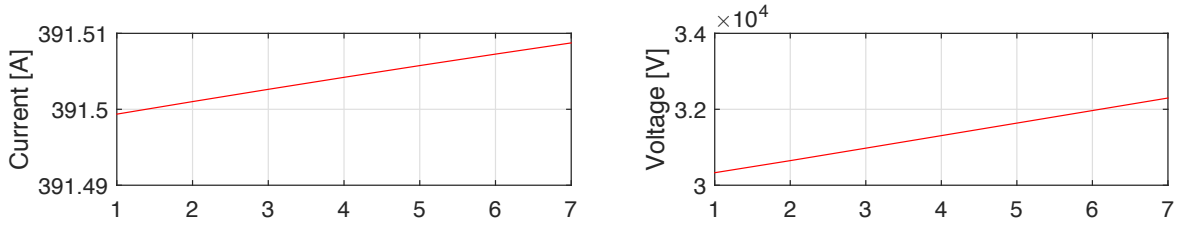


**Figure 5.23:** Maximum conductor stresses measured along the cable

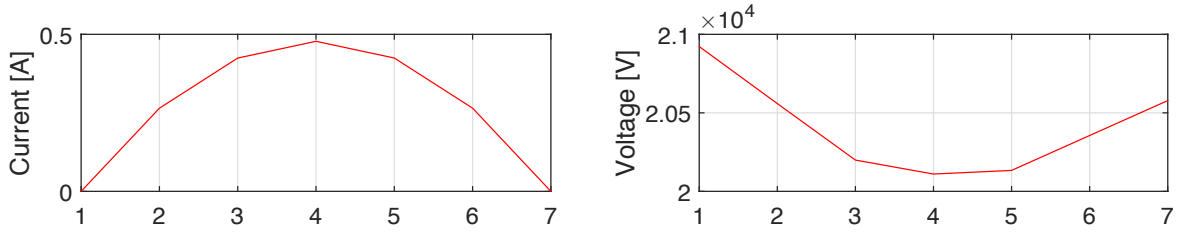


**Figure 5.24:** Maximum sheath stresses measured along the cable

Figure 5.23 shows the same trends as the other cases, but with a slightly lower currents and voltages compared to the one end grounded case. The maximum sheath currents and voltages measured in figure 5.24 are 0.5 A and just below 21 kV. Since there is no grounding the currents will be highest in the middle of the cable due to the parallel capacitances. The voltage is higher at point 1 compared to point 7, but is lowest in the middle of the cable.

### Conclusion - Turbine start and stop

It was seen when the turbines were turned off and on during the different grounding strategies, that if both cable ends are grounded, the induced voltages will be negligible but the currents will reach their highest. If there is no grounding the sheath voltages exceed 20 kV and when considering how thin the insulating layer between the sheath and armour are, it is doubtful that it could withstand such stresses. The last case is when only one end is grounded and it was seen that the voltages reached over 2 kV and just over 2 A. Another important factor to consider is the conductor current. When sheath and armour are not grounded, or just on one end, the conductor currents are considerably higher. This is due to the fact that if the sheath and armour are grounded, there will a proportionally larger current induced in them and, according to Lenz's law, the current will be induced in the opposite direction and its magnetic flux will try to oppose the change in flux from the conductor and will as such have a dampening effect. It can be concluded that in order to limit the voltage in the sheath and armour, they both need to be grounded. It will also be important to consider how much current the sheath and armour can handle if they are grounded on both ends.

### 5.3.6 Maximum cable stresses - Short circuit

In this section the results of the short circuit simulations will be presented. The cases to study will be as follows:

- Balanced fault at turbine A
- Balanced fault at turbine B
- Unbalanced fault at turbine B - positive conductor to ground

In order to reduce the amount of cases to present, only the simulations with both ends grounded will be presented here, as it is clear that the sheath and armour voltages of the other grounding strategies exceed the design criteria.

The figures which will be presented and discussed have been chosen based on worst cases for the both ends grounded scenario.

#### Balanced fault - Turbine A and B

The short circuit cases presented here are simulated at turbine A and B with both ends grounded respectively, to compare the cases more easily they have been compiled in the same figures, where turbine A is in blue and turbine B is in red.

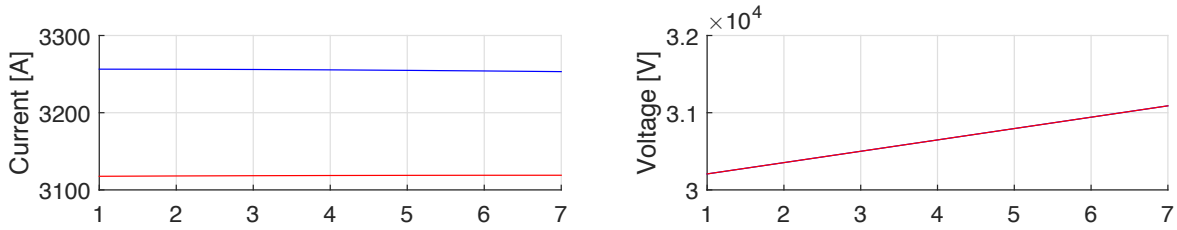


**Figure 5.25:** Maximum conductor stresses measured along the cable

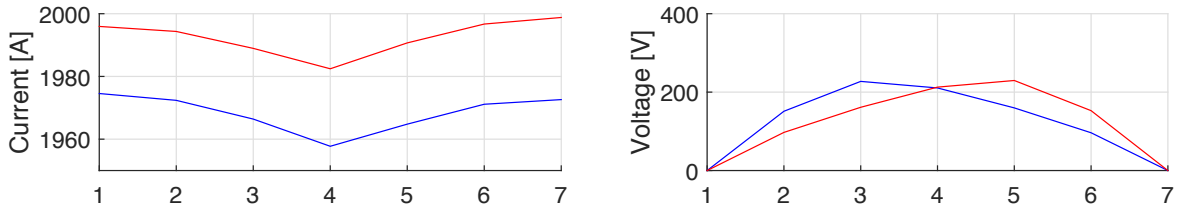


**Figure 5.26:** Maximum sheath stresses measured along the cable

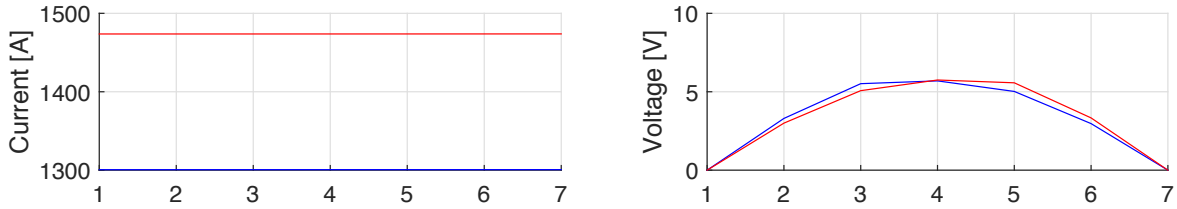


**Figure 5.27:** Maximum armour stresses measured along the cable

In figure 5.25 it is seen that the current levels are higher when the short circuit is at turbine A, which can be explained by the inductors. When the short circuit is at turbine A, the inductors from turbine B and C contribute to the fault, but when the fault is at turbine B, only the inductor at turbine A contributes. The voltages are seen to be the same since they will be highest during the energisation process and collapse after the phase to phase fault. The current in the sheath seen in figure 5.26 is highest at point seven and lowest in point four when the fault is at turbine B, and opposite when the

fault is at turbine A. Having examined the individual data, it was seen that when the highest currents were measured, there were some harmonics in the sheath which skewed the measurements. The red curve is higher due to the total slope of the conductor current being higher when the fault is at turbine B, since the current has to change direction. The maximum current measured is almost 2 kA for a balanced fault. The sheath voltages are seen to be highest in points 3 and 5 with peaks of about 220 V. Since both ends are grounded the expected voltage peak would be in the middle of the cable, but due to the oscillations of the fault the peaks are shifted from centre. The armour currents and voltages in figure 5.27 are similar to the sheath, but with the oscillations considerably lower which is seen by an even line for the current and the voltage maximums being closer to the cables centre.

**Balanced fault conclusion**

During a balanced fault it was seen that the short circuit currents for the conductor, sheath and armour reach 3250 A, 2000 A and 1580 A respectively. These are expected to be the highest fault currents in any of the cases and the balanced fault case will be used in the complete model to ensure that the cable can withstand the currents.

### Unbalanced faults - Turbine B

In this section the unbalanced faults will be presented. The short circuit events are simulated as positive conductor to ground at turbine B, since this location was found to have the highest stresses. The positive conductor is shown in red and the negative in blue.

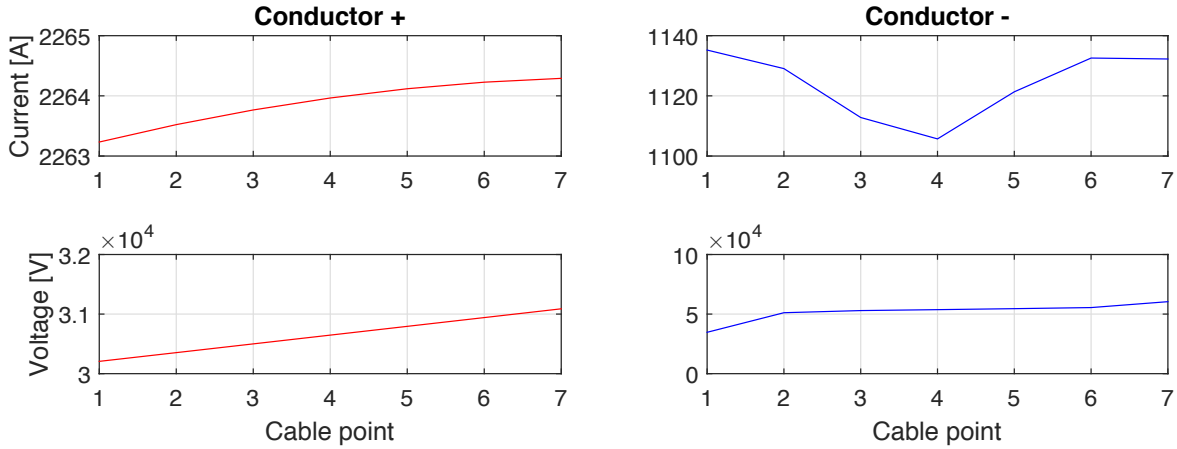


**Figure 5.28:** Maximum conductor stresses measured along the cable

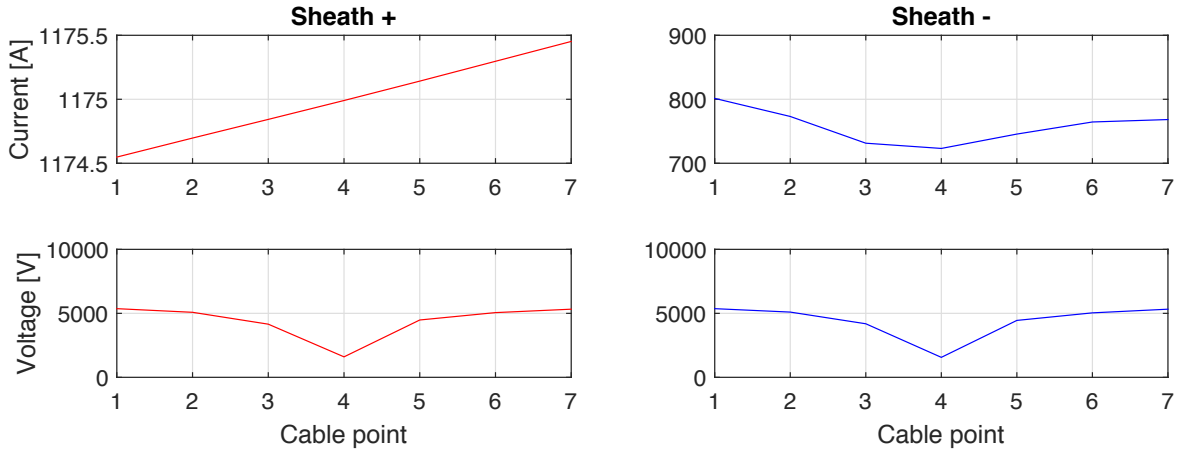


**Figure 5.29:** Maximum sheath stresses measured along the cable

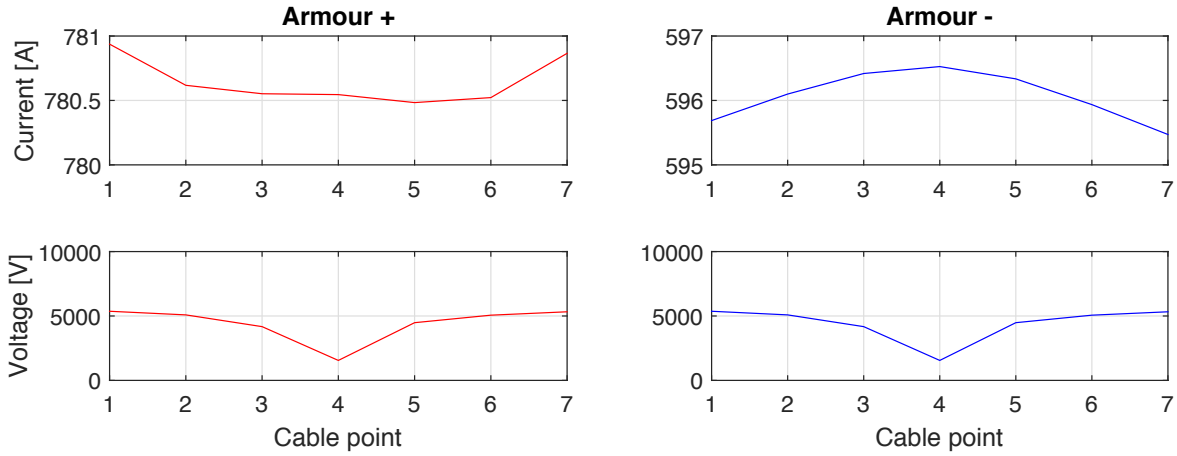


**Figure 5.30:** Maximum armour stresses measured along the cable

It is seen in figure 5.28 that the maximum current measured in the positive conductor is 2264 A and 1135 A for the negative conductor. Comparing to the balanced faults the currents are considerably lower, but the voltage in the unfaulted conductor reaches 60 kV which is the highest fault voltage

in any case and will as such be used as the design criteria for the conductor insulation. The sheath around the faulted conductor in figure 5.29, has a current exceeding 1175 A and a voltage of over 5 kV. Comparing to the armour voltage in figure 5.30 it is seen that the maximum voltages at the cable ends are the same, with a 50 V difference in the middle of the cable. Since the sheath and armour are grounded together at both ends, they will have the same potential there. The maximum armour current in figure 5.30 reaches over 780 A in the faulted cable and 596 A in the unfaulted cable and has the same voltage potential as the sheath.

#### Unbalanced fault conclusion

It was seen that the single phase to ground faults cause the highest voltage stresses throughout the cable. Exceeding 60 kV for the conductor and 5 kV for the sheath and armour. It is therefore clear that the unbalanced faults will be the benchmark for the insulation in the cable.

### 5.3.7 Conclusion - Analysis of cable stresses

During the analysis of the sheath and armour stresses, it can be concluded that when implementing measurements in the complete model, the sheath and armour voltages and currents will need to be measured at the ends of the cable. There is no need for measurements in the middle of the cable since the highest voltages stresses, measured in the unbalanced fault case, were at the cable ends. The highest current stresses were measured during the balanced fault case, were also at the cable ends.

In the start/stop case the different grounding strategies were explored and it was seen that the voltages increased greatly when not grounding or only grounding on one end of the cable. Therefore it can be concluded that in the complete model the cables should be grounded on both ends of the cables.

## 5.4 Fault Analysis

The simulation model described in section 5.2 will be used and four cases will be studied: Turbines off and on, balanced fault, unbalanced fault and conductor to sheath fault. In the fault cases the faults will be between the turbine and cable at turbines 1 & 4 in radial 1. All of the cases will be conducted for three substation voltage levels, 0.9 pu, 1 pu and 1.1 pu, all in all 19 simulations will be conducted. The off/on case is only conducted for 1 pu to see how the modelled wind farm operates in non-faulted conditions so comparisons can be made with the fault cases.

### 5.4.1 Aim

First the results of the simulations will be analysed to verify the model itself, and to look at transients and behaviour in general to see if the results make sense. The second aim of these simulations is to find the maximum cable stresses to validate the cable design, and if needed, modify it accordingly. When the cable stresses have been found, it will be determined if any protection equipment will be needed.

### 5.4.2 Limitations

- The cases presented here will only be of the 1 pu case in order to reduce the number of figures presented. The waveforms of the different substation voltage levels will be representative, amplitudes will differ.
- Faults will not be simulated at the substation, since a single converter substation is used, no protection scheme can be implemented to resolve such faults.
- No harmonic studies will be made since the converters are not in the scope of this thesis.

Tables with the maximum stresses, including those not presented here, will be present at the end of this chapter.

### 5.4.3 Model

The complete PSCAD model with illustrations and explanations of all relevant sections can be seen in appendix A.7, where also the lumping method is described. The full offshore wind farm model has measurements at the following locations:

- **Radial 1** - Current and voltage is measured at each turbine cable, sheath and armour measurements are made at the beginning of the first cable and the end of the last cable.
- **Radial 2** - Current and voltage is measured at each turbine cable
- **Radial 8** - Currents are measured at each filter capacitor, the inductor and the beginning of each cable
- **Substation** - Currents are measured before and after the filter capacitors, voltages are measured at each pole after the filter capacitors
- **Overall** - Outgoing currents are measured at each pole for every radial, voltages are measured at the end of each radial

### 5.4.4 Turbines off and on

In this case all of the turbines in the offshore wind farm will be turned off at 0.3 s and on again at 0.5 s. Figures with currents and voltages from several locations will be presented and discussed below.

#### Substation

In this section the figures from the substation will be presented. Starting from the top, 1: Currents measured at the substation before and after the filter capacitors. 2: Currents measured at the radials. 3: Voltages measured at the ends of the radials. 4: Voltage measured at the substation after the filter capacitors. - Solid lines are positive conductors and dotted lines are negative.

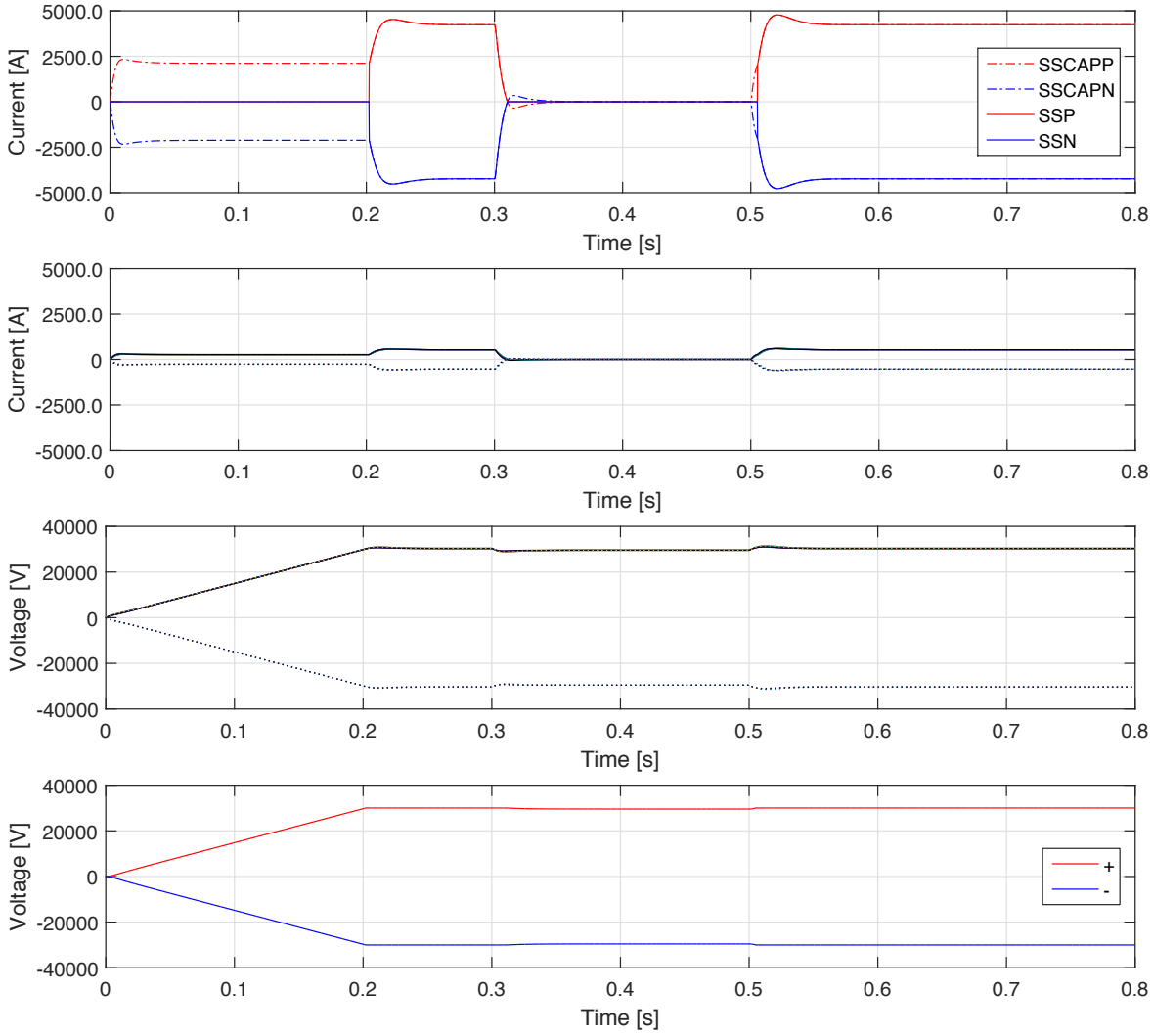


**Figure 5.31:** Currents and voltages measured at the substation

In figure 5.31, SSCAPP is the capacitor connected to the positive phase, SSCAPN is the capacitor connected to the negative phase, SSP and SSN are currents measured at the positive and negative cables at the substation voltage source. It is seen that while the capacitors charge there is no power exported, until 0.2 s where steady state is reached after a brief overshoot. At 0.3 s the turbines are turned off and there is small capacitor discharge when the voltage drops, which is seen to charge again when the turbines turn on at 0.5 s. The second figure shows the currents entering the substation from the radials, which closely follows the trends of the substation currents. The two following figures show the voltages at the end of the radials and the substation voltage after the filter capacitors respectively.

### Radial 1

Here the measurements from radial 1 will be presented. 1: Currents measured in the conductor. 2: Voltage measured over the conductor. 3: Currents measured in the sheath and armour. 4: Voltages measured over the sheath and armour.

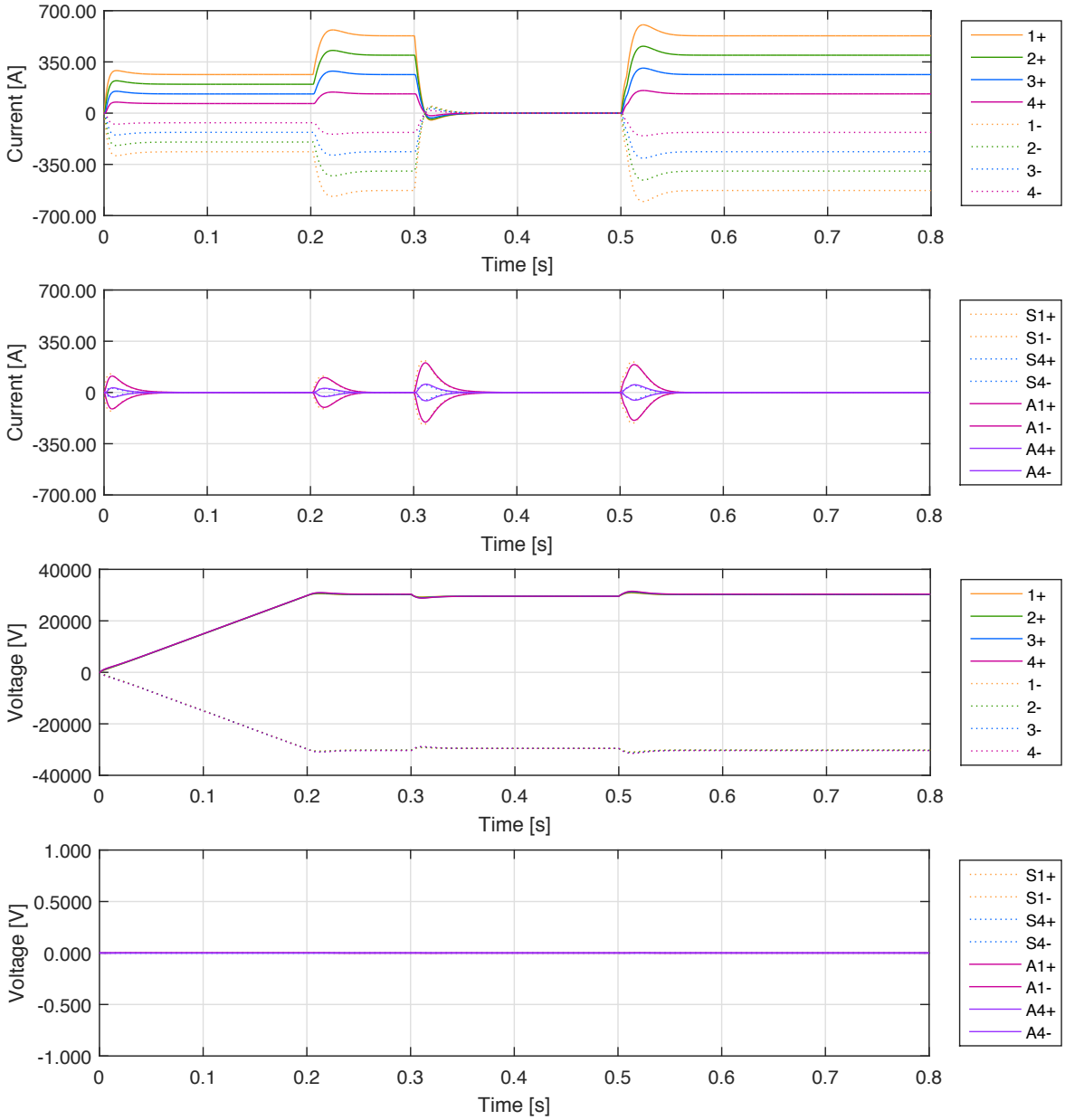


**Figure 5.32:** Currents and voltages measured at radial 1

The conductor currents in figure 5.32 are seen to be uniform and increase as each turbine feeds in to the cable. The sheath and armour currents show that the sheath current has a peak of 220 A when the turbines are turned off, with the armour current reaching 200 A at the same time. Since they are separate cables, the cable closest to the substation will have the higher currents since its conductor carries the most current. The conductor voltages follow the same trend as the substation voltages and the induced voltages in the sheath and armour are close to zero.

### Radial 2 & 8

Comparing the inductor and capacitor currents in radial 2 & 8 will reveal if the normal and lumped radials differ. The first two graphs presented are inductor and capacitors from radial 8 and 2 respectively. The last two figures are the currents entering the cables of the first turbine of the respective radials.

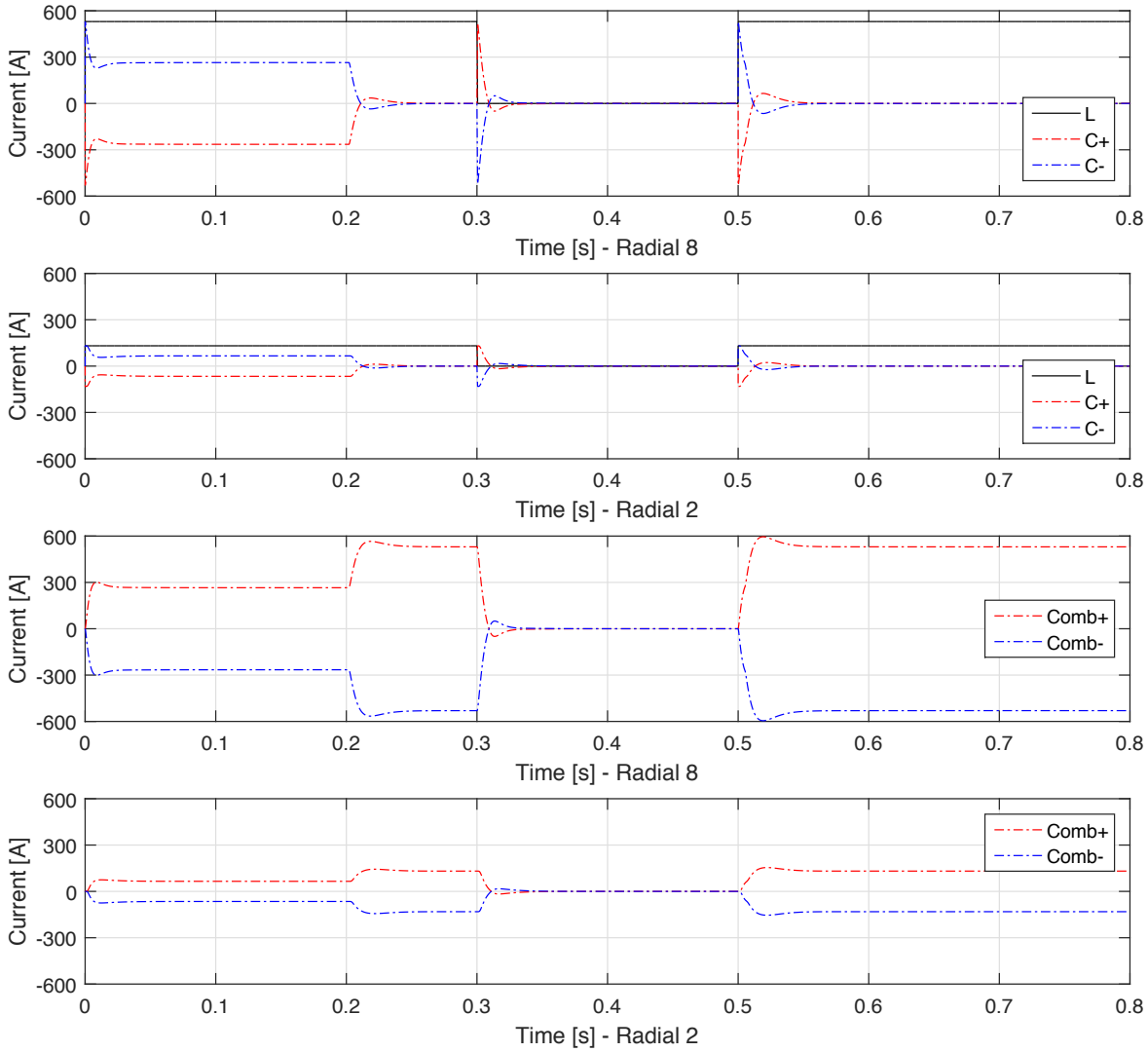


**Figure 5.33:** Currents and voltages measured at radial 1

Figure 5.33 is divided into two graphs, the top one shows the currents from the filter capacitors and the inductor, and the lower graph shows the combined current being fed in the cable. It is seen that the inductor current has the nominal current of the turbine and falls rapidly to zero due to its small size as soon as the turbine is shut off. Comparing the two top figures it is seen that the filter capacitors use half of the turbine current to charge, the other half being exported to the substation capacitors. The two lower figures show that the current from the turbines in the lumped and un-lumped radials have the same trends with different amplitudes. The maximum voltage and current values measured during the off/on simulations have been compiled in table 5.1.

| | **Off/on** | | |
|---|---|---|---|
| | **Conductor** | **Sheath** | **Armour** |
| V | 31493 | <1 | <1 |
| A | 603 | 221 | 203 |

**Table 5.1:** Maximum values measured at radial 1 when switching the turbines off and on again

### 5.4.5 Balanced fault

In this case there will be a balanced fault at the end of radial 1, between cable 1D and turbine 14 as seen in figure 3.3.

**Substation**

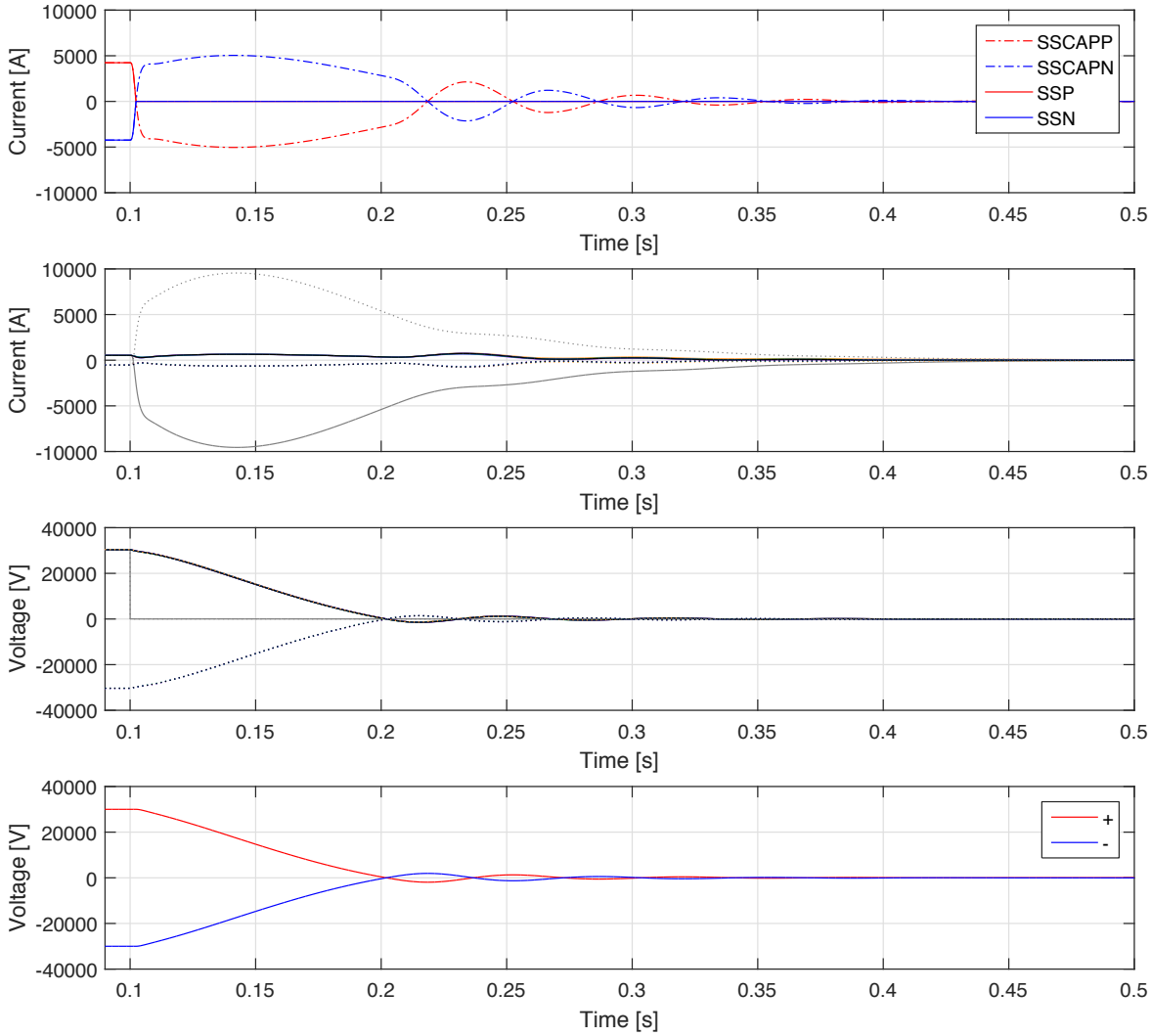


**Figure 5.34:** Currents and voltages measured at the substation

The substation capacitors in figure 5.34 are seen to discharge at the time of the fault and no more power is exported. After 0.22 s the capacitors charge again and the peak corresponds with the discharge of the radial capacitors seen in the graph below. The second graph shows that at 0.1 s the current flowing into radial 1 reaches almost 10 kA and when looking at the other radials, there is an increase in amplitude again which starts right after 0.22 s. Looking at voltage graphs in the substation and the end of the radials, it is seen that the voltage in the positive conductors becomes negative after 0.2 s, which may be part of the explanation. Looking closer at radial 8 and the specific component currents might yield the full answer.

**Radial 1**

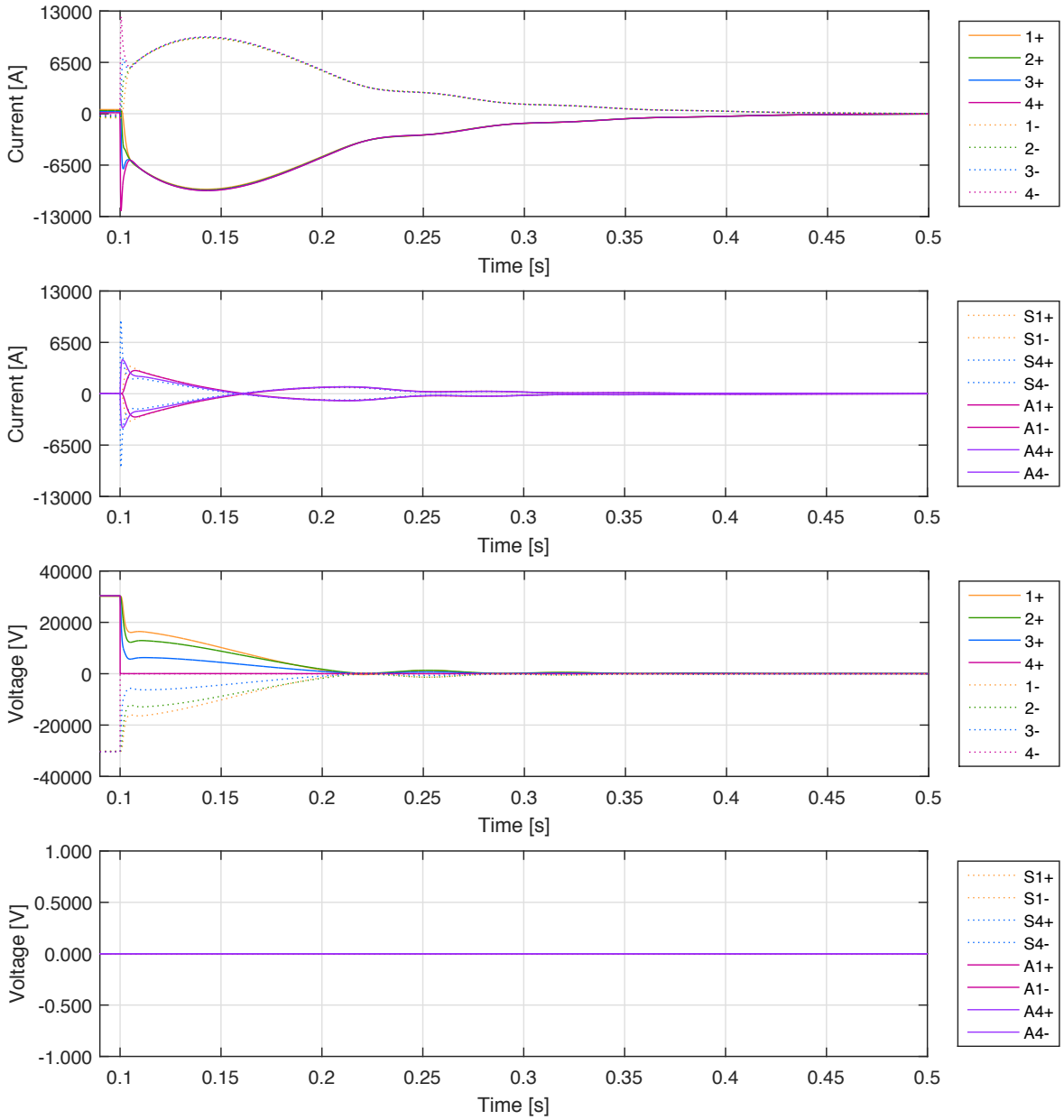


**Figure 5.35:** Currents and voltages measured at radial 1

The conductor currents, shown in the first graph in figure 5.35, is seen to have a large peak which is from the capacitors closest to the fault, in this case from the filter at turbine 1C. After the initial peak of 12300 A there is a second rise which reaches 10 kA and then decays. Currents induced in the sheath and armour are seen in the second graph, where it is seen that the sheath near the fault has a maximum of about 9300 A for a very short time, and the armour current reaches 4300 A at its peak. According to the simulations made in the small system, these should be the highest currents measured in any of the simulation cases. The conductor voltages in the third graph shows that the voltage starts to collapse at the time of fault and has a small increase at 0.25 s which correlates with the second capacitor discharge seen in figure 5.34.

**Radial 2 & 8**

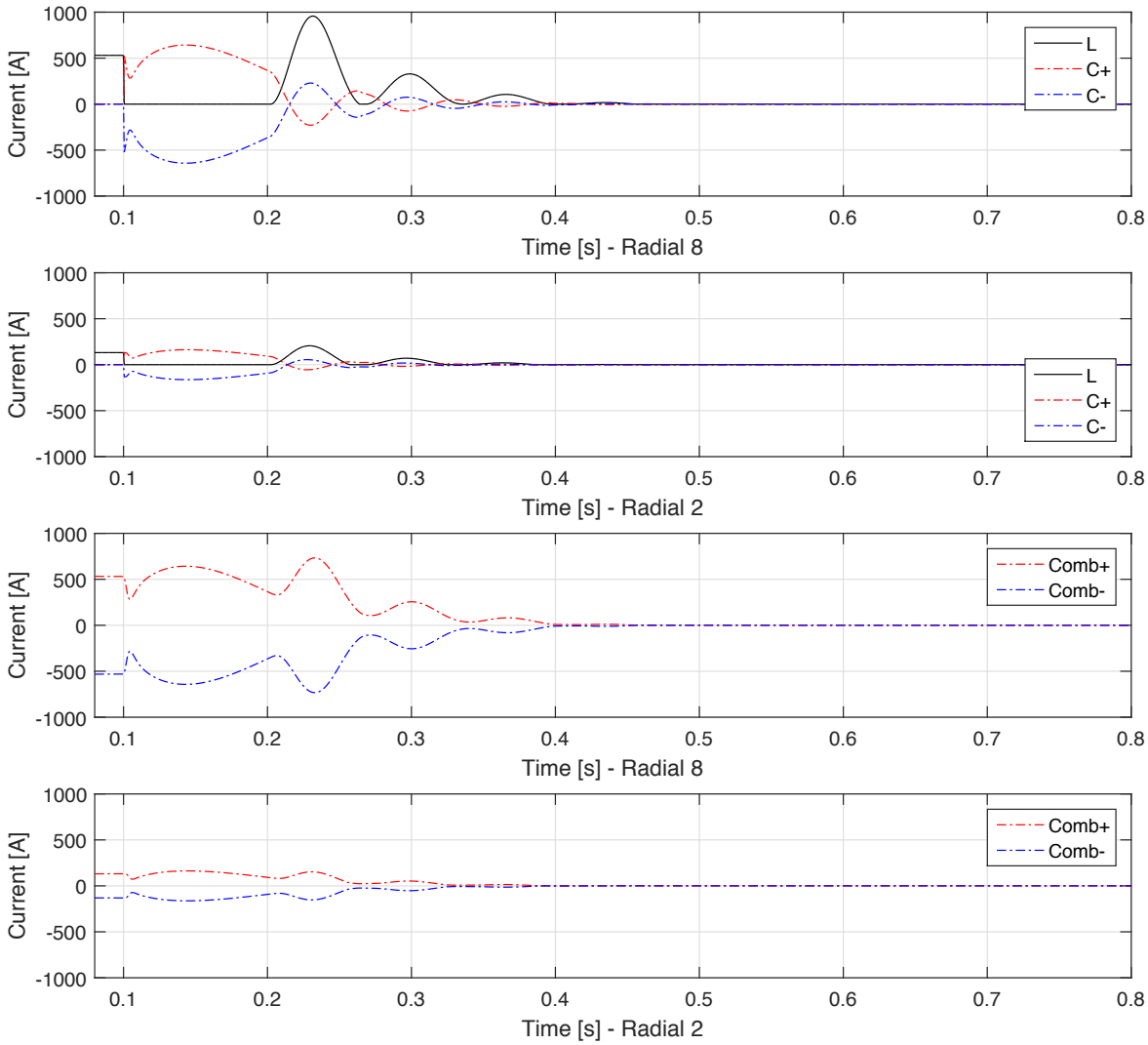


**Figure 5.36:** Comparison of currents measured at radials 2 & 8

Looking at the inductor current in figure 5.36 it is seen to go to zero as soon as the fault occurs, but rises again right after 0.2 s. Keeping in mind that in figure 5.34 the voltage was seen to change polarity which would reverse bias the turbine diodes and allow current to flow in the capacitors again, explaining the current peak seen at the substation in figure 5.34.

The maximum values for the balanced case can be seen in table 5.2. The sheath and armour voltages are close to zero.

| | **Balanced fault** | | |
|---|---|---|---|
| | **Conductor** | **Sheath** | **Armour** |
| V | 30969 | <1 | <1 |
| A | 12294 | 9341 | 4304 |

**Table 5.2:** Maximum values measured at radial 1 during a balanced fault

### 5.4.6 Unbalanced fault

In this case there is an unbalanced fault, positive conductor to ground, at the same location as in the balanced fault case, the end of radial 1.

#### Substation

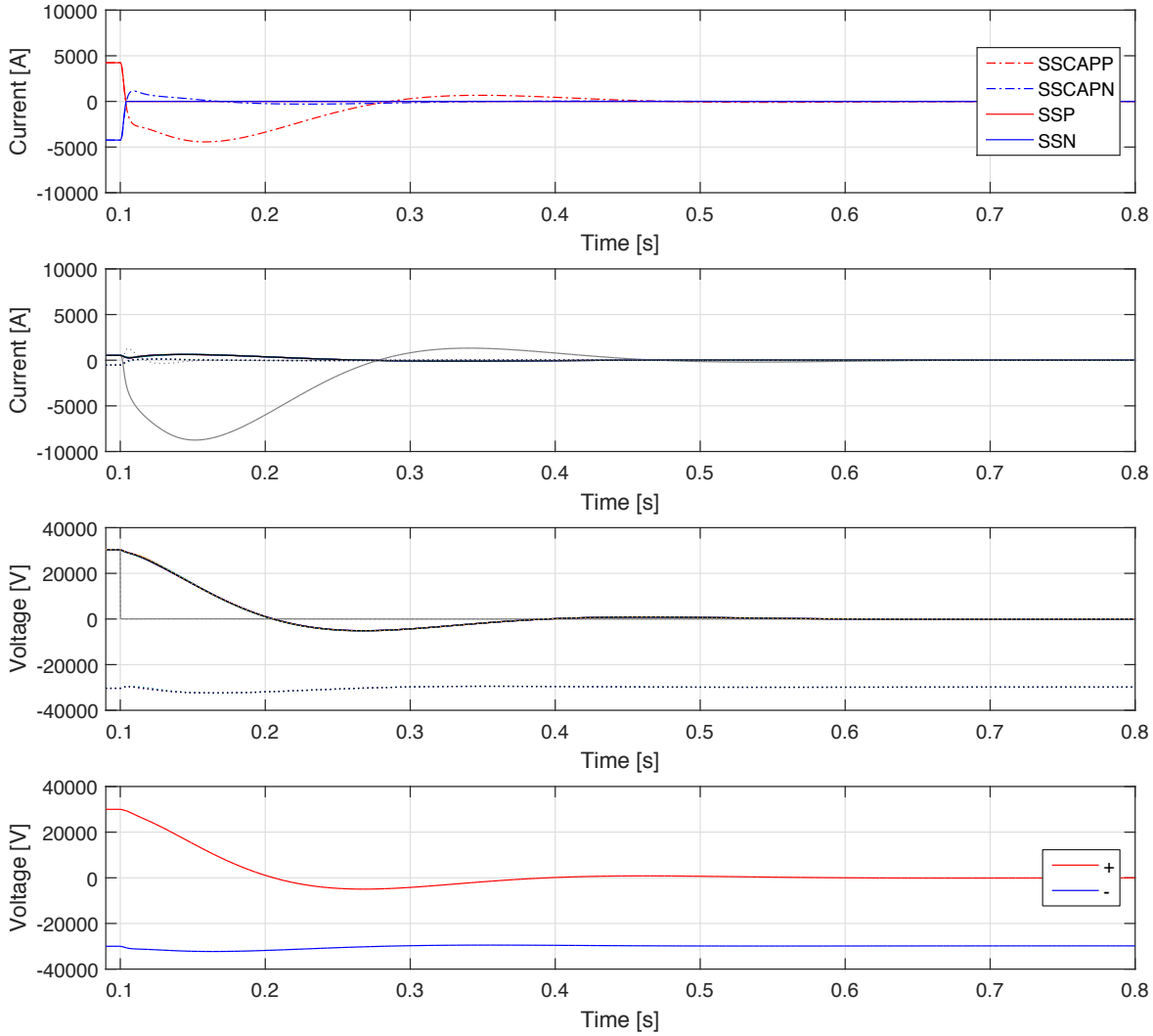


**Figure 5.37:** Currents and voltages measured at the substation

The substation currents in figure 5.37 show that the positive capacitor discharges until 0.28 s, where in the last graph the voltage slope in the positive conductor starts to rise again. The negative capacitor has a small discharge since the voltage in the negative conductor has a relatively stable progression. The radial currents in second graph, show that the positive cables current resembles the balanced case.

**Radial 1**

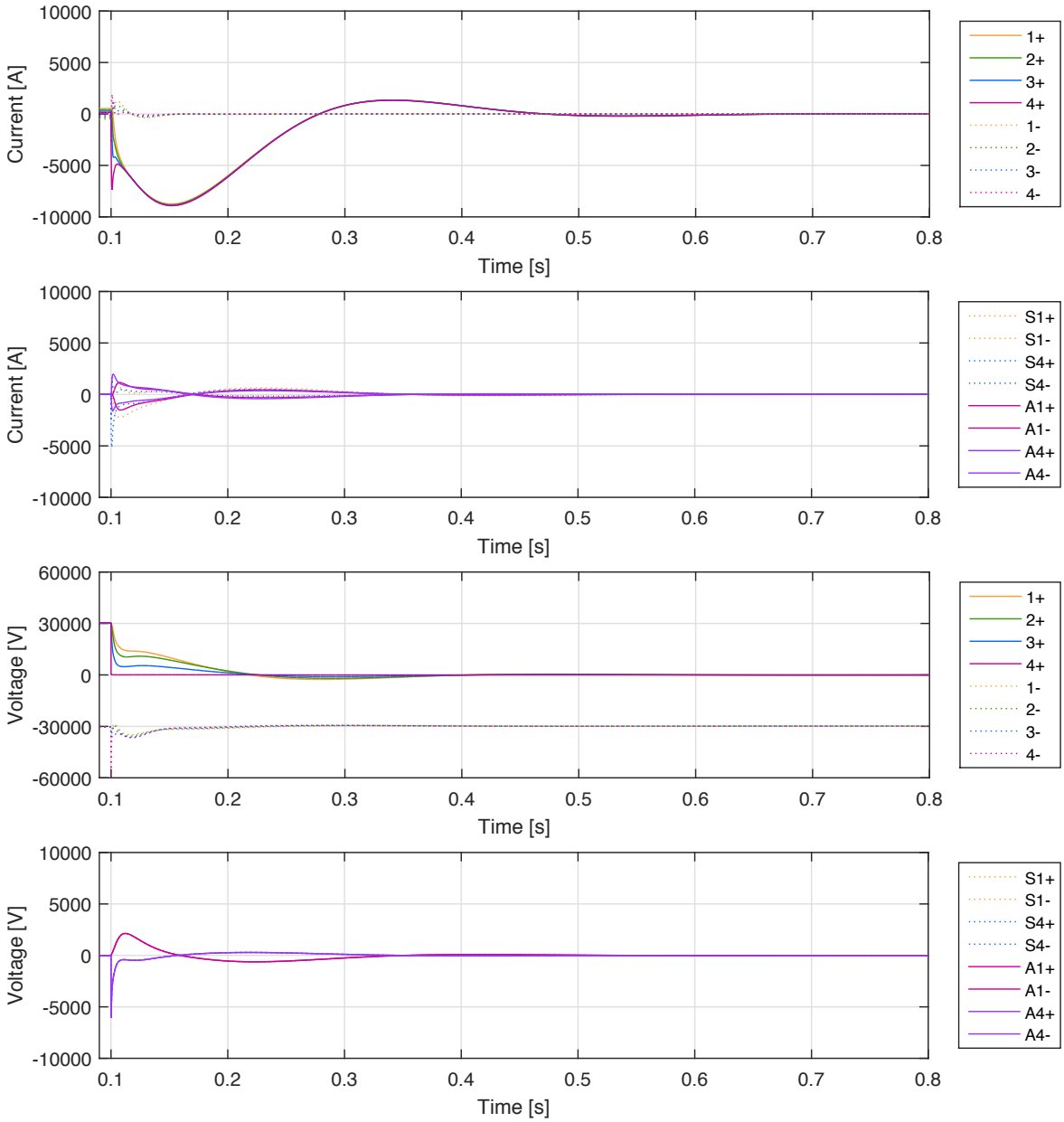


**Figure 5.38:** Currents and voltages measured at radial 1

At 0.1 s when the fault occurs, there is spike in cable section 5 which is closest to the fault, but the maximum current in figure 5.38 is at 0.15 s, which corresponds with the measured substation current. The negative cables have a maximum current of only 2 kA, compared to the almost 9 kA in the positive cables. The second graph shows that the sheath current reaches a maximum of 5.1 kA right at the time of the fault, and that the armour reaches 2 kA. The conductor voltage in the third graph shows that at the instance when the fault occurs, the positive conductor near the fault goes to 0 V and the negative conductor goes to -60 kV. This is the largest voltage deviation in any of the faults and will be used as the value which the cable will have to withstand. The sheath and armour voltage in the final graph shows that the measured voltages are the same and peak at 6 kV at the time of the fault for the positive conductor. This is the highest sheath and armour voltage and will as such be used as a maximum when checking the cables withstand levels.

**Radial 2 & 8**

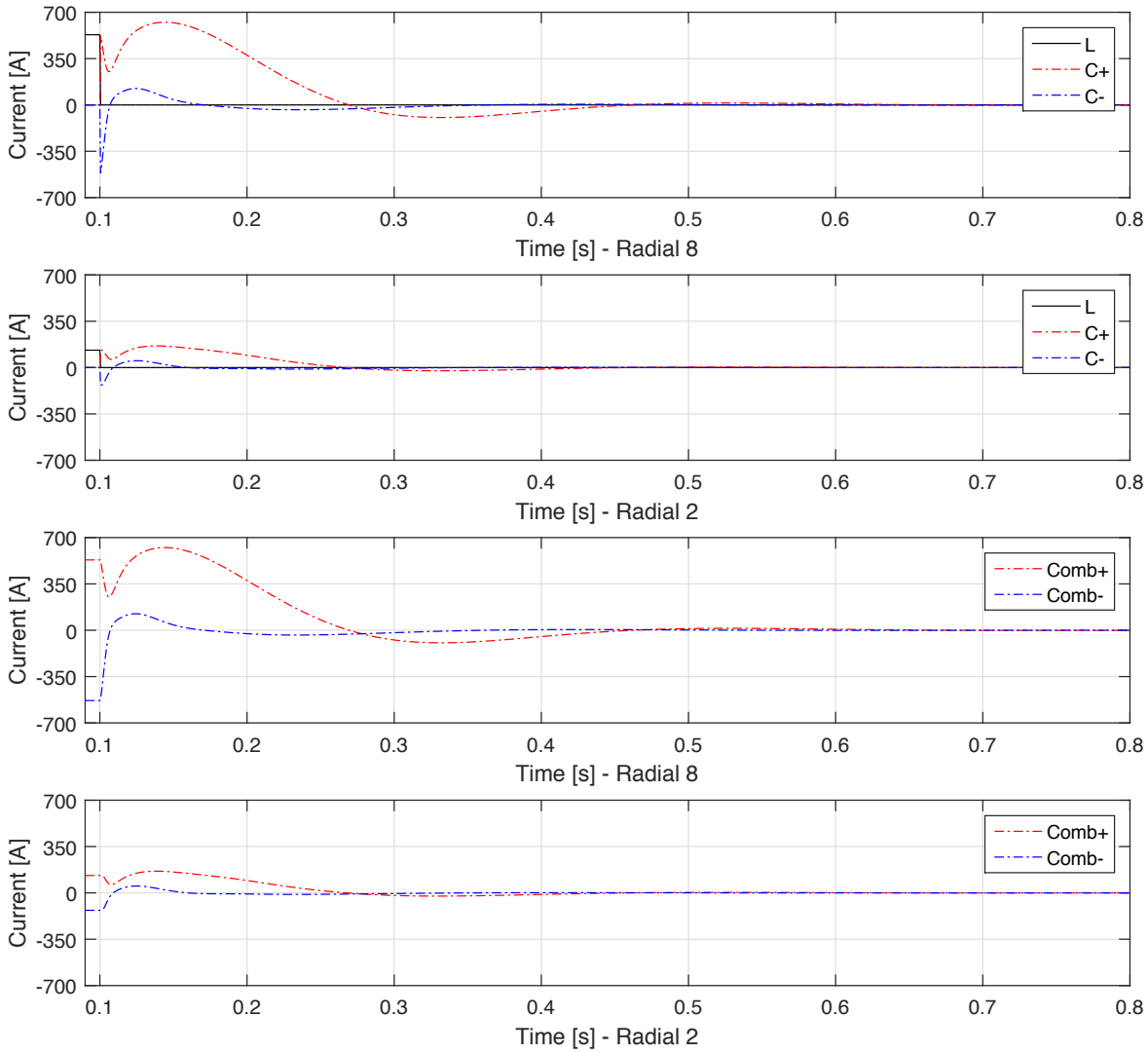


**Figure 5.39:** Comparison of currents measured at radials 2 & 8

In figure 5.39 it is seen that the inductor current goes to zero at the time of the fault and does not rise again. The positive capacitor discharges until 0.27 s, after which it charges again until 0.45 s followed buy a small discharge. The negative capacitor discharges at the instance of the fault, but charges again at 0.11 s followed by a lengthy low current discharge which reaches zero at 0.35 s. Looking at the currents in the third and fourth graph, they are seen to follow the same trends as the capacitors.

Table 5.3 contains the measured absolute maximums values during the unbalanced fault case.

| | **Unbalanced fault** | | |
|---|---|---|---|
| | **Conductor** | **Sheath** | **Armour** |
| V | 59586 | 6069 | 6069 |
| A | 8914 | 5172 | 1968 |

**Table 5.3:** Maximum values measured at radial 1 during an unbalanced fault

### 5.4.7 Conductor to sheath fault

In the final case there is a positive conductor to sheath fault at the end of radial 1.

**Substation**

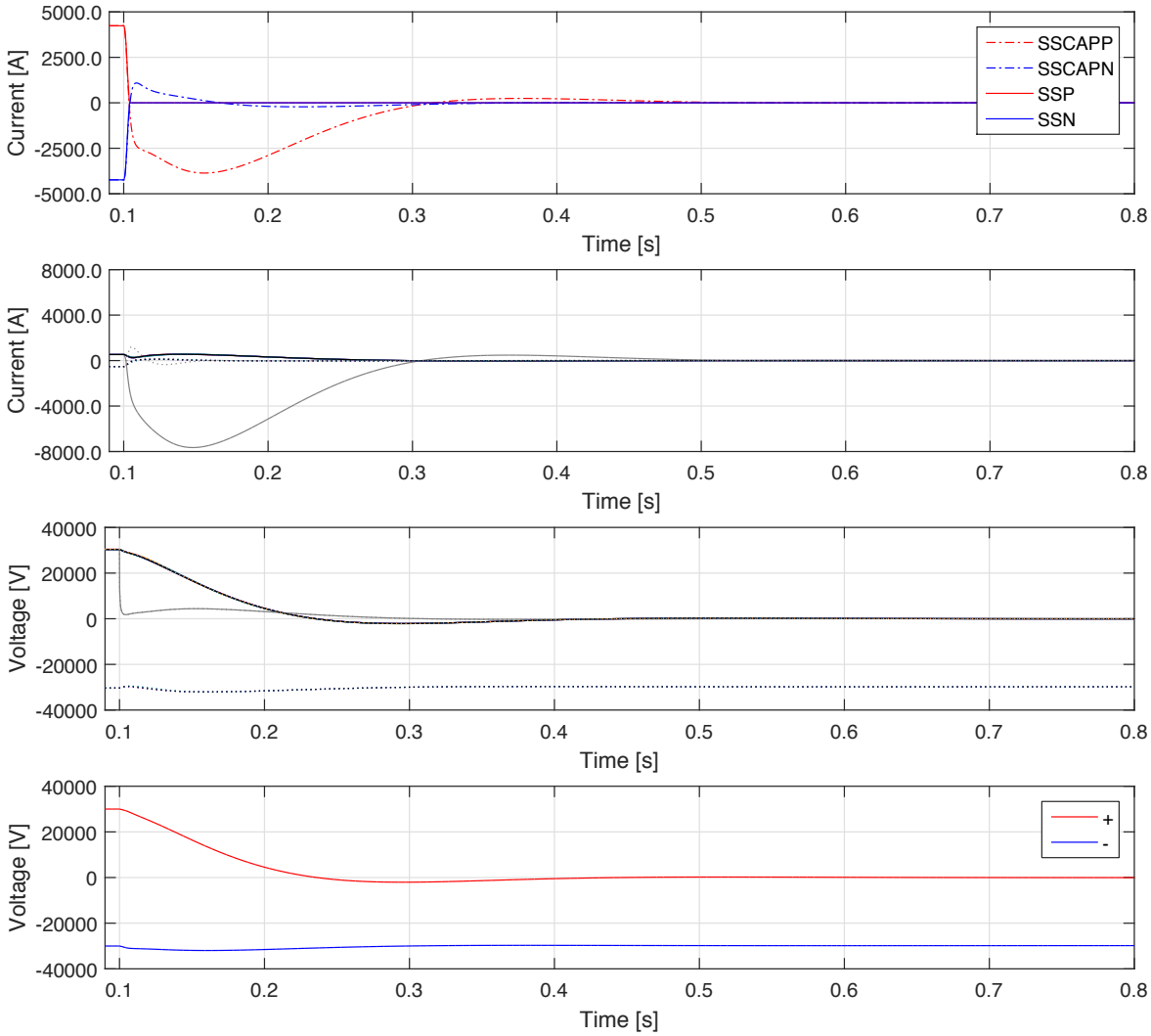


**Figure 5.40:** Currents and voltages measured at the substation

The first graph in figure 5.40 shows the substation capacitor currents, where the positive capacitor discharges until 0.3 s. The negative capacitors discharge is considerably smaller and crossing zero at 0.16 s. The second graph shows the radial currents where close to 8 kA is flowing towards to fault. The slope of the radial voltages in the third graph even out at 0.3 s, which coincides with the current crossing zero in the two graphs above. The single grey line going towards zero is the voltage measured in the faulted radial. The last graph shows the substation voltage, which follows the radial voltages closely. The negative phase is somewhat steady, explaining the small capacitor discharge in the negative conductors.

**Radial 1**

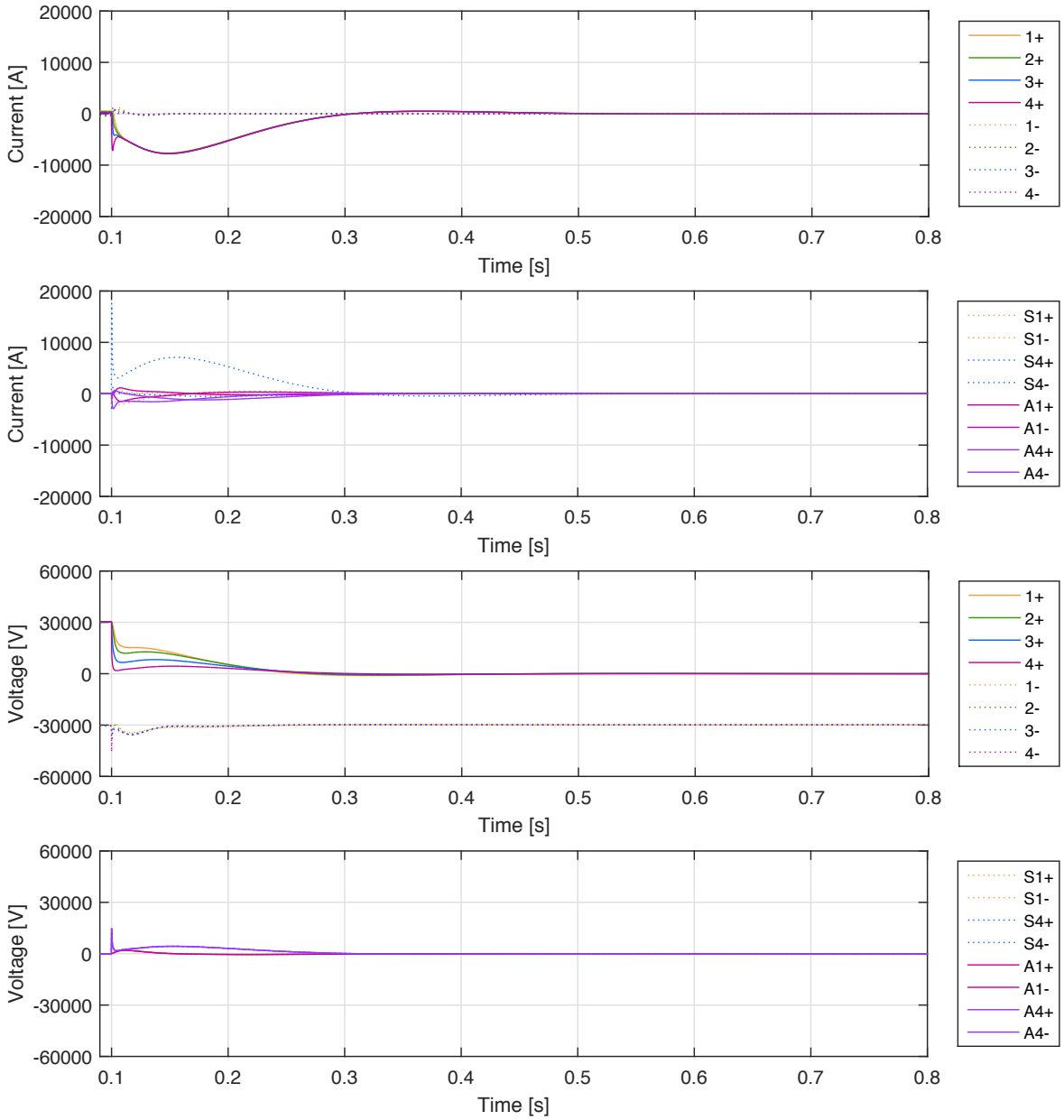


**Figure 5.41:** Currents and voltages measured at radial 1

The second graph in figure 5.41 shows a very high current spike at the time of the fault reaching almost 18 kA. Comparing it to figure 5.38 in the unbalanced case and adding the conductor, sheath and armour currents would explain the amplitude since the sheath and armour are grounded together all the current would go to the same point.

**Radial 2 & 8**

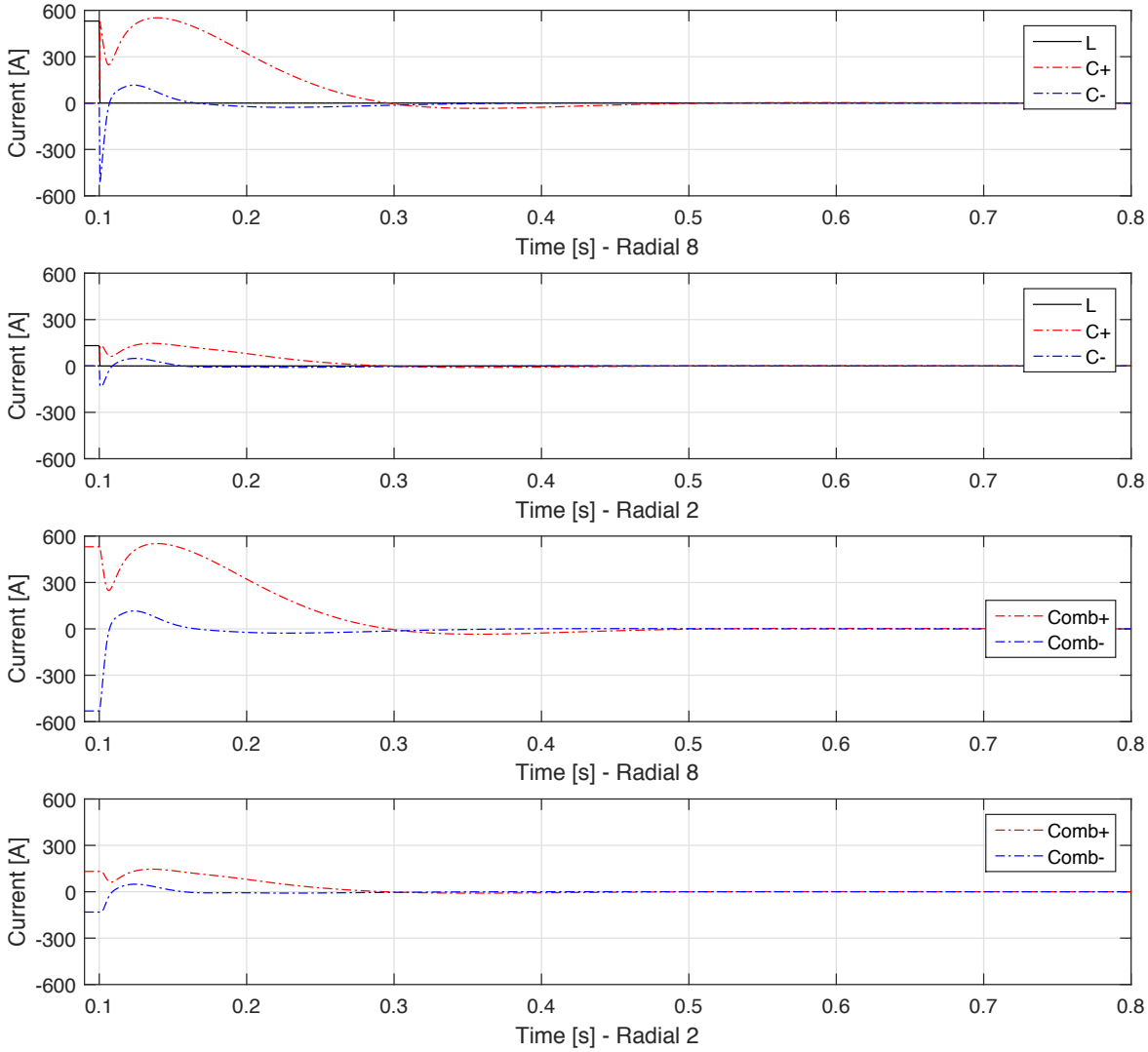


**Figure 5.42:** Comparison of currents measured at radials 2 & 8

Figure 5.42 follows the same trends as in the unbalanced case in figure 5.39, but with a lower amplitude since the current has to go through the 1 Ω ground resistance, compared to the 0.1 Ω fault resistance in the conductor to ground faults.

### 5.4.8 Conclusion - Fault Analysis

From the different fault analysis made, it was seen that the lumped radials compared well to the unlumped radials, having similar waveforms throughout the cases, where it was also seen that the capacitors have the majority of the current contribution. Looking at the substation, it was clear that it did not import power during faults and stopped exporting when the voltage dropped below limits. A polarity reversal was seen in some cases which resulted in the capacitors being able to recharge and discharge at diminishing levels. This effect was due to the DC/DC converters providing a free wheeling path, even though these actually inhibit the fault driven voltage reversal. The polarity change could be further improved by installing smoothing reactors as series output filters to completely suppress the voltage reversal.

### 5.4.9 Highest stresses for cable dimensioning

Having concluded the different simulations and noted the maximum cable stresses, these can now be collected in a table to see the worst cases for the conductor, sheath and armour.

| | **Maximum stresses** | | |
|---|---|---|---|
| | **Conductor** | **Sheath** | **Armour** |
| V | 59586 (U) | 6069 (U) | 6069 (U) |
| A | 12294 (B) | 9341 (B) | 4304 (B) |

**Table 5.4:** Maximum values measured in all simulations conducted - (B) is balanced fault - (U) is unbalanced fault

Table 5.4 shows that the maximum voltages are all in the unbalanced case and the highest current stresses are in the balanced case. Which is to be expected since an unbalanced fault will cause the unfaulted conductor to try to maintain the substation voltage level. Short circuiting the positive and negative phase result in the highest current magnitude since they both carry current.

Table 5.5 contains the highest voltage stresses measured in the conductor in all of the 18 fault cases. The worst case has been identified as the 1.1 pu phase to ground fault at turbine 4, which results in a voltage magnitude of 65882 V. The table contains information about maximum voltage, location of fault and at which time it occurred. The location is written as 1A-D, which is radial 1, A is the cable closest to the substation. In which phase the measurement was made is also noted, P/N is when the magnitudes are the same in both. The time of the fault was at 0.1 s.

| | **fault type:** | **P2N at turbine** | | **P2G at turbine** | | **P2S in cable** | |
|---|---|---|---|---|---|---|---|
| $U_{sub}$ | **fault location:** | 1 | 4 | 1 | 4 | 1 | 4 |
| 0.9 p.u. | maximum voltage | 27415 | 27415 | -53701 | -54174 | -36283 | -41228 |
| | location | 1D: P/N | 1D: P/N | 1A: N | 1D: N | 1D: N | 1D: N |
| | time | 0.1 | 0.1 | 0.1 | 0.1 | 0.117 | 0.1 |
| 1.0 p.u. | maximum voltage | 30374 | 30374 | -53701 | -59586 | -60021 | -45678 |
| | location | 1D: P/N | 1D: P/N | 1A: N | 1D: N | 1A: N | 1D: N |
| | time | 0.1 | 0.1 | 0.1 | 0.1 | 0.1 | 0.1 |
| 1.1 p.u. | maximum voltage | 33340 | 33340 | -65478 | -65882 | -49448 | -50139 |
| | location | 1D: P/N | 1D: P/N | 1A: N | 1D: N | 1A: N | 1D: N |
| | time | 0.1 | 0.1 | 0.1 | 0.1 | 0.1 | 0.1 |

**Table 5.5:** Maximum conductor voltages reached in simulated fault cases, worst case marked red (P: positive conductor, N: negative conductor, G: ground, S: sheath)

The data for sheath, armour and the conductor current will not be shown here since it will be used in following chapter and discussed there.

## 5.5 Conclusion - Transient Analysis

The first aim of the transient analysis chapter was to find a recommendable grounding strategy. Several simulations were made with three different grounding strategies. It was clear that the cables needed to be grounded at both ends to keep the otherwise very high voltages down. The maximum stresses found in the conductor, sheath and armour will be used in the subsequent chapter to see if any protection is required. The measurements made in this chapter will be used to see if insulations hold and if temperatures are within limits cables limits.

### 5.5.1 Discussion of results

When using simulation software it is always necessary to be critical and to question the validity of the results. Transient behaviour and frequency can be somewhat accurately represented, but magnitudes are a different matter. Specific data of components and surroundings are often based on information found in standard tables, which could differ from proper measurements. During these simulations contribution from the turbines was always assumed to be zero, since they were turned off at the time of the fault, where an actual system would contain various measurement and communications delays which would mean there would be some contributions from the turbines. It was however seen that the majority of the current contributed to the faults was from the capacitors.

# Validation of System Design 6

This chapter aims to validate the suitability of two parts of the initial system design, proposed in chapter 3, based on the simulation results from chapter 5. The first section picks up on the cable design and tests if it is able to withstand the transient stresses occurring in the simulated fault cases. The second section discusses the initial hypothesis, that a simple system design without other protection devices than disconnectors is possible.

## 6.1 Validation of Cable Dimensioning under faulted Conditions

When the cable dimensions were determined in chapter 3, only normal operation had been taken into consideration. However, it has to be ensured that the cables are able to withstand the stresses during transients caused by faults in other locations of the PCN, as simulated in section 5.4 of this chapter.

Therefore the transients have to be compared to following criteria:

- The electric field stress in the insulation has to be below the dielectric strength of the material. As the electric field distribution is temperature dependent, the temperature difference over the insulation must stay below a specific value in order to avoid too high electric stresses in the insulation.
- The current flow in the conducting parts of the cable - conductor, sheath, armour - causes dissipation of energy and heating of the cable. To avoid decomposition of the insulation and other PE layers the maximum allowable temperature in any cable layer is 90°C in continuous operation. During short circuits, the conductor temperature can go up to 250°C for up to 5 seconds [22]. Furthermore many manufacturers refer to a so called "emergency load", allowing the cable to heat up to between 105°C and 130°C for up to several hours at once and up to 100 hours per year without having significant impact on the insulation material and cable lifetime [25], [26].

### 6.1.1 Electric Stress in Insulation

The electric field distribution in the DC cable insulation depends (in addition to the cable geometry) on its temperature and conductivity, which both vary with distance to the conductor. Consequently, heating of the insulation material due to current flow in the conductor influences the field distribution and hence the peak electric stresses that the insulation has to withstand. The higher the temperature difference over the insulation, the higher becomes the peak value of electric field stress [20]. If this peak surmounts the dielectric strength in the insulation, an electric breakdown is likely to occur.

According to section 3.2 the insulation thickness was determined using a conservative approach, being supposed to withstand up to 2.5 times the rated pole to earth voltage assuming maximum allowable temperature of 90°C in the conductor and ambient temperature (10°C) in the sheath. Consequently the cable insulation is designed to withstand up to 75 kV in the conductor for a temperature drop of 80 K in the insulation. Given that the temperature limit of 90 °C is not surpassed and the absolute

value of the conductor voltage stays below 75 kV, the electric field stress will therefore stay below the dielectric strength of the material.

In addition to the main insulation, the separation sheath (between sheath and armour) and the oversheath (between armour and seabed) have to withstand electric stresses caused by voltages in sheath and armour to avoid breakdown.
Comparing results from the simulated fault cases shows that there is no difference between the measured sheath and armour voltages of the same cable section in any case. Consequently there is no potential difference over the separation sheath, which is not at risk of suffering an electric breakdown.
Regarding the oversheath, the worst case voltages are first identified. Considering that the electric stress in the layer depends among others on the cable geometry, this has to be done by differentiating between the sections with big and with small cable design respectively. For the big cables, the worst case armour voltage of 5.7 kV occurs when there is a phase-to-ground fault at turbine 11, which is the closest turbine to the substation in the same feeder. The stresses over the outer sheath are calculated in analogy to the calculations explained in chapter 3.2.2 for the main insulation. According to the results regarding cable heating (compare subsection 6.1.2), the armour temperature remains below 60°C in the cable sections featuring the big cable, hence a maximum temperature drop of 50 K over the outer sheath can be assumed. This leads to a maximum stress of 11 kV/mm in the outer sheath, which is well below the dielectric strength of PE being 18.9 kV/mm or higher [27]. It has to be added that this worst case includes the faulted cable section itself, so the real stresses in the unfaulted PCN parts will be even lower.
For the small cable, the worst case armour voltage amounts to 16.1 kV, when there is a conductor-to-sheath fault in cable section 1D, the most remote cable section in that feeder, under a pre-fault substation voltage of 1.1 p.u.. As for the big cable a maximum temperature drop of 50 K can be expected. The peak electric stress under this condition is 27.5 kV/mm, which is higher than the dielectric strength of the material. However, this peak voltage was measured at the faulted cable itself, which needs to be replaced anyway. The highest measured voltage in an unfaulted cable amounts to 2.5 kV in the case of a conductor-to-sheath fault in cable section 1A under a pre-fault substation voltage of 1.1 p.u., causing a maximum electric stress of 5 kV/mm in the outer sheath of the small cable sections. This will not cause any problems to the PE oversheath.

### 6.1.2 Temperature Rise in Conducting Layers

Described in appendix A.5 the conductor temperature during steady state is defined by equation 6.1, where $\Theta_c$ and $\Theta_{amb}$ are conductor and ambient temperature respectively, $I_{cont}$ is the continuous conductor current, $R'$ is the resistance per unit length of the cable and $\sum T_i$ comprises of thermal resistances 1 to 4 as defined in chapter 3.2.1.

$$\Theta_c = \Theta_{amb} + I_{cont}^2 R' \cdot \sum T_i \tag{6.1}$$

During transients, the change in current flow results in changing power dissipation. On the other side, the power outflow through the outer cable layers changes much slower, as explained in [18, ch. 3.1.3]. Consequently, the difference between power dissipation and outflow causes heating in the conducting layer. Equation 6.2 describes this relation mathematically. Here, $I_{fault}$ is the time dependent fault current in the conducting layer, $c_p$ is the specific heat of its material, $m$ its mass per unit length and $\Theta_{fault}$, $\Theta_{cont}$ the time dependent temperature during the fault and the continuous conductor temperature respectively.

$$\int I_{fault}^2 R' dt - \int I_{cont}^2 R' dt = c_p m(\Theta_{fault} - \Theta_{cont}) \tag{6.2}$$

For the estimation of the temperatures during a transient, adiabatic heating is assumed, i.e. the excess heat is retained inside the cable layer which is carrying the current responsible for it. This layer can be conductor, sheath or armour of the cable. Being designed with different materials, table A.2 in appendix A.2 summarizes the material constants required for the calculations.

Knowing the fault currents from simulations in this chapter and obtaining pre-fault temperatures as well as power outflow from load flow simulations, the evolution of the temperature during the fault is given by equation 6.3. It is assumed that $R'$ remains constant during the fault.

$$\Theta_{fault}(t) = \frac{\int I_{fault}^2 R' dt}{c_p m} - \frac{\int I_{cont}^2 R' dt}{c_p m} + \Theta_{cont} \tag{6.3}$$

Table 6.1 summarizes the maximum temperatures reached for the different simulation cases.

| | **fault type:** | **P2N at turbine** | | **P2G at turbine** | | **P2S in cable** | |
|---|---|---|---|---|---|---|---|
| $U_{sub}$ | **fault location:** | 1 | 4 | 1 | 4 | 1 | 4 |
| 0.9 p.u. | maximum temperature | 85.2°C | 96.9°C | 84.2°C | 94.8°C | 83.5°C | 91.9°C |
| | location | 1A: P/N | 1C: P/N | 1A: P | 1C: P | 5A: P/N | 1C: P |
| 1.0 p.u. | maximum temperature | 69.3°C | 83.3°C | 68.1°C | 80.8°C | 67.3°C | 77.3°C |
| | location | 1A: P/N | 1C: P/N | 1A: P | 1C: P | 1A: P | 1C: P |
| 1.1 p.u. | maximum temperature | 58.7°C | 75.0°C | 57.2°C | 72.2°C | 56.3°C | 68.1°C |
| | location | 1A: P/N | 1C: P/N | 1A: P | 1C: P | 1A: P | 1C: P |

**Table 6.1:** Maximum cable temperatures reached in simulated fault cases, worst case marked red (P: positive conductor, N: negative conductor, G: ground, S: sheath)

As to be expected, the highest temperatures for every fault type occur for the minumum acceptable steady state voltage of 0.9 p.u. at the substation, since the current flows are highest in this case. This means that for this case the steady state temperature of the cable before the fault is already highest, and consequently further heating due to fault energy dissipation most critical. Pre-fault temperatures of conductor, sheath and armour for all regarded substation voltages are presented in appendix A.6.
Furthermore, for every fault case the conductor reaches the highest temperatures when the fault is located at the remote feeder end. The highest temperature occurs in the C-section of the faulted radial, even though the D-section is closer to the fault and would hence be expected to become warmer. However, in steady state the current flow through the D-section amounts to only half of the current flow in the C-section, therefore its pre-fault temperature is considerably lower and consequently its peak temperature is lower, too.
In case that $U_{sub} = 0.9\ p.u.$ the conductor temperature in cable section 1C exceeds 90°C in all cases, when the fault occurs at the remote feeder end. It declines with approximately $0.2\frac{K}{s}$, after the current decays. For the worst case, a phase-to-phase fault at turbine 4 with the peak temperature amounting to 96.9°C, it takes 34.5 s until the conductor temperature will be within the allowed long term temperature range of 90°C again. This fits well into the allowed time and temperature ranges for emergency load mentioned before. Furthermore it should be considered that the calculations, which the regarded results are based on, assume quasi-adiabatic heating of the conducting layers. In reality, heat transfer into the adjacent materials will increase during the fault, causing reduced heating of the conductor. It may be worth recalculating the temperature results considering this effects. For AC cables, the standard IEC 949 [28] gives a guideline to estimate the influence of this non-adiabitic effects. However, there is no guideline for MVDC cables so far.
Another point to consider is the temperature drop over the insulation when the temperature in the conductor is above 90°C, as it was dimensioned considering a maximum drop of 80 K. Comparing to the pre-fault sheath temperatures given in table A.6, appendix A.6, it is seen that this is not an issue, as the pre-fault temperature in the sheath amounts to 55.1°C for 0.9 pu in section 1C, which means

the maximum temperature difference remains below 80 K.
Apart from section 1C all temperatures remain under the 90°C limit for all simulated cases.

Concluding this section, it can be said that the cables are properly sized regarding electric stresses and temperatures occurring in the simulated fault cases. However, an optimization of the cable can be advantageous regarding two aspects. As the peak electric stresses in separation sheath and oversheath stay well below the dielectric strength of their material, the layer thickness could be reduced. This would also improve the heating of the cable during steady state operation. Regarding temperature, a bigger conductor cross section could be chosen in order to reduce temperatures during continuous as well as transient operation. This in turn, may reduce the necessary main insulation thickness since the peak electric stress is dependent on the temperature drop across the insulation. Consequently, a smaller cable design might be achievable.

## 6.2 Discussion of System Protection

Protection can generally fulfil several objectives. One of them is separating the faulty part of the system from the sources that are feeding into the fault in order to reduce peaks and duration of the fault response. Another one is to prevent the fault from pulling down the voltage of the entire system by isolating the faulty part. Finally, can aim at isolating the fault location in order to prevent an amount of energy dissipation in the system that would cause damage to the unfaulted system parts. Subsection 6.1.2 has shown that this last aspect is not of concern for the regarded cable system. Energy dissipation in other components is outside the scope of this project.

In the regarded WPP, the only power sources are wind turbines, which are connected to the PCN via DC-DC converters. In case of a fault, the inverter transistors on the low voltage side of the converter can be switched of fast, so that within 10 $\mu s$ no power is fed from the turbines into the PCN any more, which is part of the individual wind turbine protection. From the HVDC link no power can be imported, as the SAB converter configuration allows only unidirectional power flow out of the WPP. However, the energy stored in the PCN will feed into the fault.
The medium frequency transformers in the turbine and substation converters, the turbine converter output filter capacitors and substation converter input filter capacitors and the MVDC cables themselves constitute these energy storages. Together, they form a complex R-L-C circuit in the wind farm, which shapes the transient voltage and current response until the system is completely de-energized and all energy dissipated, if there is no protection which isolates the fault.
In any case, the system has no sources to continuously feed into the fault, therefore static short circuit current contributions are not present and only dynamic fault contributions are an issue for the chosen PCN design. For considerations of protection this means that an investment in costly devices is only reasonable, if they can act fast enough to prevent depletion of the system voltage below the minimum tolerable value to maintain operation of the unfaulted part of the system.

As stated in chapter 3.1.6 it is preferable to keep the system as simple as possible. Disconnectors have to be installed in the system to allow save maintenance of all components. However, if no further switchgear is installed, the time of interruption of supply is defined by the natural transient response of the occurring fault and cannot be influenced. Only after all energy is depleted can the faulted part of the system be isolated and operation of the rest of the system be resumed, starting with a re-energisation which will add up to the duration of the interruption.
Another option is to install breakers. Conventional AC breakers rely on a zero crossing of the current to avoid arching during disconnection. The utilization of this technology is only reasonable, if the first zero crossing of the current through the breaker that needs to open in order to isolate the fault occurs before the system voltage drops below a critical level.
Finally, DC breakers can be considered. Different types of DC breakers were discussed in chapter 2.4.3. As in the case of AC breakers, the time which the device needs to break the current at the

required position is crucial for the decision if it is worth to invest in the costly equipment or not. However, DC breakers have the advantage that they can create an artificial zero crossing, hence they can react earlier compared to AC breakers, and the only concern is that the operation time of the device itself is fast enough. A general choice can be made between devices operating mechanically, which are comparably slow, solid state devices, which are considerably faster, and hybrids. Considering the fast depletion of energy in the system, solid state breakers seem most promising. However, power electronic devices are costly and have the disadvantage of causing on-state losses during normal operation. Other properties that are of importance for the choice of breaker technology are consumption of space on the platform and required additional equipment such as cooling devices when using power electronics. It should also be considered that all additionally installed equipment requires additional maintenance.
In the end, the choice of a suitable protection strategy is a trade off between costs associated with the additional equipment and savings due to avoided interruption of supply to the external grid.

Resulting from these considerations, three scenarios for the protection are derived and compared regarding their loss of production. The first two scenarios assume that all feeders are connected to one big DC-DC converter at the offshore substation and compare the scenario where only disconnectors are installed in the system to the scenario where breakers are utilised. The third case takes into consideration different layouts of the substation, which were discussed in chapter 3.1.5. For this analysis, it is assumed that the entire faulted radial will be isolated at the end of the sequence of actions in all scenarios and for all fault cases. Identification of the faulted feeder can be made by current measurements into the substation. A reversal of the current flow direction indicates the fault location. Energy losses are calculated based on average power production of the WPP, when the site features an annual average wind speed of 11 m/s, which is a typical value for well chosen offshore WPP sites.

### 6.2.1 No Protection Devices

In this first scenario, no further equipment is installed in addition to the disconnectors. As explained before, this means that the fault transient cannot be actively interrupted and the faulty system part can only be isolated after depletion of the fault currents. For the estimation of downtime it is assumed that the disconnectors can operate when the current through them is within $\pm\ 10A$ for a duration of at least 100 ms. Table 6.2 shows the time until this state is reached for the faulted radial 1, which is the last one to deplete, for the simulated fault cases.

| | **fault type:** | **P2N at turbine** | | **P2G at turbine** | | **P2S in cable** | |
|---|---|---|---|---|---|---|---|
| $U_{sub}$ | **fault location:** | 1 | 4 | 1 | 4 | 1 | 4 |
| 0.9 p.u. | time to steady state | 1.1408 | 0.7969 | 0.7885 | 0.6840 | 0.7067 | 0.8209 |
| 1.0 p.u. | time to steady state | 1.1572 | 0.8053 | 0.7884 | 0.6838 | 0.7068 | 0.8264 |
| 1.1 p.u. | time to steady state | 1.1723 | 0.8117 | 0.7883 | 0.6837 | 0.7069 | 0.8311 |

**Table 6.2:** Time to fault current depletion in radial 1 in simulated fault cases [s], worst case marked red. (P: positive conductor, N: negative conductor, G: ground, S: sheath)

Comparing the simulated cases, it can be seen that the time to depletion varies between 0.68 seconds up to 1.17 seconds. In the turbine fault cases, both balanced and unbalanced, the current needs longer to decay when the fault occurs at a turbine close to the substation than at a remote turbine. For conductor-to-sheath faults in the cable the opposite relation between distance to substation and depletion time is observed, so the longest fault duration is recorded for a remote cable fault. Comparing different pre-fault voltage levels, only small influences on the fault duration can be observed. The worst case is defined by the highest depletion time, as it causes the longest system outage. It amounts to 1.172 seconds in case of a balanced fault at the turbine closest to the substation and a pre-fault substation voltage of 1.1 p.u..

After the faulted radial is disconnected, the system is de-energised and can not resume operation before re-energisation has been completed, adding up to the total downtime of the WPP. The simulation case in chapter 5.4.4 has shown that energization from the turbines takes 205 ms up to rated voltage of $\pm 60\ kV$, provided all turbines are used to bring up the entire system. When one feeder is disconnected only $\frac{7}{8}$ of the turbines are available to energize the system. On the other hand, the faulted feeder does not have to be energized. As equal amounts of energy is stored in the substation capacitor filters as in all turbine capacitor filters together and the energy stored is negligibly small compared to that, it can be said that approximately $\frac{15}{16}$ of the system needs to be energized. Furthermore, the system can resume operation as soon as 0.9 p.u. of the rated voltage are reached. Hence, the time required for energization can be estimated as

$$t_{re-energization} = 0.9 \cdot \frac{15}{16} \cdot \left(\frac{7}{8}\right)^{-1} \cdot 205\ ms \cdot (P_{turb,p.u.})^{-1} \approx 198\ ms \cdot (P_{turb,p.u.})^{-1} \tag{6.4}$$

This corresponds to an energization slope of approximately 273 $\frac{V}{ms} \cdot P_{turb,p.u.}$.

The total outage duration can be estimated by adding up time of depletion and time of re-energization. From energy calculations in chapter 3.3 the average power production of the WPP can be determined. Assuming an average annual wind speed of 11 m/s, the capacity factor $CF$ is defined by

$$CF = \frac{E_{WPP,11}}{E_{WPP,max}} = \frac{1310\ \frac{GWh}{year}}{2243\ \frac{GWh}{year}} = 0.584 \tag{6.5}$$

This means the average energy provided by each turbine is approximately 0.584 p.u.. Substituting this value into equation 6.4 leads to a re-energization time of 339 ms. Consequently, the total outage duration for the example of the worst case fault will be

$$t_{outage} = t_{depletion} + t_{re-energization} = 1172\ ms + 339\ ms = 1511\ ms \tag{6.6}$$

The loss of supply is here defined as the energy which the seven unfaulted radials produce during $t_{outage}$. During this time, the WPP does not export any power. However, the unfaulted feeders could theoretically maintain operation, if the fault would be isolated infinitely fast. Therefore the energy produced by them during $t_{outage}$ is unnecessarily lost. For the regarded case it amounts to

$$E_{loss,supply} = t_{outage} \cdot 7 \cdot 4 \cdot CP \cdot P_{turb,rated} = \frac{1.511\ s}{3600\ s/h} \cdot 28 \cdot 0.584 \cdot 8\ MW = 54.9\ kWh \tag{6.7}$$

Using equations 6.4, 6.6 and 6.7 for operation of rated power would lead to $t_{outage} = 1370\ ms$ and $E_{wasted} = 85.2\ kWh$.

### 6.2.2 Integration of Protection Devices

This scenario suggests the installation of breakers at the substation connection of each feeder. As explained previously, the investment in breakers is only reasonable if they can operate fast enough to prevent de-energization of the system below a minimum tolerable voltage level. It is thus important to know how fast the voltage in the system depletes.

During steady state operation the lower voltage limit is set at 0.9 p.u., however during transients it can drop even lower. The transient limit depends on operating limitations of the equipment connected to the power collection network. To avoid assumptions regarding the magnitude, table 6.3 shows several characteristic times of the voltage decay for all simulated fault cases. The times until the first radial drops below 0.9 p.u. and 0.8 p.u. respectively are measured. Furthermore, since the voltage drop follows a linear function, the voltage drop per time is calculated from this two values. Consequently, the time until a specific voltage is reached can be calculated based on the presented results.

| | **fault type:** | **P2N at turbine** | | **P2G at turbine** | | **P2S in cable** | |
|---|---|---|---|---|---|---|---|
| $U_{sub}$ | **fault location:** | 1 | 4 | 1 | 4 | 1 | 4 |
| 0.9 p.u. | time to 54 kV | 0.0014 | 0.0014 | 0.0014 | 0.0014 | 0.0014 | 0.0014 |
| | time to 48 kV | 0.0085 | 0.0160 | 0.0167 | 0.0305 | 0.0197 | 0.0322 |
| | slope | 0.8451 | 0.4110 | 0.3922 | 0.2062 | 0.3279 | 0.1948 |
| 1.0 p.u. | time to 54 kV | 0.0080 | 0.0152 | 0.0158 | 0.0284 | 0.0184 | 0.0299 |
| | time to 48 kV | 0.0128 | 0.0249 | 0.0276 | 0.0488 | 0.0338 | 0.0523 |
| | slope | 1.2500 | 0.6186 | 0.5085 | 0.2941 | 0.3896 | 0.2679 |
| 1.1 p.u. | time to 54 kV | 0.0120 | 0.0232 | 0.0254 | 0.0455 | 0.0311 | 0.0487 |
| | time to 48 kV | 0.0161 | 0.0312 | 0.0360 | 0.0622 | 0.0443 | 0.0681 |
| | slope | 1.4634 | 0.7500 | 0.5660 | 0.3593 | 0.4545 | 0.3093 |

**Table 6.3:** Time measured until voltage drops to 54 kV and 48 kV at the end of the radials [s], slope of voltage drop [kV/ms], worst cases marked red.
(P: positive conductor, N: negative conductor, G: ground, S: sheath)

Comparing the simulated cases several patterns can be observed. For every regarded fault type, the voltage reaches 54 kV and 48 kV sooner and drops with steeper slope when the fault is located close to the substation than when it is located remotely. Defining the shortest time to 54 kV and 48 kV respectively as well as the highest slope as worst cases, it can be said that in general a phase-to-ground turbine fault is worse than a phase-to-sheath cable fault and a phase-to-phase fault is worst. In addition, the slopes are worse for higher pre-fault substation voltages, and the times to 54 kV and 48 kV are shorter for lower initial pre-fault substation voltages.
Consequently, the worst case is a balanced fault at the turbine closest to the substation. In addition, if the substation voltage is at the lower steady state limit of 0.9 p.u. from the beginning, the radial voltages will drop below that value within 1.4 ms in all cases, which is to be expected.

Consequently, the case of a balanced fault at turbine 11 and a pre-fault substation voltage of 0.9. p.u. is taken as an example to show the dependence between breaker operation time and system downtime. The later the chosen breaker succeeds to isolate the faulted radial, the lower will the system voltage drop. As in the first scenario, the system voltage needs to be raised to at least 0.9. p.u., which corresponds to 54 kV, in order to resume operation.
Table 6.4 shows the dependency between fault breaking time $t_{breaker}$ the total downtime and consequently loss of supply for this example case. The re-energization time is calculated in analogy to scenario 1. As before, the re-energization slope is

$$273\frac{V}{ms} \cdot P_{turb,p.u.} = 273\frac{V}{ms} \cdot 0.584 = 159\frac{V}{ms} \tag{6.8}$$

The total downtime is calculated according to

$$t_{outage} = t_{breaker} + t_{re-energization} \tag{6.9}$$

| $t_{br}$ [ms] | **1** | **2** | **3** | **4** | **5** | **10** | **20** | **30** | **40** | **50** | **60** | **70** |
|---|---|---|---|---|---|---|---|---|---|---|---|---|
| U @ $t_{br}$ [kV] | 54.3 | 53.5 | 52.6 | 51.8 | 51.0 | 46.7 | 38.3 | 29.8 | 21.4 | 12.9 | 4.5 | 0 |
| $t_{re-en}$ [ms] | 0 | 3.2 | 8.5 | 13.8 | 19.1 | 45.7 | 98.9 | 152 | 205 | 258 | 312 | 340 |
| $t_{out}$ [ms] | 1 | 5.2 | 11.5 | 17.8 | 24.1 | 55.7 | 119 | 182 | 245 | 308 | 372 | 410 |
| $E_{loss}$ [kWh] | 0.04 | 0.19 | 0.42 | 0.65 | 0.88 | 2.02 | 4.32 | 6.61 | 8.90 | 11.2 | 13.5 | 14.9 |

**Table 6.4:** Loss of supply depending on time of breaking the fault

It can clearly be seen that the utilisation of a fast breaker is advantageous compared to the first scenario. For breaker times up to 5 ms less than 1 kWh of energy supply is lost, as the downtime remains below 25 ms. The system voltage remains above 0.8 p.u. and can be recovered relatively quickly. For slower breakers the investment becomes less and less attractive, as the loss in supply and down time rise considerably. The longer a breaker needs for its operation, the higher becomes the share of re-energisation in the downtime. In the example, breaker time of 70 ms causes an interruption of supply of almost 15 kWh, which is still less than in the scenario without breakers, but in the same order of magnitude.

Concluding this scenario, if installation of breakers is desired, they should be able to act as fast as possible. Comparing to table 6.3, an operation time below 8 ms seems advisable to prevent the voltage from dropping low in any fault case. However, it is an economical consideration if the saving compared to the scenario without breakers, where only 85.2 kWh of supply are lost in the worst case, are worth the investment.

### 6.2.3 Partial Isolation of the system

This last scenario addresses the influences of different substation designs presented in chapter 3.1.5 on the system downtime and loss of supply in case of a fault. The previous scenarios assumed that all radials are connected to the HVDC link through the same substation converter. It is however possible to install several converters in parallel, so that e.g. two converters are supplied by four feeders each, or four converters by two feeders each.
This has two effects on the system in case of a fault. Firstly, due to the uni-directional power flow of the SAB DC-DC converters, only the turbines and radials connected to the same converter will feed into the fault, which will result in reduced stresses in the system.
Secondly, the feeders connected to different converters than the faulted one can continue operation and supply. In case of a four-converter substation design this mean that during the fault, only one feeder interrupts its supply in addition to the faulted one, reducing the loss in supply to $\frac{1}{7}$ of the values estimated in scenarios one and two. This could result in a reduction of worst case loss of supply from 85.2 kWh to 12.2 kWh compared to scenario one. In case of a two-converter substation design four feeders continue supplying the external grid during the fault,reducing the loss in supply to $\frac{3}{7}$ of the values estimated in scenarios one and two. Once the faulty part of the system is isolated, either by means of a disconnector as in scenario one or by means of a breaker as in scenario two, the other feeders that were connected to the same converter as the faulted radial can re-energize this part of the system and resume their supply to the external grid.
In contrast to the first two scenarios, the external grid is continuously supplied with power during the fault.

Concluding this scenario it can be said that a smart substation design with parallel converters and feeders that are partially isolated from one another can prevent a complete interruption of supply to the external grid and reduce loss of energy supply considerably for the regarded fault cases. This supports the initial hypothesis, that the system can be designed without breakers.

### 6.2.4 Conclusion & Outlook

Concluding this chapter, two parts of the initial system design have been reconsidered based on the results from the transient simulations conducted in chapter 5.

First, the cable design proposed in chapter 3.2 has been validated with respect to field stresses and heating caused by transient voltages and currents of the simulated fault cases. As a consequence, the applicability of recommendations given by AC standard DS IEC 60502-2 [22] regarding sizing of layers outside the main insulation has been verified for the design of MVDC cables used in the proposed PCN. Furthermore a balanced fault at the turbine remotely from the substation has been identified as worst case regarding cable heating.
It could be concluded that the cables are properly sized regarding electric stresses and temperatures occurring in the simulated fault cases. Future work should however consider additional design iterations.

Secondly, system protection has been discussed. The initial hypothesis, that a system design with disconnectors as only protection devices, has been compared to the possibility of installing breakers at the points of connection of each feeder to the substation. Following conclusion could be drawn.

- The time until the current flows in the system deplete below 10 ampere and disconnection is possible vary between 0.68 and 1.17 seconds depending on the fault. The slowest depletion takes place in case of a balanced fault at the turbine nearest to the substation.
- The worst case fault with regard to the beginning of voltage drop in the system and its slope is a balanced fault at the turbine nearest to the substation, causing the fasted de-energization of the system.
- The outage time is in the order of magnitude of 1 to 2 second if no breakers are installed. The loss of supply from the unfaulted feeders amounts to 85 kWh in the worst case.
- A more complex substation design with several DC-DC converters installed in parallel is advantageous when it comes to loss of supply during faults. This approach seems most promising for a system without breakers, supporting the initial hypothesis.

The observations and comparison made in this section are based on the ideal assumption, that the fault is detected in the instant it happens, and that this information is available everywhere in the system. In reality this is of course not the case. Part of the protection task is detection of the fault by measurement of characteristic values. For any protection scheme, discrimination between normal and faulted operation has to be ensured. Therefore, the borders between these modes of operation should be clearly mapped. Future work should pick up on these aspects and continue with the development of a protection algorithm.

# Conclusion & Outlook 7

In order to conclude this thesis, the main chapters will be discussed and lastly the objectives will be reviewed in order to see if the success criteria have been reached.

In system design focus was placed on identifying major changes between AC and DC wind farm concepts. It was seen that an AC collection network required two substation to transform MVAC to HVAC and then HVAC to HVDC. The proposed DC system only required one substation for converting MVDC to HVDC. DC cable design was also analysed and it was concluded that the different physical principles in AC and DC regarding electric fields and ampacity meant that cables designed for AC systems could not be used in a DC PCN without considering a variety of factors. It was therefore decided to propose a sizing algorithm for MVDC cables, generating required cable dimensions for various considered voltage levels. A voltage level of $\pm 30kV$ was chosen which resulted in cable sizes of 50 $mm^2$ and 175 $mm^2$. An overview of the energy production and system losses was also presented. An estimated annual energy production of 1300 $GWh/year$ for an average wind speed of 11 $m/s$ was calculated and the annual energy losses were found to be 9.5 $GWh/year$ at the same wind speed.

An approach to control the PCN was devised, with its main tasks being able to deliver amount of power requested, and to keep the system voltage within allowable limits. The developed control scheme operates with a power reference as input which considers substation voltage disturbances, and has turbine converter current as output. The control was seen to follow a given power reference, however since linear control theory was utilised, considerable steady state errors were seen as the substation voltage and power reference deviated far from the point of linearisation, which emphasizing the necessity to develop a voltage control at the offshore substation in future work. A voltage limiter loop was successfully implemented to reduce currents if necessary to keep the voltages within boundaries. During load rejection the turbine current was reduced to zero to maintain voltage, but exceeds limits by only 2% in the worst case, due to time delays in the control.

Transient analysis was conducted in order to choose a grounding strategy and identify characteristic waveforms, highest stresses for cable dimensioning and worst case faults. A small three-turbine wind farm was designed in PSCAD in order to find areas of interest in the full scale model. During these simulations it was concluded that both cable ends would need to be grounded in order to keep voltages in the sheath and armour within acceptable levels. It was also seen that by way of measurements in the cable, placing them at the ends of the cables would be sufficient since the highest stresses were found to be there.
The next step was simulate with the full model, with a focus on verifying the model itself and to find the maximum cable stresses to see if the cable was designed properly. Comparing transients in the lumped and un-lumped radials showed that they were comparable. The sources of the general shapes and magnitudes of the waveforms were identified and the causes of these discussed. Some polarity reversal was seen which was caused by a free-wheeling in the DC/DC converters. This allowed the capacitors to recharge and discharge at lower amplitudes until depletion.
The highest voltage stress was found when simulating a phase to ground fault at turbine four in radial 1 with a substation voltage of 1.1 p.u.. The fault voltage reached close to 66 kV in the negative

conductor.

The last task in the thesis was to validate the system design. First the cable dimensioning was scrutinised. The conductor insulation was designed with a safety margin of 2.5, which amounts to 75 kV with a temperature of 90°C, which is 9 kV over the maximum voltage registered in the fault cases. Since the voltage in the sheath and armour was the same, due to them being grounded together, the insulation between them did not have any significant potential difference. The oversheath was also within limits for the fault cases, apart from in the faulted cable itself in case of a phase to sheath fault, but this was seen as irrelevant since the cable would need replacing anyway.
The dissipation of fault energy due to current transients in the conducting layers was also examined. Calculating the steady state temperatures in the conducting layers and using the fault currents from PSCAD to calculate the temperature rises, resulted in identifying the worst case as the phase to neutral fault at turbine 4 during 0.9 p.u. substation voltage. In this case the temperature reached 96.9°C and stayed over the 90°C limit for 34.5 s. Considering the temperature ranges for emergency load, this is not seen as a problem. Furthermore the calculations assume quasi-adiabatic heating of the conducting layers, where in a real system there would be heat transfer into adjacent materials and as such reducing temperatures. The applicability of the AC standard, DS IEC 60502-2 [22], considering sizing of layers outside the main insulation, has been verified for the design of MVDC cables used in this thesis.
For the design of the DC wind farm, the focus was on having as few components as possible to reduce cost. Disconnectors will always be needed to allow for maintenance, so these were the only components considered by way of protection. Analysing fault cases showed that longest time until decay of the fault, which was defined as current remaining below 10 A to allow disconnection, was in case of a balanced fault at the turbine nearest the substation. The same fault also accounted for the fastest drop in system voltage, defining the maximum amount of time a breaker would have to isolate the faulted radial. If however no breakers were installed, the outage time would be around 2 seconds and the loss of power from the unfaulted radials amounted to 85 kWh. Substation designs were also re-discussed, were the benefits of having multiple DC/DC converters installed in parallel would mean that the wind farm could supply power during faulted scenarios. This would be advantageous in a system without breakers and support the hypothesis that a simple design can be feasible.

The objectives listed as the success criteria in chapter 1 consisted of five points. Subsequently it will be revised if they have been fulfilled.

- *Design of a MVDC power collection network concept.* - A $\pm 30kV$ system was selected. It uses two different MVDC cable designs, with a conductor cross section of 50 and 175 $mm^2$ respectively. The MVDC side of the SAB DC/DC converters is filtered by parallel capacitors with a time constant of 50 ms and midpoint grounding. Sheath and armour are grounded together and on both ends of every cable section. The system contains disconnectors, but no breakers. All radials feed into a single substation converter. Expected energy losses in the MVDC cables amount to less than 0.8%.
- *Development of a control scheme for the MVDC power collection network.* - A power control scheme for the wind turbine converters was developed and implemented into the PLECS model of a single feeder. The turbine power follows a given reference by adjusting the output current according to measured output voltage. In case of an overvoltage at the end of a feeder, all turbines within the same feeder reduce their power accordingly.
- *Development of a protection scheme for the MVDC power collection network.* - The system was designed to have no fault current contribution from the turbines or HVDC link. Only energy stored in the system feeds into the fault, so that no static fault currents occur. Therefore the protection scheme aims at isolating the faulty feeder by opening its disconnector after the transient short circuit currents have decayed.
- *Conduction of case studies to characterize the system behaviour.* - Three fault cases were

considered: phase-to-phase and phase-to-ground faults at the turbine converter outputs and conductor-to-sheath faults in the MVDC cables. Different fault locations and pre-fault voltage levels were considered. Transient responses were analysed and worst cases identified.

- *Assessment of applicability and weaknesses of the proposed system design.* - It was shown that the proposed system and MVDC cable design are able to withstand peak stresses in steady state and transient operation. However, some weaknesses were identified. Polarity reversal during fault transients suggest the employment of smoothing reactors at the DC/DC converters. Utilization of a multi-converter substation topology is preferable with regard to transient magnitudes and loss of supply in case of faults and seems more promising for the system design without breakers.

It can be concluded that all points have been fulfilled, to the extent that the limited time frame of the project allowed.

As mentioned in the beginning, the idea of utilizing DC power collection networks is a new concept, where no practical experience has been gained so far. Consequently, a lot of research is required regarding case studies as were conducted in this project in order to identify most promising system design concepts. The field of future work being very wide, some suggestions are made subsequently, picking up on the findings of this project.

- During the simulations in PSCAD, the turbines had no contribution to the faults as they were assumed to stop supplying power at the time of the faults. In a real system however there are delays attributed to measurement and communication protocols, so the turbines would supply power for that time. The effects of this extra fault contribution could be investigated to see if they would have an impact on the system design.
- Many aspects of system energisation could be explored. Connecting the whole system at once could lead the damaging transients, so connecting one radial at a time, or all the radials at the same time with the turbines disconnected, so they could then be connected one by one should be analysed. Different sequences to switch in feeders should be examined to find the fastest sequence which would have the lowest adverse effects, such as inrush currents.
- The cable design could be optimised by considering non-adiabatic heating, which would result in lower temperatures in the conducting materials, which then in turn could be reduced. A sensitivity study should be made where the design could be re-iterated to find the optimum considering losses and conductor size, insulation and maximum voltage stresses and so forth. The goal being to have as cheap cables as possible which would still satisfy safety and reliability criteria.
- Including the converter topologies would add a variety of new considerations. A control scheme for the substation could be devised which would open up opportunities for managing the voltage. The size of the capacitors could also be revised if the converters were modelled fully. Their size could be adjusted by examining the ripples from the turbine converters and adjusting them accordingly. This would then have effects on control speed and the total amount of energy into faults. Harmonic analysis could also be performed to see how the converters would affect stability and power quality.
- Different detection and protection algorithms should be considered. The number of measurement points required for acceptable fault detection should be considered in order to reduce the number of physical devices, and as such cost. The protection algorithms would need to consider the least amount of turbines disconnected for the shortest amount of time to keep power supply at maximum.

- Fault scenarios other than those performed in this thesis could be simulated. If the turbine converters were included, faults could be placed in and around them to identify possible weaknesses. Modelling the substation would mean that the affects of faults on it could be monitored. Internal safety features could also be taken into account.
- Modelling the different radial structures mentioned in this thesis should be done with respect to minimising total cable costs, reliability and transmission losses. Protection schemes should be considered for the various designs to see which design would yield the most efficient and reliable system.
- As was seen in the fault analysis, a polarity reversal could occur which was caused by a free-wheeling path in the converters. Implementing smoothing reactors would reduce or eliminate these, but it could be investigated if the polarity reversal would be beneficial by way of getting a faster zero crossing, and as such be able to break faulted areas quicker. The effects of voltage reversal on the cables should be carefully considered first.

# Appendix A

## A.1 Cable models

In this section the different types of cable models available in PSCAD will be presented and analysed. The benefits and shortcomings of the models will be compared in order to chose a method to use for the transient simulations.

### Nominal $\pi$ model

The nominal $\pi$ model has half of the shunt admittance lumped at each end of the cable and the total series impedance added together. The nominal $\pi$ model can be seen in figure A.1. This model is recommended for shorter cables due to the lumped values. [1]

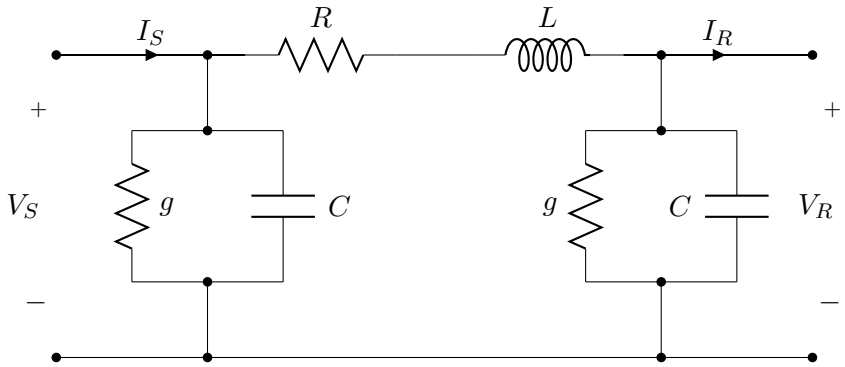


**Figure A.1:** Nominal $\pi$ model

The shunt capacitance is calculated as equation A.1, where g is the conductance in Siemens and l is the line length in meters. The line impedance is calculated in equation A.2.

$$Y = (g + j\omega C)l \tag{A.1}$$

$$Z = R + jX \tag{A.2}$$

### Equivalent $\pi$ model

The equivalent $\pi$ model is more accurate for longer cables because it utilises distributed parameters. Voltages and currents can be found at any given place along the cables length. The implementation of the distributed parameters can be seen in figure A.2. [1]

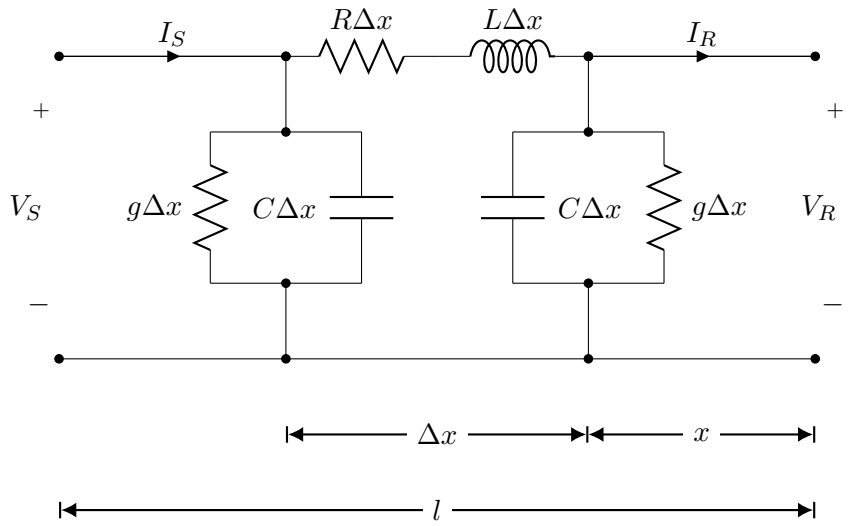


**Figure A.2:** Equivalent $\pi$ model

By implementing the propagation constant, $\gamma$ which is calculated by equation A.3, the parameters of the model can be obtained with equations A.4 through A.7.

$$\gamma = \sqrt{(r + j\omega L)(g + j\omega C)} \tag{A.3}$$

$$Z' = Z\frac{sinh\gamma l}{\gamma l} \tag{A.4}$$

$$\frac{Y'}{2} = \frac{Y}{2}\frac{tanh\gamma l/2}{\gamma l/2} \tag{A.5}$$

$$V_S = (1 + \frac{Z'Y'}{2})V_R + Z'I_R \tag{A.6}$$

$$I_S = Y'(1 + \frac{Z'Y'}{4})V_r + (1 + \frac{Z'Y'}{2})I_R \tag{A.7}$$

In order to properly represent several frequency ranges, both the $\pi$-models need to have multiple sections coupled together, which will affect computational time.

### Bergeron model

A further development of the $\pi$-models is the Bergeron model. Power losses utilise a lumped resistance, but the distributed capacitances and inductances are accurately represented. The model is accurate for specific frequencies, but is not suitable for harmonic studies as it misses some of the frequency responses. The standard Bergeron model cannot be used for lossy lines since both the propagation constant and the characteristic impedance are frequency dependent, but by making the series resistances lumped at the ends and in the middle and assuming the shunt conductances negligible as seen in figure A.3, the cable can be modelled as two separate Bergeron equivalent models. [29]

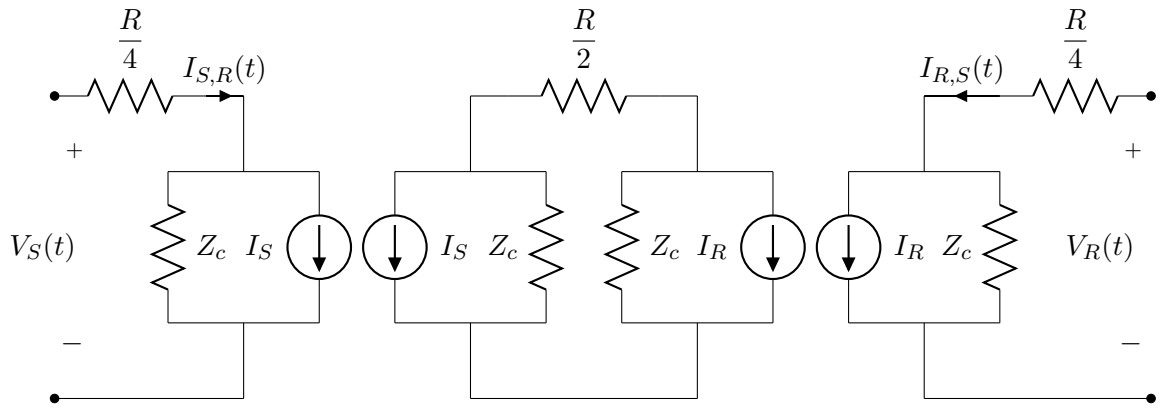


**Figure A.3:** Bergeron model with lumped resistance

The lumped resistance model in figure A.1 can be collected to a two port format seen in figure A.4.

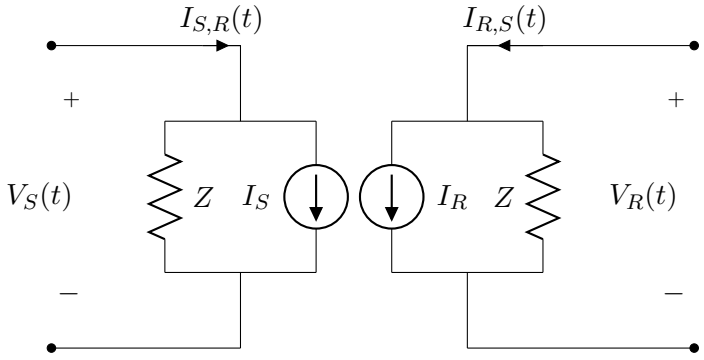


**Figure A.4:** Time domain Bergeron model

$I_S$ and $I_R$ are shortened for $I_S(t-\tau)$ and $I_R(t-\tau)$ respectively, where $\tau$ is the travel time calculated as equation A.8 where $l$ is length and $v$ is speed.

$$\tau = \frac{l}{v} = l\sqrt{LC} \tag{A.8}$$

The collected impedance at each end is calculated as equation A.9.

$$Z = Z_0 + \frac{R}{4} \tag{A.9}$$

The currents at each end are then represented by equations A.10 and A.11.

$$\begin{aligned} I_S(t-\tau) = &\left(\frac{1+H}{2}\right)\left(-\frac{1}{Z}V_R(t-\tau) - I_{R,S}(t-\tau)\right) \\ &+\left(\frac{1+H}{2}\right)\left(-\frac{1}{Z}V_S(t-\tau) - I_{S,R}(t-\tau)\right) \end{aligned} \tag{A.10}$$

$$\begin{aligned} I_R(t-\tau) = &\left(\frac{1+H}{2}\right)\left(-\frac{1}{Z}V_S(t-\tau) - I_{S,R}(t-\tau)\right) \\ &+\left(\frac{1+H}{2}\right)\left(-\frac{1}{Z}V_R(t-\tau) - I_{R,S}(t-\tau)\right) \end{aligned} \tag{A.11}$$

H represents equation A.12.

$$H = \frac{Z_C - \frac{R}{4}}{Z_C + \frac{R}{4}} \tag{A.12}$$

The Bergeron model can be compared to using several $\pi$-models together, as it can accurately represent components at the fundamental frequency. It is not recommended to use for multiple frequency studies.

### Frequency dependent in mode

A constant transformation matrix is required for the frequency dependent in mode model, which represents all the frequency dependencies of all the parameters. [30]

The sending and receiving end voltages can be calculated by equations A.13 and A.14, where $v_k(t-\tau)$ and $v_m(t-\tau)$ are the backward travelling waves functions which are based on the historical values of the forward travelling waves, given that the time step $\delta t < \tau$. [31]

$$v_k(t) = Z_{eq} i_k(t) + v_k(t-\tau) \tag{A.13}$$

$$v_m(t) = Z_{eq} i_m(t) + v_m(t-\tau) \tag{A.14}$$

A representation of the model can be seen in figure A.5.

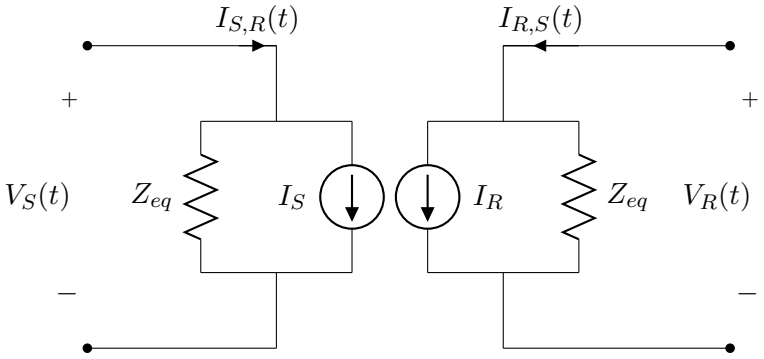


**Figure A.5:** Frequency dependent in mode model

The frequency dependent in mode model proved to unreliable when dealing with unbalanced systems, AC/DC systems included. [31]

### Frequency dependent in phase

The in phase model has the benefit of formulating the model in the phase domain directly and thereby removing the problems of the frequency dependent transformation matrix. It is the most accurate model and can be used for all transmission configurations and unbalanced cable geometries. [30] A representation of the model can be seen in figure A.6. [31]

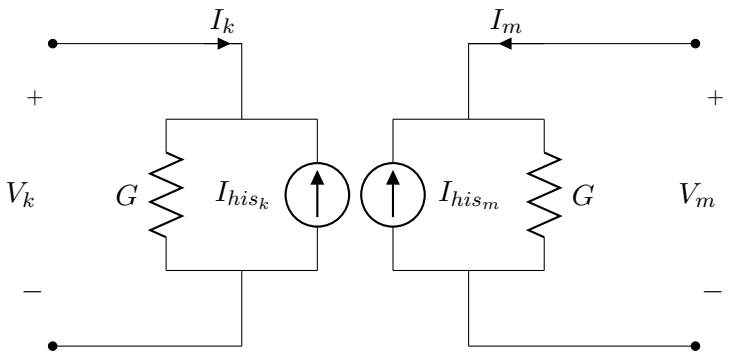


**Figure A.6:** Frequency dependent in mode model

$I_{his_k}$ $I_{his_m}$ represent the history injections by the current sources and are updated for each time step by the given node voltages $V_k$ and $V_m$. The specific steps which are calculated by PSCAD are given as equations A.15 through A.18.

$$I_k(n) = GV_k(n) - I_{his_k}(n) \tag{A.15}$$

$$I_{kr}(n) = I_k(n) - I_k i(n) \tag{A.16}$$

$$I_{ki}(n+1) = H * I_{mr}(t-\tau) \tag{A.17}$$

$$I_{his_k}(n+1) = Y'_C * V_k(n) - 2I_{ki}(n+1) \tag{A.18}$$

$i$ is incident waves, $r$ is reflected waves and $*$ is a convoluted integral. $H$ is the propagation function matrix $e^{-\sqrt{ZY}l}$ and $Y_C$ is the characteristic admittance matrix $Z^{-1}\sqrt{ZY}$.

**Cable models - conclusion**

Considering the different cable models available for implementation in PSCAD it is seen that if conducting transient analysis, the frequency dependent phase models are superior since they accurately represent components at every frequency. Deciding between the two models can be done by reading about the frequency dependent models described in the PSCAD literature, this is verbatim: *"The Frequency Dependent (Phase) Model is the most numerically accurate and robust line/cable model available anywhere in the world!"* [31].

## A.2 Material Parameters used in Calculations

Table A.1 presents the material constant values utilized for the calculation of electric stress in the insulating layers (main insulation, oversheath). a is the temperature coefficient of the insulations electrical conductivity, b is the electric field coefficient of the electrical conductivity of the insulation. In reality, the coefficients a and b are not constant but depend on temperature and electric field strength. To not overcomplicate calculations, they are assumed constant here. As the maximum electric stress is higher for high values of a and low values of b, they were chosen accordingly to ensure that the insulation will not be to thin [20].

| | material | dielectric strength [kV/mm] | a | b |
|---|---|---|---|---|
| insulation | XLPE | 21 [21] | 0.084 | 0.0645 |
| oversheath | PE [27] | 18.9 | 0.115 | 0.0128 |

**Table A.1:** Material constants for electric stress calculations

Table A.2 summarizes the material constants of the conducting layers required temperature calculations [27].

| | material | $\rho_{20°C}$ $[\Omega m]$ | $\alpha$ $[K^{-1}]$ | $c_p$ $[Jkg^{-1}K^{-1}]$ | $m$ $[kgm^{-3}]$ |
|---|---|---|---|---|---|
| conductor | copper | $1.68 \times 10^{-8}$ | 0.0039 | 393 | 8930 |
| sheath | lead | $2.20 \times 10^{-7}$ | 0.0039 | 129 | 11340 |
| armour | steal | $1.80 \times 10^{-7}$ | 0.0030 | 466 | 7850 |

**Table A.2:** Material constants for transient heating calculations

Furthermore the thermal resistivity $\rho_T$ is

- 3.5 $\frac{Km}{W}$ for PE and XLPE
- 0.9 $\frac{Km}{W}$ for the seabed soil

## A.3 Summary of DS IEC 60502

The Danish standard DS IEC 60502-2 covers "Power cables with extruded insulation and their accessories for rated voltages from 1 kV (Um = 1,2 kV) up to 30 kV (Um = 36 kV) – Part 2: Cables for rated voltages from 6 kV (Um = 7,2 kV) up to 30 kV (Um = 36 kV)". The standard within its scope "specifies the construction, dimensions and test requirements of power cables with extruded solid insulation from 6 kV up to 30 kV for fixed installations" [22].

The specifications given in the standard that are of importance for and utilized in this project are summarized subsequently.

The cable has to comprise following layers above the conductor:
insulation, screen, sheath, separation sheath, armour, oversheath.

Maximum conductor temperature for chosen insulation and sheathing materials in °C:

| layer | material | normal operation | short circuit (up to 5 s) |
|---|---|---|---|
| insulation | XLPE | 90 | 250 |
| separation sheath | PE | 90 | - |
| oversheath | PE | 90 | - |

Screen

- The conductor has to be screened by a semiconductor layer.

- The insulation has to be screened by a semiconductor layer and a metal layer, which may be the sheath.
- The thickness of the semiconductor layers is 0.75 mm each.

Sheath

- The sheath material is lead or a lead alloy.
- Its nominal thickness $r_{pb-sheath}$ in $mm$ is calculated according to
  $r_{pb-sheath} = 0.03 * D_g + 0.7$ in steps of 0.1,
  with $r_{pb-sheath} \geq 1.2$ and $D_g$ being the fictitious diameter under the sheath.

Separation Sheath

- Its nominal thickness $r_{sep-sheath}$ in $mm$ is calculated according to
  $r_{sep-sheath} = 0.02 * D_u + 0.6$ rounded off to steps of 0.1,
  with $r_{sep-sheath} \geq 1.0$ and $D_u$ being the fictitious diameter over the sheath.

Armour

- The armour is made of round steel wires.
- Their nominal diameter $t_A$ is 2.5 mm for a fictitious diameter $D_s$ between 35 mm and 60 mm under the armour, which is the case for all regarded cables.

Oversheath

- Its nominal thickness $r_{outer-sheath}$ in $mm$ is calculated according to
  $r_{outer-sheath} = 0.0035 * D + 1$ rounded off to steps of 0.1,
  with $r_{outer-sheath} \geq 1.4$ and $D$ being the fictitious diameter over the armour.

Fictitious diameters in $mm$ are calculated as

- $D_g = D_c + 2r_{ins} + 3.0$ with conductor diameter $D_c$ rounded off to steps of 0.1 and insulation thickness $r_{ins}$
- $D_u = D_g + 2r_{pb-sheath}$
- $D_s = D_u + 2r_{sep-sheath}$
- $D = D_s + 2t_A$

## A.4 Sizing Algorithm

As could be seen in chapter 3.2, the size of cable layers, especially conductor and insulation, depend on each other. Knowledge of the conductor size is needed in order to determine the insulation thickness. However, the conductors ampacity and hence the thermal design depend on heat transfer through the insulation. Therefore an iterative procedure is required to achieve appropriate dimensioning of the MVDC cable. It is presented in figure A.7.

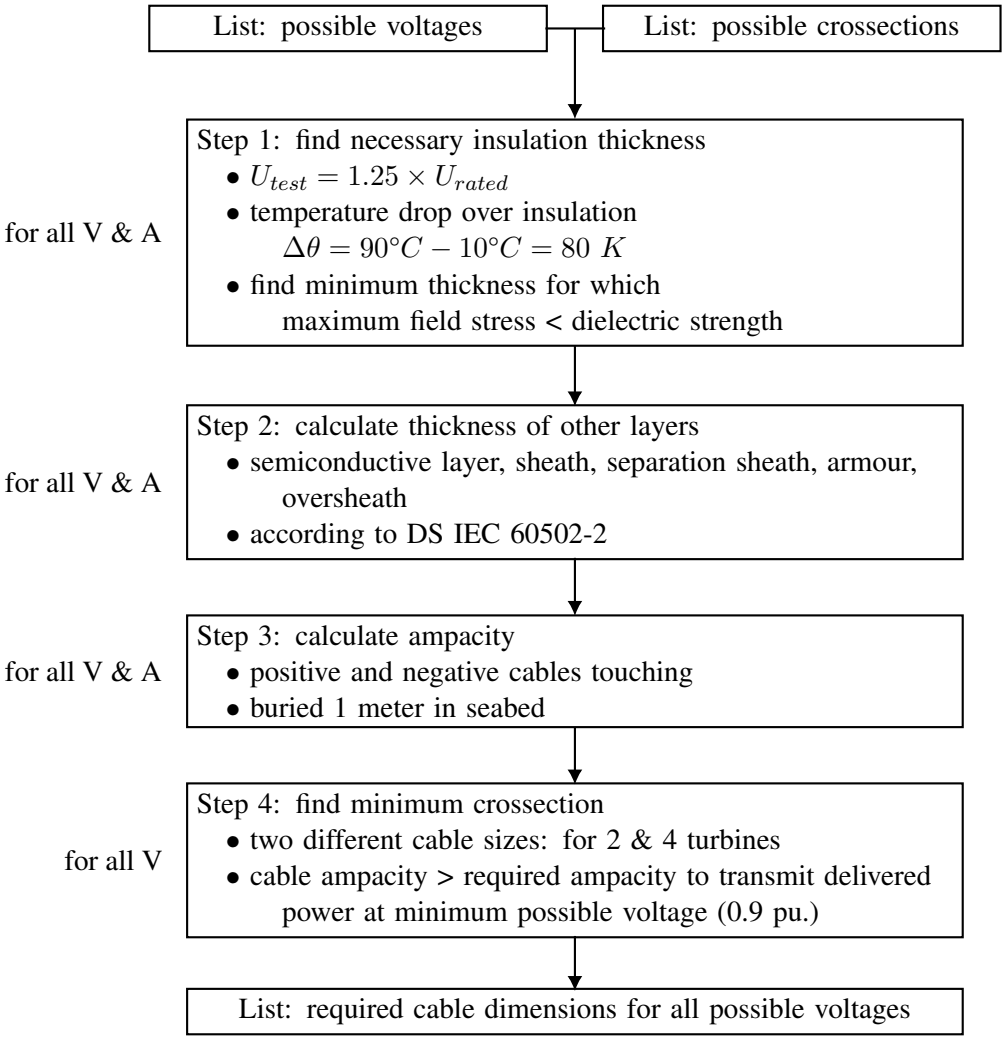


**Figure A.7:** Algorithm for dimensioning of the MVDC cable

In the figure it can be seen that the dimensioning procedure is based on a preselection of possible voltage levels and conductor cross sections. This selection can be made with respect to equipment available on the market, restrictions in the production process or according to economic criteria, or it can be replaced by an optimization. For this project, the values presented in table A.3 have been considered.

| **A** [$mm^2$] | 50 | 75 | 100 | 125 | 150 | 175 | 200 | 225 | 250 | 300 |
|---|---|---|---|---|---|---|---|---|---|---|
| | 400 | 500 | 600 | 700 | 800 | 900 | 1000 | 1100 | 1200 | |

| **V** [$\pm kV$] | 10 | 12 | 14 | 16 | 18 | 20 | 22 | 24 |
|---|---|---|---|---|---|---|---|---|
| | 26 | 28 | 30 | 32 | 36 | 40 | 50 | 60 |

**Table A.3:** Possible voltage levels (V) and conductor cross sections (A) considered for the cable dimensioning

In step 1 of the algorithm, the required insulation thickness is determined for every combination of possible voltage levels and conductor cross sections based on the theory presented in chapter 3.2.2. To ensure that the insulation is able to withstand voltages and electric stresses during all operating conditions that are likely to occur, the dimensioning is executed with respect to maximum possible temperature drop over the insulation and 1.25 times the rated pole to pole voltage. Assuming an ambient temperature of 10°C and considering the maximum allowable steady state operation temperature of 90°C this corresponds to a difference of 80 K across the insulation. The voltage is chosen considering the possibility to operate the grid at up to 1.1 p.u. in normal operation, the case of a phase to ground voltage close to the cable, where the opposite phase will experience a fast rise in potential to the phase to phase voltage level and a safety margin.
Considering all these facts, the insulation thickness is increased stepwise until the peak calculated stresses are smaller than the dielectric strengths of the material.

In step 2, the thickness of all other layers are determined according to the procedure in appendix A.3 for all combinations of V and A.

Subsequently, in step 3, the ampacity for all cable designs is determined following the theory explained in chapter 3.2.1. It is assumed that positive and negative pole of each cable section are buried one meter deep in the seabed and that both cables are touching.

Finally, in step four the suitable cable design for each voltage level is selected. The cables are supposed to feature as few material as possible, therefore two different cable sizes are chosen for every voltage level. The bigger design is utilised for the cable sections that have to transmit the power of three or four turbine towards the substation, i.e. the cables closest to it. The cables further upstream, which have to carry current from only one or two turbines can have a smaller design.
The designs are chosen by comparing the ampacity of all possible cable designs from step 3 to the maximum required steady state ampacity $I_A$, which is defined by the rated turbine power and the minimum allowed system voltage according to the relation

$$I_A = \frac{number\ of\ turbines \cdot P_{rated}}{0.9 \cdot U_{rated}}. \tag{A.19}$$

Finally, the procedure results in a list of selected cable designs depending on the system voltage level. Results are presented in chapter 3.2.4.

## A.5 DC Load Flow Simulation

### A.5.1 Load Flow Algorithm

Load flow simulations are calculated following the Gauss-Siedel method (see e.g. [32]). Since a DC system is regarded, only active power flows occur and voltage drops in the load flow calculation depend solely on the conductor resistances. Subsequently, the load adapted Gauss-Siedel algorithm is explained.

**Step 1: Specification of System Data**

The system consists of 33 buses, 32 turbine buses and 1 substation bus, which is regarded as the slack bus. The overall topology is presented in chapter 3.1.1. Each turbine has a rated power of 8 MW which it can feed into the system.

The distances between these buses, representing the length of the cable sections, are summarized in table A.4. Resulting from chapter 3.2 two different cable dimensions are chosen for the system. The letters in brackets shows which cable sections feature the bigger (B) or smaller (S) cable design respectively.

| | **Feeder** | | | | | | | |
|---|---|---|---|---|---|---|---|---|
| | 1 | 2 | 3 | 4 | 5 | 6 | 7 | 8 |
| A | 3.5 (B) | 2.2 (B) | 1.4 (B) | 1.9 (B) | 1.3 (B) | 0.6 (B) | 3.1 (B) | 1.7 (B) |
| B | 1.1 (B) | 1.9 (B) | 2.3 (B) | 1.3 (S) | 1.8 (B) | 1.8 (B) | 1.2 (B) | 1.2 (S) |
| C | 1.2 (S) | 2.4 (S) | 1.3 (S) | 1.4 (S) | 1.1 (S) | 2.9 (S) | 1.2 (S) | 1.2 (S) |
| D | 1.2 (S) | 1.0 (S) | 1.1 (S) | 1.3 (S) | 1.3 (S) | 1.7 (S) | 1.2 (S) | 1.8 (S) |

**Table A.4:** Cable lengths in km and cross section (in brackets) of the WPP cable sections

**Step 2: Calculation of Admittance Matrix**

Since a DC system is regarded, only active power flows occur and voltage drops depend solely on the conductor resistances $R_{cable}$, which can be calculated as

$$R_{conductor} = 2\frac{\rho_\theta}{A}l. \tag{A.20}$$

In equation A.20 $l$ is the cable length between the nodes, $A$ is the conductor cross section and $\rho_\theta$ is the specific resistivity of the conductor material at temperature $\theta$, which can be calculated as in equation A.21. The factor 2 comes from the fact that power is transferred using both positive and negative phase, hence the absolute conductor length is twice the distance between two nodes.

$$\rho_\theta = \rho_{20°C} \cdot (1 + \alpha\,(\theta - 20°C))\,. \tag{A.21}$$

In equation A.21 $\rho_{20°C,copper} = 0.0168\ \Omega mm^2 m^{-1}$ and the thermal coefficient $\alpha_{copper} = 0.0039\ K^{-1}$ for copper.

Consequently the $33 \times 33$ admittance matrix $Y$ can be calculated. The entries $Y_{ij}$ between two buses i and j are calculated by equation A.22 where $R_{ij}$ is the resistance $R_{conductor}$ between these buses. The diagonal elements $Y_{ii}$ of the matrix are the negative sum of all adjacent cables to bus i, as shown

in equation A.23

$$Y_{ij} = Y_{ji} = -\frac{1}{R}. \tag{A.22}$$

$$Y_{ii} = -\sum_{j=1,\, j\neq i}^{33} Y_{ji} \tag{A.23}$$

**Step 3: Initialisation of bus voltages at iteration 0**

$$V_i^{(0)} = 1 \qquad\qquad for\ i = 1...33 \tag{A.24}$$

**Step 4: Update bus voltages for buses 2 to 33 (bus 1 is the slack bus)**

In $k^{th}$ iteration:

$$V_i^{(k)} = \frac{1}{Y_{ii}} \cdot \left( \frac{P_i}{V_i^{(k-1)}} - \sum_{j=1}^{i-1} Y_{ij} V_j^{(k)} - \sum_{j=i+1}^{33} Y_{ij} V_j^{(k-1)} \right) \tag{A.25}$$

In equation A.25 $P_i$ is the power that is fed in at bus i by its turbine.

After all bus voltages have been updated, the difference between the results in the $k^{th}$ and $(k-1)^{th}$ iteration are compared to a maximum tolerable error $\varepsilon_{error}$:

$$\left| V_i^{(k)} - V_i^{(k-1)} \right| \leq \varepsilon_{error} \tag{A.26}$$

Step 4 is repeated until equation A.26 becomes true for all buses.

**Step 5: Calculation of slack bus power, line current flows, power flows and losses**

The slack bus power, which is negative when the WPP exports power, is defined as

$$P_1 = V_1 \left( V_1 Y_{1,1} + \sum_{j=2}^{33} Y_{1,j} V_j \right) \tag{A.27}$$

The line current flows from bus i to j are calculated as

$$I_{ij} = -Y_{ij} \left( V_i - V_j \right) \tag{A.28}$$

Corresponding to this, the line flows from bus i to j are calculated as

$$P_{ij} = V_i I_{ij} \tag{A.29}$$

Finally the line losses are found to be

$$P_{loss,ij} = P_{ij} + P_{ji} \tag{A.30}$$

### A.5.2 Consideration of Cable Heating

Current flow through the cable causes energy dissipation, leading to heating of the cable. This mechanism is explained in more detail in chapter 3.2.1. Rearranging equation 3.9 allows the calculation of conductor temperature $\Theta_c$ for a given resistance per unit length, current and ambient temperature $\Theta_{amb}$.

$$\Theta_c = I^2 R'(T_1 + T_2 + T_3 + T_4) + \Theta_{amb} \tag{A.31}$$

Equation A.31 and the description of the load flow algorithm show that the magnitudes of conductor temperature, resistance and current flow through the conductor resulting from the load flow are interdependent. Therefore, the load flow calculation with consideration of conductor temperatures has to be solved iteratively. The method is shown in picture A.8.

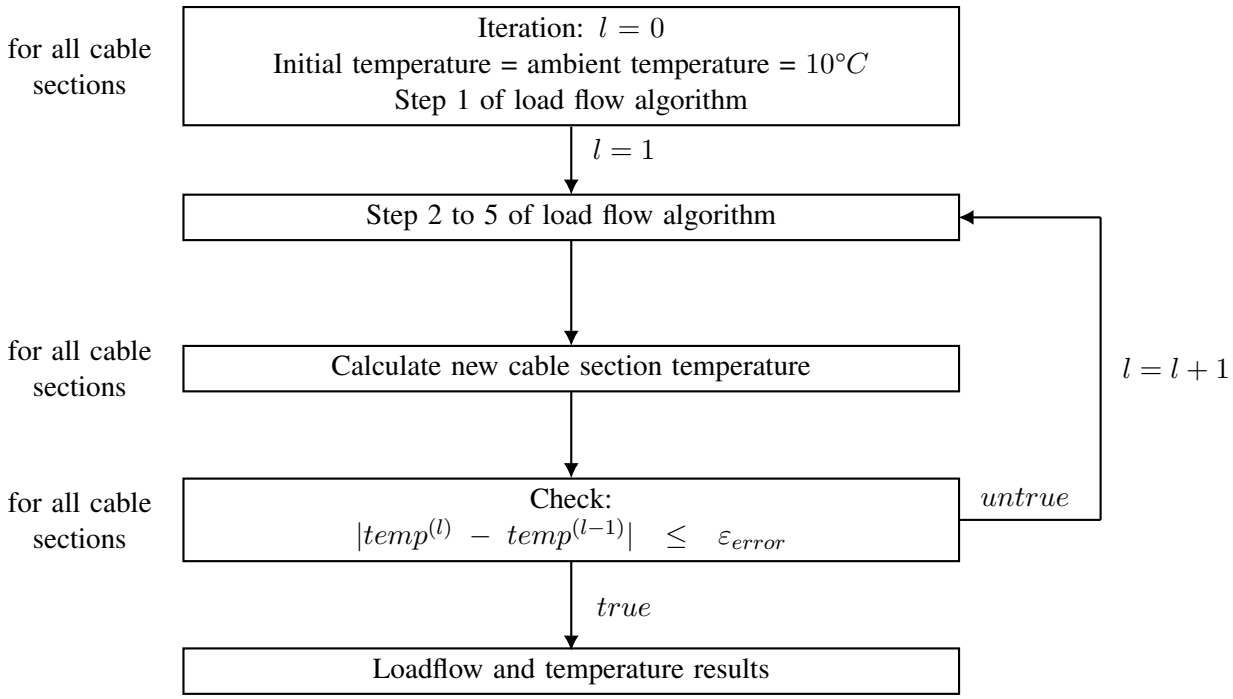


**Figure A.8:** Algorithm for load flow including conductor heating

Initially, it is assumed that the cables operate at ambient temperature, which is assumed to be 10°C throughout the year. Seasonal changes and long term heating effects due to cable operation are not regarded. With this information a load flow is conducted in the first iteration l=1. Next, the cable temperatures for every cable section are calculated based on equation A.31 and on the current flowing through them according to the load flow results. Afterwards, the temperatures are compared with the results from the previous iteration. If the error is smaller than a minimum allowable tolerance $\varepsilon_{error}$, the calculations are finished. Otherwise the procedure is repeated from step 2 of the load flow algorithm, where the admittance matrix of the system is calculated with the newly obtained temperature values, until the temperatures converge.

## A.6 Temperatures of conductor, sheath and armour

Steady state temperatures of the cable's conductors, sheaths and armours are presented in tables A.5 to A.13, given that all turbines feed in rated power.

| | **Feeder** | | | | | | | |
|---|---|---|---|---|---|---|---|---|
| | 1 | 2 | 3 | 4 | 5 | 6 | 7 | 8 |
| A | 82.2 | 82.2 | 82.9 | 83.1 | 83.5 | 82.7 | 82.4 | 83.2 |
| B | 45.9 | 45.8 | 46.1 | 83.1 | 46.5 | 45.9 | 45.9 | 83.3 |
| C | 82.1 | 81.6 | 82.7 | 24.9 | 25.1 | 81.8 | 82.3 | 24.9 |
| D | 24.7 | 24.6 | 24.8 | 25.1 | 25.0 | 24.7 | 24.8 | 25.1 |

**Table A.5:** Steady state conductor temperatures when $U_{sub} = 0.9\ p.u.$ in °C

| | **Feeder** | | | | | | | |
|---|---|---|---|---|---|---|---|---|
| | 1 | 2 | 3 | 4 | 5 | 6 | 7 | 8 |
| A | 59.0 | 59.0 | 59.5 | 59.6 | 59.9 | 59.3 | 59.1 | 59.6 |
| B | 34.3 | 34.2 | 34.5 | 55.7 | 34.7 | 34.4 | 34.4 | 55.9 |
| C | 55.1 | 54.7 | 55.4 | 19.3 | 19.4 | 54.9 | 55.2 | 19.3 |
| D | 19.2 | 19.2 | 19.3 | 19.4 | 19.4 | 19.2 | 19.2 | 19.4 |

**Table A.6:** Steady state sheath temperatures when $U_{sub} = 0.9\ p.u.$ in °C

| | **Feeder** | | | | | | | |
|---|---|---|---|---|---|---|---|---|
| | 1 | 2 | 3 | 4 | 5 | 6 | 7 | 8 |
| A | 57.5 | 57.5 | 58.0 | 58.1 | 58.4 | 57.8 | 57.6 | 58.2 |
| B | 33.6 | 33.5 | 33.8 | 54.4 | 34.0 | 33.6 | 33.6 | 54.5 |
| C | 53.8 | 53.4 | 54.1 | 19.0 | 19.1 | 53.6 | 53.9 | 19.1 |
| D | 18.9 | 18.9 | 19.0 | 19.2 | 19.1 | 18.9 | 19.0 | 19.1 |

**Table A.7:** Steady state armour temperatures when $U_{sub} = 0.9\ p.u.$ in °C

| | **Feeder** | | | | | | | |
|---|---|---|---|---|---|---|---|---|
| | 1 | 2 | 3 | 4 | 5 | 6 | 7 | 8 |
| A | 65.8 | 65.8 | 66.2 | 66.3 | 66.6 | 66.1 | 65.9 | 66.4 |
| B | 38.5 | 38.4 | 38.6 | 66.4 | 38.8 | 38.5 | 38.5 | 66.5 |
| C | 65.9 | 65.5 | 66.2 | 22.0 | 22.1 | 65.7 | 65.9 | 22.0 |
| D | 21.9 | 21.8 | 22.0 | 22.1 | 22.1 | 21.9 | 21.9 | 22.1 |

**Table A.8:** Steady state conductor temperatures when $U_{sub} = 1\ p.u.$ in °C

| | **Feeder** | | | | | | | |
|---|---|---|---|---|---|---|---|---|
| | 1 | 2 | 3 | 4 | 5 | 6 | 7 | 8 |
| A | 47.9 | 47.8 | 48.1 | 48.2 | 48.3 | 48.0 | 47.9 | 48.2 |
| B | 29.3 | 29.3 | 29.4 | 45.3 | 29.6 | 29.3 | 29.3 | 45.4 |
| C | 44.9 | 44.7 | 45.1 | 17.5 | 17.6 | 44.8 | 45.0 | 17.5 |
| D | 17.4 | 17.4 | 17.5 | 17.6 | 17.6 | 17.4 | 17.5 | 17.6 |

**Table A.9:** Steady state sheath temperatures when $U_{sub} = 1\ p.u.$ in °C

| | **Feeder** | | | | | | | |
|---|---|---|---|---|---|---|---|---|
| | 1 | 2 | 3 | 4 | 5 | 6 | 7 | 8 |
| A | 46.7 | 46.7 | 47.0 | 47.1 | 47.2 | 46.9 | 46.8 | 47.1 |
| B | 28.7 | 28.7 | 28.8 | 44.2 | 29.0 | 28.8 | 28.8 | 44.3 |
| C | 43.9 | 43.7 | 44.1 | 17.3 | 17.3 | 43.8 | 44.0 | 17.3 |
| D | 17.2 | 17.2 | 17.3 | 17.4 | 17.3 | 17.2 | 17.2 | 17.4 |

**Table A.10:** Steady state armour temperatures when $U_{sub} = 1\ p.u.$ in °C

| | Feeder | | | | | | | |
|---|---|---|---|---|---|---|---|---|
| | 1 | 2 | 3 | 4 | 5 | 6 | 7 | 8 |
| A | 54.6 | 54.6 | 54.8 | 54.9 | 55.1 | 54.8 | 54.7 | 54.9 |
| B | 33.2 | 33.1 | 33.3 | 55.0 | 33.4 | 33.2 | 33.2 | 55.1 |
| C | 54.7 | 54.5 | 54.9 | 19.9 | 19.9 | 54.6 | 54.7 | 19.9 |
| D | 19.8 | 19.8 | 19.9 | 20. | 0 19.9 | 19.8 | 19.8 | 19.9 |

**Table A.11:** Steady state conductor temperatures when $U_{sub} = 1.1\ p.u.$ in °C

| | Feeder | | | | | | | |
|---|---|---|---|---|---|---|---|---|
| | 1 | 2 | 3 | 4 | 5 | 6 | 7 | 8 |
| A | 40.2 | 40.2 | 40.4 | 40.5 | 40.5 | 40.4 | 40.3 | 40.5 |
| B | 25.7 | 25.7 | 25.8 | 38.2 | 25.9 | 25.7 | 25.7 | 38.2 |
| C | 37.9 | 37.8 | 38.1 | 16.2 | 16.2 | 37.9 | 38.0 | 16.2 |
| D | 16.1 | 16.1 | 16.2 | 16.2 | 16.2 | 16.1 | 16.1 | 16.2 |

**Table A.12:** Steady state sheath temperatures when $U_{sub} = 1.1\ p.u.$ in °C

| | Feeder | | | | | | | |
|---|---|---|---|---|---|---|---|---|
| | 1 | 2 | 3 | 4 | 5 | 6 | 7 | 8 |
| A | 39.3 | 39.3 | 39.5 | 39.5 | 39.6 | 39.5 | 39.4 | 39.6 |
| B | 25.3 | 25.2 | 25.3 | 37.3 | 25.4 | 25.3 | 25.3 | 37.4 |
| C | 37.1 | 37.0 | 37.2 | 16.0 | 16.0 | 37.0 | 37.2 | 16.0 |
| D | 16.0 | 15.9 | 16.0 | 16.0 | 16.0 | 15.9 | 16.0 | 16.0 |

**Table A.13:** Steady state armour temperatures when $U_{sub} = 1.1\ p.u.$ in °C

## A.7 PSCAD

In this section the full PSCAD model will be presented. Five figures containing the top layer, radials 1, 2, 3 and 8 will be shown and its functions explained.

The top layer, or main, as it is referred to in PSCAD is shown in figure A.9. The substation on the left is modelled as a voltage source and its filter is seen just right of it. There are also two diodes and switches marked ENRG, which are only used to import power to energise the system quickly to shorten simulation time. During normal simulations the switches are off and the diodes ensure that no power is imported from shore. Currents are measured before and after the substation filter to be able to see when power is exported and when it is charging the filter capacitors. Two measurements are also placed to measure the substation voltage after the filter. Currents are measured out of each radial, where radials 3-8 are marked with an L to indicate that they are lumped.

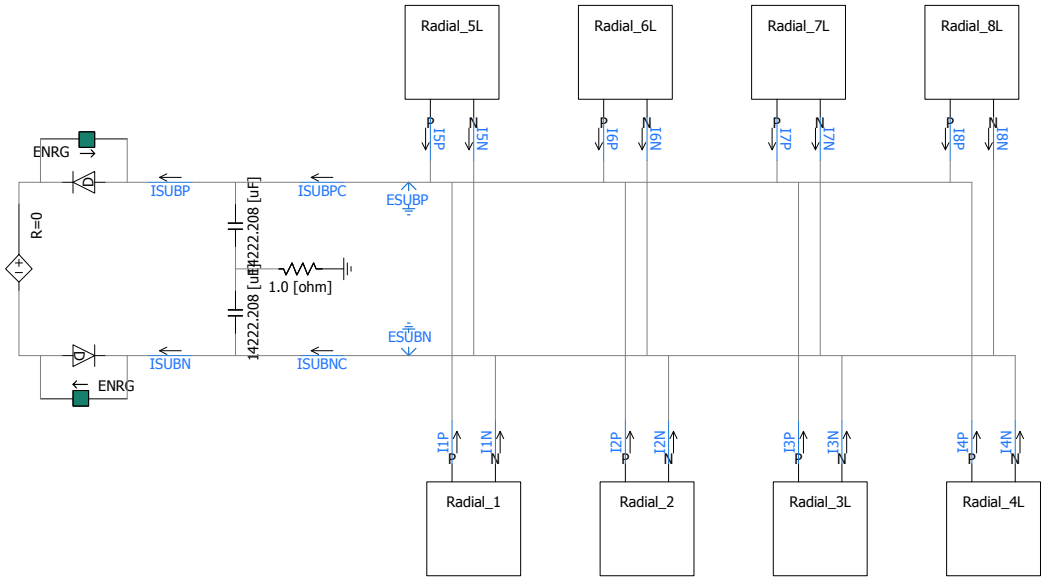


**Figure A.9:** Top layer of PSCAD model

Figure A.10 shows the fully modelled radial 1 where current and voltage is measured at each turbine. The current source together with the capacitors represents a turbine and its converter. Furthermore there are measurements of current and voltage at the sheath and armour at the beginning and the end of the radial. The switches marked BRK are used to control the turbines ability to supply current or not.

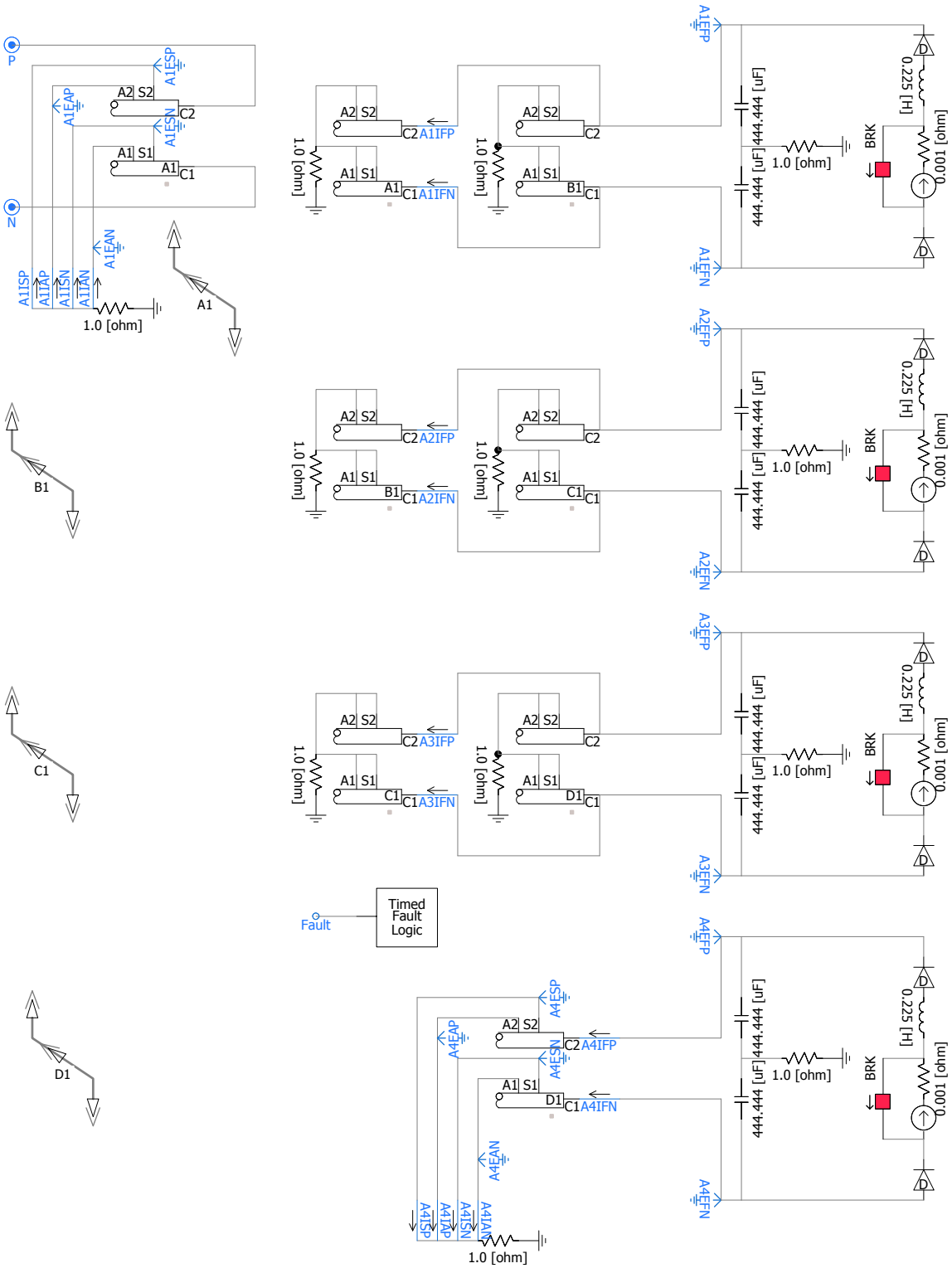


**Figure A.10:** Radial 1 of PSCAD model

Radial 2 is depicted in figure A.11, which is also a full radial with currents and voltages measured for each turbine. This radial was kept full in order to be able to compare two full radials, and also how a full radial compares to a lumped one during non-steady state conditions. The last turbine has some extra current measurements which help in identifying the contributions from the different components and also to see when the capacitors charge and discharge.

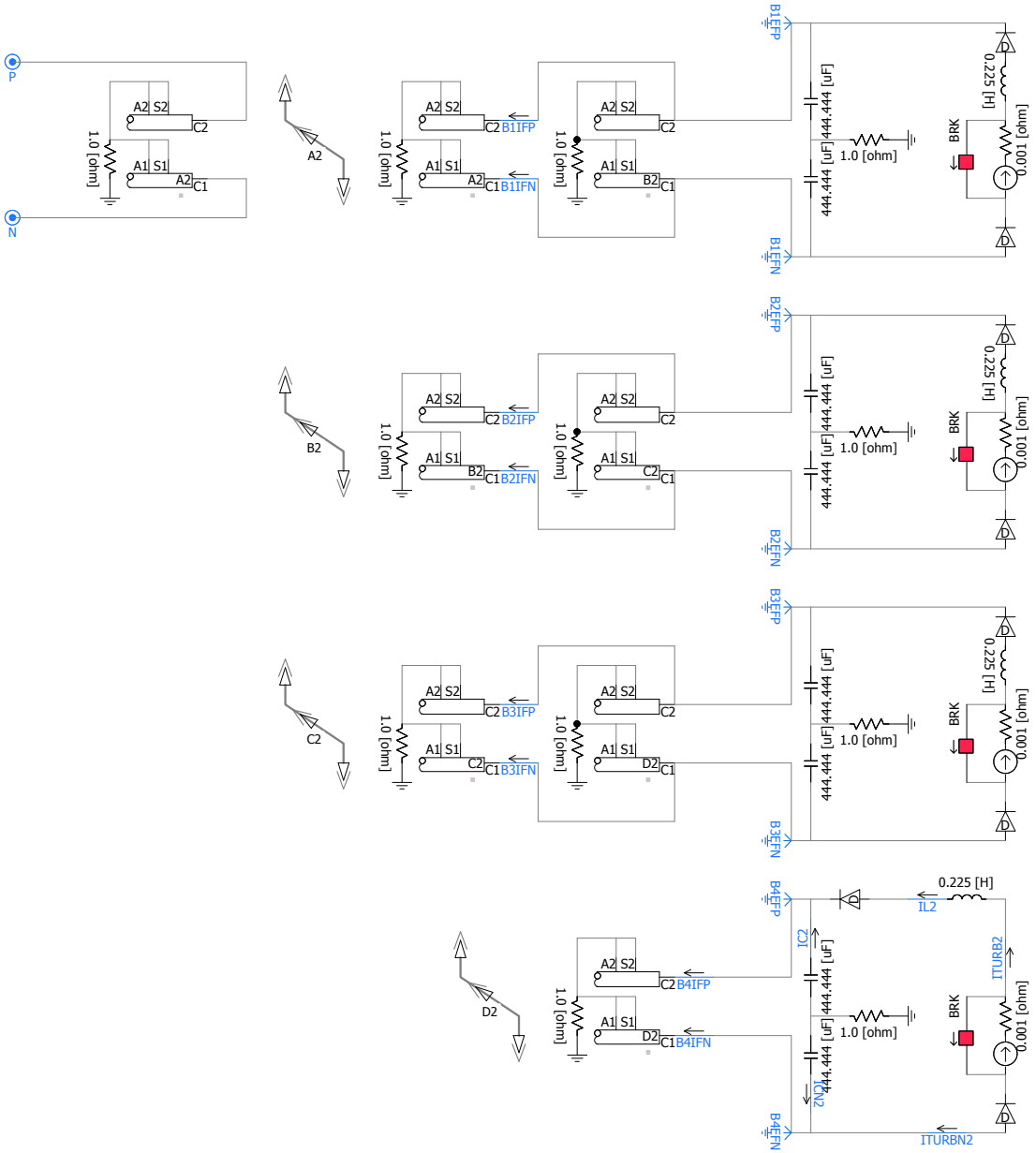


**Figure A.11:** Radial 2 of PSCAD model

Radial 3 is shown in figure A.12 and is a lumped radial. The description of the lumping procedure is presented after this section. Voltage measurements are at the turbine and the current from the radial is measured in the top layer as shown in figure A.9. Radials 3-7 have the same layout.

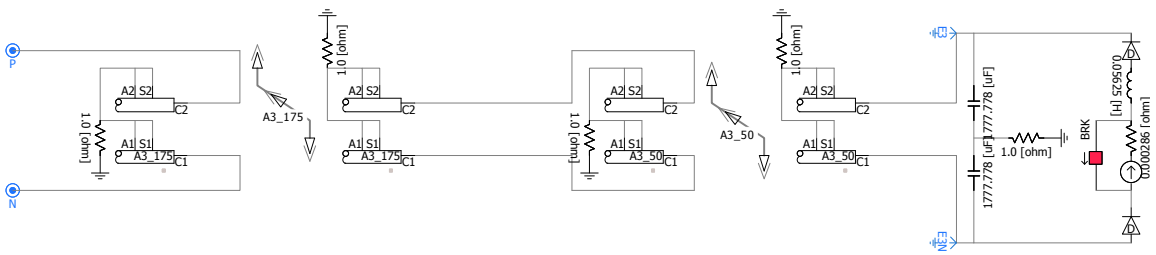


**Figure A.12:** Radial 3 of PSCAD model

The final figure is A.13 which is of radial 8. This is included since it contains the same extra current measurements as radial 2, seen in figure A.11. These were included to be able to compare a full radial with a lumped one more in detail.

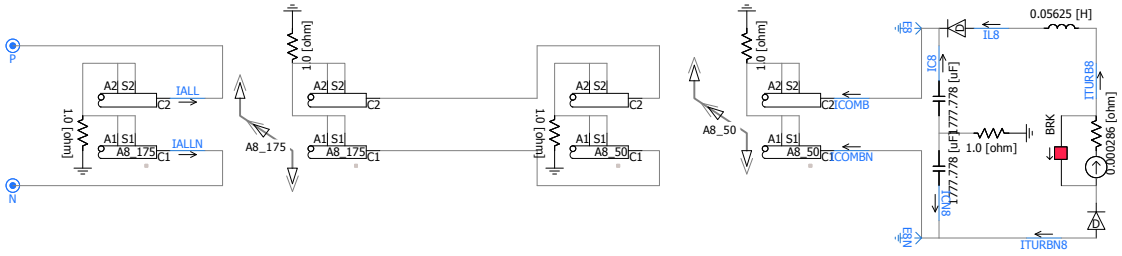


**Figure A.13:** Radial 8 of PSCAD model

### A.7.1 Lumping

Six of the eight radials have been lumped and the method and validation of the lumping will be presented here. In order to lump a radial, there are four main components which need consideration:

- **Cables** - There are four cables in a radial, one for each turbine, and they are lumped into two cables, 50 mm$^2$ and 175 mm$^2$. Labelling them from the substation as A,B,C,D the lengths are calculated as follows:

$$Cable_{175} = 100\% \cdot A + 75\% \cdot B$$

$$Cable_{50} = 50\% \cdot C + 25\% \cdot D$$

- **Capacitors** - Since the capacitors are in parallel they are added up:

$$C_{lumped} = 4 \cdot C$$

- **Inductors** - The inductors are in series and are lumped as:

$$L_{lumped} = \frac{1}{\frac{1}{L} + \frac{1}{L} + \frac{1}{L} + \frac{1}{L}}$$

- **Turbines** - The turbines are current sources in series so these are also added up:

$$Turb_{lumped} = 4 \cdot Turb$$

A lumped radial was shown in figure A.12. After lumping the radials it is important to see how they compare to the originals. An off/on simulation has been done where currents are measured out of the radials and the inductor and capacitor currents of radials 2 & 8

The first graph in figure A.14 shows that the currents at the different radials compare closely to each other. The second and third graph have different amplitudes because the measurements at radial 2 are for a single turbine, whereas radial 8 is lumped and as such has four times more current, but it is seen that the transients from turning the turbines off and on again are very similar, meaning the selected lumping method can be considered sufficient. It should be mentioned that when lumping in such a manner there will always be differences from the original system.

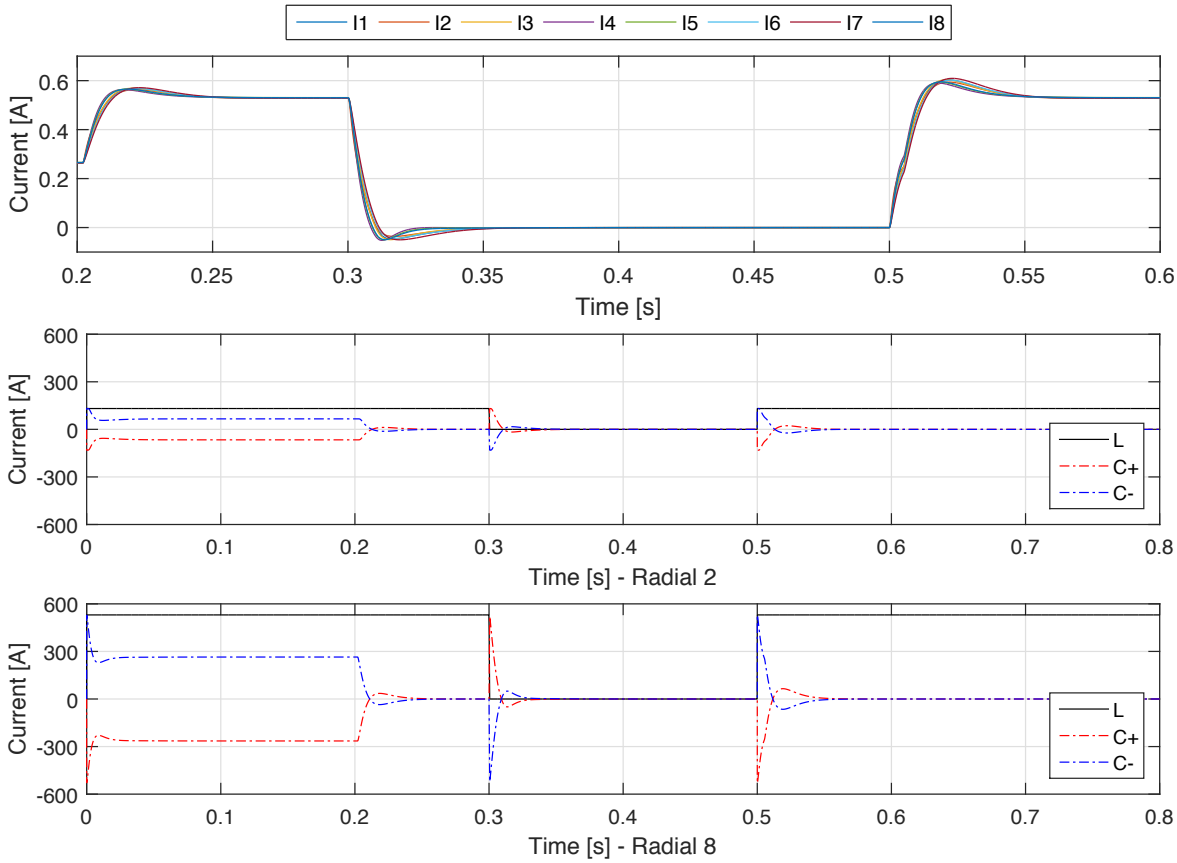


**Figure A.14:** Comparing lumped and full radials

## A.8 Small system

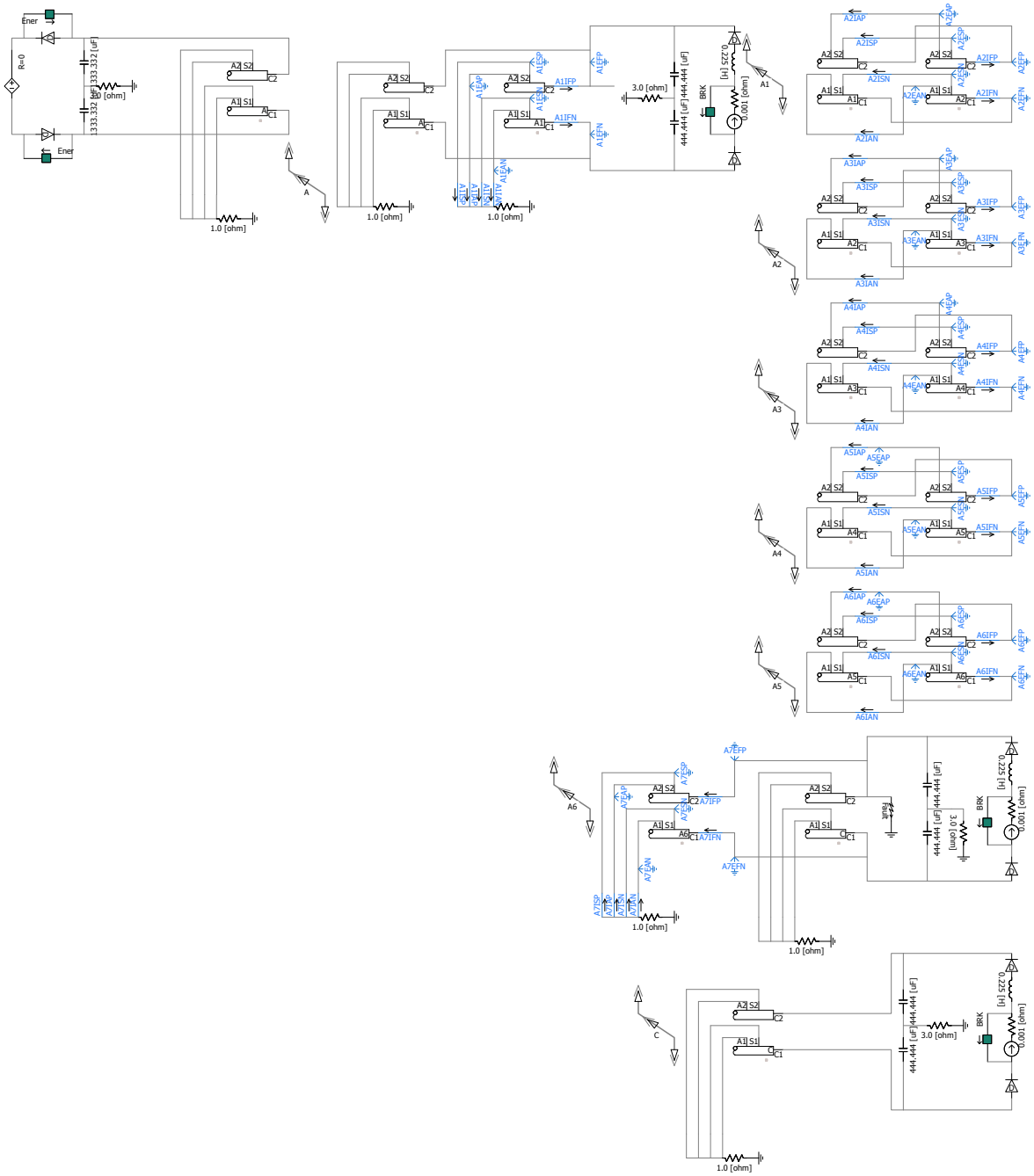


**Figure A.15:** The small system modelled in PSCAD

# Summary B

During the last decades wind power has become a serious participant in electrical power generation and the capacity of European offshore wind power is supposed to increase by 20 GW until the year 2020. Within today's offshore wind farms the power of the individual turbines is gathered in an AC collection network and transferred from an offshore substation to shore. If situated remotely from shore, offshore wind farms are connected to the national grids via HVDC links. This means that power is converted several times within the wind farm before reaching the onshore grid. Disadvantages of this common practice are conversion losses and the necessity of large, heavy and costly equipment. One promising approach to improve costs and losses of future wind farms is the utilisation of a DC power collection network and DC/DC converters. If wind turbines have an MVDC output, which then is collected at a single platform and converted to HVDC, considerable savings are achievable.

This thesis proposes such a DC collection network design and discusses aspects that need to be considered during the design process. Furthermore, a control and protection scheme is derived for the proposed system configuration. Finally, transient fault analysis of selected cases is conducted. From the entire wind farm, only the MVDC part is within the project scope.

Regarding the system design, a focus is placed on the dimensioning of cables for the application. Since MVDC cables are not available on the market yet and due to the different properties of DC compared to AC current transmission, e.g. the elimination of skin-effects, an MVDC cable design is developed. Furthermore, the system voltage level, DC/DC converter output filters, grounding strategies, switchgear and the utilization of single or multi- converter substation topologies are addressed. Conduction losses resulting from the cable design and rated system voltage are compared to expected annual energy production.

The control scheme aims at feeding power into the network according to a given power reference. However, since voltage drops in the network depend on active power flows, they have to be able to reduce their power injection in order to maintain the system voltages within allowed limits, if required. A control strategy is devised, where turbine power follows a given reference by adjusting the output current according to measured output voltage. In case of an overvoltage at the end of a feeder, all turbines within the same feeder reduce their power accordingly.

In order to exploit the potential savings that are expected of the DC wind farm concept, the system design is kept as simple as possible. Since switchgear is bulky and expensive, the system protection relies only on disconnectors. The hypothesis that this is possible is based on the fact that wind turbines with a converter interface do not contribute fault currents, hence only the energy stored in the system will feed into the fault. After the fault transient is depleted, the faulty part of the grid can by separated by disconnectors.

A model of the system for transient simulations in PSCAD is built. Short circuit transients are analysed for selected fault types, which are phase-to-phase and phase-to-ground faults at the turbine converter outputs and conductor-to-sheath faults in the MVDC cables. Characteristic transient waveforms are shown and analysed. Based on the transient study, a grounding strategy for cable

sheath and armours is selected. Furthermore, worst case faults are identified with respect to peak voltage stresses, temperature rise in the cables, and duration of the fault current transients.

Finally, it is shown that the system and MVDC cable design proposed in this project are able to withstand peak stresses in steady state and transient operation. However, some weaknesses are identified. Polarity reversal during fault transients suggest the employment of smoothing reactors at the DC/DC converters. Utilization of a multi-converter substation topology is preferable over a single-converter topology with regard to reliability in case of faults and seems more promising for the simple system design without breakers.

# Bibliography


[1] Hadi Saadat. *Power system analysis*. PSA Publishing LLC, 2010.

[2] Christoph Meyer, Markus Höing, Anders Peterson, Rik W. De Doncker. Control and design of dc grids for offshore wind farms. *IEE Transactions on Industry Applications, Vol. 43, No. 6*, 2007.

[3] Stefan Lundberg. *Wind Farm Configuration and Energy Efficiency Studies - Series DC versus AC Layouts*. Chalmers University of Technology, 2006.

[4] Sheng Jie Shao, Vassilios G. Agelidis. Review of dc system technologies for large scale integration of wind energy systems with electricity grids. *Energies 2010, Vol. 3*, 2010.

[5] Mufit Altin, Remus Teodorescu, Birgitte Bak-Jensen, Pedro Rodriguez, Florin Iov, Philip C. Kjær. Wind power plant control - an overview. *9th International Workshop on Large-Scale Integration of Wind Power into Power Systems*, 2010.

[6] MHI Vestas Offshore Wind A/S. V 164 8.0 mw. http://mhivestasoffshore.com/Products-and-services/The-Turbines/V164, accessed 24/02/2015.

[7] European Wind Energy Association. Wind in power - 2014 european statistics. www.ewea.org/fileadmin/files/library/publications/statistics/EWEA-Annual-Statistics-2014.pdf, 2015.

[8] European Wind Energy Association. Wind energy scenarios for 2020. www.ewea.org/fileadmin/files/library/publications/scenarios/EWEA-Wind-energy-scenarios-2020.pdf, 2014.

[9] T. Ackermann. *Wind Power in Power Systems*. John Wiley, 2012.

[10] Lena Max. *Design and Control of a DC Collection Grid for a Wind Farm*. Chalmers University of Technology, 2009.

[11] Remus Teodorescu, Marco Liserre, Pedro Rodriguez. *Grid Converters for Photovoltaic and Wind Power Systems*. John Wiley and Sons, 2011.

[12] Gerhard Ziegler. *Numerical Distance Protection*. Publicis Publishing, 2011.

[13] Gerhard Ziegler. *Numerical Differential Protection*. Wiley VCH, 2012.

[14] Jimmy Ehnberg, Thomas Nordlander. *Protection system design for MVDC collection grids for off-shore wind farms*. Elforsk, 2011.

[15] Zheng Ganhao. *Study on DC Circuit Breaker*. IEEE, 2014.

[16] Magnus Callavik, Anders Blomberg, Jürgen Häfner, Björn Jacobson. *The Hybrid HVDC Breaker - an innovation breakthrough enabling reliable HVDC grids*. ABB Grid Systems, 2012.

[17] Filipe Faria da Silva, Claus Leth Bak. *Electromagnetic Transients in Power Cables*. Springer, 2013.

[18] Thomas Worzyk. *Submarine Power Cables - Design, Installation, Repair, Environmental Aspects*. Springer, 2009.

[19] IEC. Invisible link - submarine power cables and connecting equipment are central to marine energy in iec e-tech marine and hydro power. www.iec.ch/etech/2013/pdf/etech-2013-07-LR.pdf, July 2013.

[20] Giovanni Mazzanti, Massimo Marzinotto. *Extruded Cables for High-Voltage Direct-Current Transmission: Advances in Research and Development*. John Wiley and Sons, 2013.

[21] AZO Materials. Crosslinked polyethylene - xlpe - typical properties. http://www.azom.com/article.aspx?ArticleID=855, accessed 24/03/2015.

[22] International Electrotechnical Commission (IEC). *Power cables with extruded insulation and their accessories for rated voltages from 1 kV (Um = 1,2 kV) up to 30 kV (Um = 36 kV) – Part 2: Cables for rated voltages from 6 kV (Um = 7,2 kV) up to 30 kV (Um = 36 kV)*. Danish Standards Foundation, 2014.

[23] J. F. Manwell, J. G. McGowan, A. L. Rogers. *Wind Energy Explained - Theory, Design and Application*. John Wiley and Sons, 2009.

[24] Jin Yang, John Edward Fletcher, John O'Reilly. Multiterminal dc wind farm collection grid internal fault analysis and protection design. *IEEE Transactions on Power Delivery, Vol. 25, No. 4*, 2010.

[25] General Cable. Ageing of xlpe compounds. http://www.generalcable.co.nz/getattachment/1e44846d-863c-458b-925c-ffdf59f725dd/Ageing-of-XLPE-Compounds.aspx, accessed 30/05/2015.

[26] Asia Pacific Wire and Cable Corp Ltd. Low voltage, medium voltage and high voltage xlpe power cable. http://www.apwcc.com/p3-products2-1-3.asp, accessed 30/05/2015.

[27] David R. Lide. *Handbook of Chemistry and Physics*. CRC Press, 2007.

[28] International Electrotechnical Commission (IEC). *Calculation of thermally permissible short-circuit currents, taking into account non-adiabatic heating effects*. International Electrotechnical Commission (IEC), 1988.

[29] J. R. Martí, L. Martí, H. W. Dommel. Transmission line models for steady-state and transients analysis. *Planning, Operation and Control of Today's Electric Power Systems*, 1993.

[30] Jin Yang, John O'Reilly, John E. Fletcher. *An Overwiev of DC Cable Modelling for Fault Analysis of VSC-HVDC Transmission Systems*. IEEE, 2010.

[31] PSCAD. *PSCAD/EMTDC On-Line Help System*. Manitoba HVDC Research Centre, 2013.

[32] Arthur Bergen, Vijay Vittal. *Power Systems Analysis*. Prentice-Hall, 2000.